© Copyright 2018

Zhenni Wan

Resistive Switching Effects of Vanadium Pentoxide Thin Film

Zhenni Wan

A dissertation

submitted in partial fulfillment of the

requirements for the degree of

Doctor of Philosophy

University of Washington

2018

Reading Committee:

M. P. Anantram, Chair

Robert Bruce Darling, Chair

Arka Majumdar

Program Authorized to Offer Degree:

Electrical Engineering

University of Washington

Abstract

Resistive Switching Effects of Vanadium Pentoxide Thin Film

Zhenni Wan

Chair of the Supervisory Committee:
Professor M. P. Anantram
Department of Electrical Engineering

In this Ph.D. work, the resistive switching effects of vanadium pentoxide (V_2O_5) thin films are extensively explored and investigated. Contrary to conventional Flash memory devices where the information is stored by the electrons in the floating gate (FG), emerging memory devices employs the resistive switching effects of metal-insulator-metal (MIM) devices in which the information is stored in the location of atoms, which determines the high or low resistance state.

Both reversible and irreversible resistive switching are discovered for the first time in V_2O_5 based MIM devices and the switching effects are studied as a function of metal contacts and environment, which play an important role in determining the device characteristics. Two conductor materials, chromium and indium tin oxide (ITO), are mainly investigated and the mechanisms for both irreversible and reversible switching are addressed. The dependence of

switching effects on testing environment is enabled by building a vacuum test chamber. The devices are tested in a variety of gases environment and the role of intercalated H_2O molecules in enabling the resistive switching is established. Resistance change is attributed to reduction of valence states of vanadium at electrode/V_2O_5 interface resulting from the electrochemical reactions when a voltage bias is applied. Reversibility of the switching is determined by whether the electrode material has the capability of temporarily storing oxygen ions.

V_2O_5 xerogel film synthesized by sol-gel process experiences drastic atomic structural change during post annealing process, resulting in significant impact on resistive switching characteristics. X-ray diffraction analysis reveals that α-phase V_2O_5 forms at bottom V_2O_5/ITO interface while β-phase V_2O_5 forms at top V_2O_5/ITO interface. The presence of intercalated H_2O molecules is essential for the reversible switching to occur. *Ab initio* calculations prove that the enlarged interlayer spacing in V_2O_5 xerogel significantly reduces the formation energies of oxygen vacancies, thus enabling the creation of mobile oxygen ions.

In order to make the synthesis of V_2O_5 thin film more compatible with modern IC fabrication processes, thermal evaporation is employed for V_2O_5 deposition. Reversible bipolar switching is preserved and the stability of I-V characteristics over annealing temperature has been improved. DFT calculations are performed to simulate the amorphous V_2O_5 structure generated by melt-quench process using *ab initio* molecular dynamics technique. Formation energies of oxygen vacancy is also reduced in amorphous V_2O_5. Degradation of V_2O_5 film due to spontaneous reduction of vanadium oxide with presence of intercalated water molecules has been suppressed.

TABLE OF CONTENTS

List of Figures iv

List of Tables viii

Chapter 1. Introduction 1

1.1 Background 1

1.2 Outline 4

Chapter 2. Irreversible Resistive Switching in Xerogel V_2O_5 Thin Film 8

2.1 Characterization 8

2.1.1 Film Synthesis 8

2.1.2 X-ray Diffraction Analysis 9

2.2 Device Structure 11

2.3 Current-Voltage Characteristics in Air 12

2.4 Switching Mechanism 14

2.5 Asymmetry in Two Interfaces 17

2.6 Physical Explanation for Diode and Resistor-Like States 18

2.7 Other Structures Tested 21

2.7.1 ITO/V_2O_5/Cr Structures 21

2.7.2 Ti/V_2O_5/Cr and Ti/V_2O_5/ITO Devices 24

2.8 Summary of Chromium/V_2O_5 Devices 25

Chapter 3. Forming Free Bipolar Resistive Swtiching in ITO/V_2O_5/ITO Structure 27

3.1 Motivation 27

3.2 Results 29

3.2.1 Resistive Switching Characteristics 29

3.2.2 Contact Diameter Dependent Switching Voltages 32

3.3 Switching Mechanism 33

3.4 Discussion 35

3.5 Summary of ITO/V_2O_5/ITO Devices 37

Chapter 4. Engineering of the Resistive Switching Properties by Atomic Structural Transition in ITO/V_2O_5/ITO Structure 39

4.1 Motivation 39

4.2 Results 41

4.2.1 I-V Characteristics at Various Annealing Temperatures 41

4.2.2 TGA and X-Ray Diffraction Analysis 43

4.3 Discussions 45

4.3.1 Asymmetrical Interfaces 45

4.3.2 Microscopic Insights 48

4.4 Summary of The Impact of Phase Transition 53

Chapter 5. Bipolar Resistive Switching Characteristics of Thermally Evaporated V_2O_5 Film 54

5.1 Methods 55

5.2 Experimental Results 57

5.3 Simulation and Discussion 60

5.3.1 Simulation of Oxygen Vacancy Formation Energy 60

5.3.2 Localized Bipolar Resistive Switching Induced by Joule Heating ... 63

5.4 Summary of Thermally Evaporated V_2O_5 Thin Film Devices ... 71

Chapter 6. Photon-Induced Coloration of V_2O_5 Thin Film in ITO/V_2O_5/ITO Structure ... 73

6.1 Experimental Method and Results ... 73

6.1.1 Device Structure and Fabrication Process ... 73

6.1.2 I-V Characteristics in Dark and Illuminated Environment ... 74

6.1.3 Coloration of V_2O_5 Film ... 76

6.2 Physical Explanations ... 78

6.3 Discussion and Relation to Previous Chapters ... 80

Chapter 7. Conclusion ... 82

Bibliography ... 84

Appendix A ... 94

LIST OF FIGURES

Figure 1.1. A flash memory cell 2
Figure 1.2. Atomic structure of orthorhombic V_2O_5 crystal..3
Figure 2.1. SEM image of V_2O_5 xerogel film synthesized by sol-gel process. (a) Bulk region of the film. Inset: Surface height profile extracted from AFM data. (b) Edge of the film. Single nanoribbon can be observed clearly. 9
Figure 2.2. X-Ray diffraction analysis of V_2O_5 xerogel film annealed at different temperatures. 10
Figure 2.3. Schematic of the device structure. Bottom electrode is fabricated on silicon substrate. V_2O_5 xerogel film is then deposited by sol-gel process. Top electrode is then patterned by shadow mask evaporation. 11
Figure 2.4. Current-Voltage characteristics of the device in air atmosphere. (a) Low-bias measurements of the virgin-state. The device is in a high conductance state and lasts for over one month if not applied higher bias. (b) Forward-first sweep. Switching of the device happens and shows two peaks. (c) Following reverse sweeps. The device remains in a diode-like state with peaks. Inset: Sweeps with different scan rates. (d) Low-bias measurements show that device has been switched to low conductance state. 13
Figure 2.5. Reverse-first sweep I-V characteristics. (a) Low-bias measurements show that the resistor-like state has only 5~6 times higher resistance than the virgin-state. (b) Switching occurring at reverse bias shows similar peaks (-0.3 V, -0.7 V) as forward bias case, but turn the device into a resistor-like state. 14
Figure 2.6. I-V measurements in different environments. (a) Sample is in vacuum for 5 minutes. Switching still occurs as it's in air. (b) Following sweeps show much less hysteresis and reduced peak. (c) Sample has been in vacuum for over 2 hours. Switching is highly suppressed due to water removal. (d) Chamber is vented and the same sample in (c) is tested in nitrogen and water vapor. Switching occurs once again. 16

Figure 2.7. Band structure of the device. (a) Virgin-state. Chromium has low work function and thus forms a weak Schottky barrier at the interfaces. The device behaves like a resistor in low bias range. (b) Diode-like state. Interfacial layer with reduced oxidation states forms at top interface, creating a stronger Schottky contact. (c) Resistor-like state. Interfacial layer is formed at bottom interface, but with thinner width. Electrons can tunnel through easily. 20

Figure 2.8. I-V characteristics of ITO (top)/V_2O_5/Cr (bottom) devices. (a) Forward-first sweeps. (b) reverse first sweeps..22

Figure 2.9. I-V characteristics of Cr (top)/V_2O_5/ITO (bottom) devices. (a) Forward-first sweeps. (b) reverse first sweeps..23

Figure 2.10. Blue laser response of ITO (top)/V_2O_5/Cr (bottom) devices. (a) Low bias response. (b) 3V forward bias response. 24

Figure 2.11. I-V characteristics of (a) Ti/V_2O_5/Cr device (b) Ti/V_2O_5/ITO.........................25

Figure 3.1. Resistive switching characteristics of ITO/V_2O_5/ITO structure, measured by using a probe tip (2 μm diameter) on the top ITO layer. The applied voltage varies from 0 V→3 V→0 V→–3 V→0 V. Abrupt resistive switching is observed at +2.5 V during the initial sweep. The resistance is reset to its initial state after a bias of –1.5 V is applied. 30

Figure 3.2. Transient response of the ITO/V_2O_5/ITO device. The applied voltage is shown in blue. The detected current is shown in green. (a) +0.2 V, 200 ns “READ” pulse in the low resistance state. (b) +0.2 V, 200 ns “READ” pulse in the high resistance state after applying a “SET” pulse of +4 V, 200 ns. (c) +0.2 V, 200 ns “READ” pulse returning to the low resistance state after applying a “RESET” pulse of –4 V, 200 ns..31

Figure 3.3. Custom-built circuit for measuring transient response of device under test (DUT). 32

Figure 3.4. Positive switching voltage increases with the diameter of top metal contact. The smallest switching voltage (+2.5 V) is observed with a probe tip (~2 μm diameter). The highest switching voltage (+6.8 V) is observed when the contact diameter is 100 μm. 33

Figure 3.5. Proposed band diagram of the ITO/V_2O_5/ITO structure after a "SET" operation. At the top ITO/V_2O_5 interface, oxygen ions migrate from the V_2O_5 side to the ITO side, leaving an interfacial vanadium oxide layer with reduced oxidation states. A thin Schottky barrier is formed due to the reduced electron affinity of the interfacial layer, which is responsible for the increased resistance. Oxygen ions can be driven back into the V_2O_5 when a negative voltage is applied. 35
Figure 3.6. Current-voltage characteristics of ITO/V_2O_5/ITO structure at different temperatures varying from 4.0˚C to 62.3˚C. Resistive switching behavior persists in the tested temperature range. 37
Figure 4.1. Switching voltages vs post annealing temperatures 41
Figure 4.2. Thermogravimetric analysis (TGA) of V_2O_5 xerogel thin film 43
Figure 4.3. XRD results of ITO/V_2O_5/ITO structure 44
Figure 4.4. XRD results of ITO/V_2O_5/Glass, V_2O_5/Glass, V_2O_5/ITO and V_2O_5/Sapphire structures at annealing temperatures of (a) 280˚C (b) 400˚C...................................46
Figure 4.5. Phase distribution of ITO/V_2O_5/ITO device at annealing temperature above 280˚C and below 400˚C 48
Figure 4.6. Atomic structures of (a) α-V_2O_5. (b) ß-V_2O_5. (c) $V_2O_5 \cdot 0.5\ H_2O$, type I. (d) $V_2O_5 \cdot 0.5\ H_2O$ type II. 50
Figure 4.7. Atomic structure after removing oxygen atom and relaxation for (a) $V_2O_5 \cdot 0.5\ H_2O$ type II, O3 site. (b) $V_2O_5 \cdot 0.5\ H_2O$ type II, O4 site. 52
Figure 5.1. Bulk-and-stick plots of the simulated (a) orthorhombic α-V_2O_5 (b) amorphous V_2O_5 57
Figure 5.2. I-V characteristics of as-fabricated devices 58
Figure 5.3. Dependence of I-V characteristics on annealing temperatures........................59
Figure 5.4. Illustration of oxygen vacancy sites O(1), O(7) and O(9). 62
Figure 5.5. Test scheme setup for distribution of switching characteristics 64
Figure 5.6. Switching distribution showing the localized switching characteristics 65
Figure 5.7. Distribution of LRS and HRS of all the nine points tested 66
Figure 5.8. 3D TCAD simulation results of electric field distribution in ITO/V_2O_5/ITO structure. (a) top view. (b) cross section view. 67

Figure 5.9. Structure of patterned top ITO devices. 68
Figure 5.10. I-V characteristics of devices with patterned top ITO layer 69
Figure 5.11. Illustration of the Joule heating model 71
Figure 6.1. Structure of ITO/V_2O_5/ITO device and I-V measurement setup. 74
Figure 6.2. I-V characteristics of ITO/V_2O_5 xerogel/ITO device under microscope light. 75
Figure 6.3. Transient photoresponse measurements under blue laser (wavelength = 405 nm) 76
Figure 6.4. Optical microscope image of color change region. The shape of a probe tip can be clearly observed. 77
Figure 6.5. Transmittance spectrum of ITO/V_2O_5/ITO device before and after coloration. 78
Figure 6.6. Illustration of electrochemical reactions occurring in ITO/V_2O_5/ITO structure 79
Figure A.1. Design of test chamber and base 94
Figure A.2. Design of gas feedthrough port 95
Figure A.3. Design of sample stage 96
Figure A.4. Picture of test chamber, gas panel, pump and gas cylinders 96
Figure A.5. Picture of temperature-controlled probe station 97

LIST OF TABLES

Table 4.1. Energies of formation of oxygen vacancies in ß-V_2O_5 and $V_2O_5 \cdot 0.5\ H_2O$..........50

Table 5.2. Energies of formation of oxygen vacancies in amorphous V_2O_5. 60

ACKNOWLEDGEMENTS

It has been a long and amazing journey since I started working on the research topics in this dissertation. First, I would like to express my utmost appreciation to my supervisor and mentor, Prof. M. P. Anantram for his consistent support and guidance in the past few years. It has always been a privilege for me to have such a knowledgeable, inspiring, supportive and patient advisor to walk me through the research world of novel semiconductor devices. He has provided me with a great deal of freedom to explore different directions and methodologies in experiments, as well as maintained a high standard for the development of theory and explanation. This dissertation would not have been completed without him.

My same gratitude also goes to my other supervisor, Prof. Robert Bruce Darling for his generous and continuous guidance towards the completion of this thesis, especially on the experimental and instrumentation side. I started this journey with very limited knowledge and experience in laboratory and he basically taught me everything from scratch in terms of all the fabrication, characterization and instrumentation mentioned in this dissertation. I have always been inspired by his broad and deep knowledge, patience and support.

I would also like to thank my committee member Prof. Arka Majumdar for his guidance on optical aspects of this dissertation and his help on the instrumentation setup. It is always fruitful to discuss with a sharp researcher like him. Without the help from EE Nanophotonics Lab, the transient response measurements would not have been completed.

I would like to thank my GSR committee member Prof. Guozhong Cao for his sharp and fruitful comments during my general and final exams. His advice from the viewpoint of a material scientist inspires me a lot in the research on fabrication and characterization.

I would like to thank Prof. Lih Y. Lin for serving as my committee member. Thank you for all the kind help on setting up the instruments in the initial stage of my research.

I would like to particularly thank my group mates Hashem Mohammad and Yunqi Zhao for the help on first-principles calculations in this dissertation. They have shared inspiring and fruitful discussions on the simulation side which eventually leads to two publications. Thank you for being such amazing team mates. I was my great pleasure to work with you.

I would like to thank Washington Nanofabrication Facilities (WNF) for providing fabulous instruments towards the fabrication of my devices. The training and guidance provided by the staff members are also highly appreciated.

DEDICATION

To My Family

Chapter 1. INTRODUCTION

1.1 BACKGROUND

High speed non-volatile memory is highly desired and has many applications as it can maintain the stored information without any external power source. Currently, the most widely used non-volatile memory is Flash memory based on floating gate (FG) transistors [1, 2]. Figure 1.1 shows a typical flash memory cell that resembles a standard MOSFET, except that the transistor has two gates: control gate (CG) and floating gate (FG). During the programming process, a large positive voltage is applied on both the control gate and drain, creating a high current in the channel and enabling the hot electrons to inject into the float gate and get trapped there as the floating gate is insulated from the substrate [3]. By introducing negative charges into the floating gate, the threshold voltage (V_T) of the transistor increases so the current from drain to source under a small read voltage is low, representing a logic "0". During the erasing process, a large negative voltage applied on the control gate forces the electrons to tunnel off the floating gate and into the channel [2], resulting in a reduced threshold voltage and thus increases the drain-source current, which is a logic "1". Therefore, in Flash memory, the data is stored by the location of electrons.

While Flash memory has achieved great success over the past decades, it has its own limitations as the feature size of semiconductor industry keeps going down following Moore's Law. When the gate oxide becomes thinner and thinner, quantum tunneling effects take place and reduce the ability of the floating gate to hold its stored charge [3]. The excess fabrication process for the floating gate is also limiting the area for a unit cell. Typical programming/erasing time for a Flash memory cell is in μs range [4-6], which also limits the operation speed. Researchers are

investigating emerging memory devices, such as Phase Change Memories [7-11], FeRAMs [12-15], MRAM [16-20] and ReRAM to solve these issues.

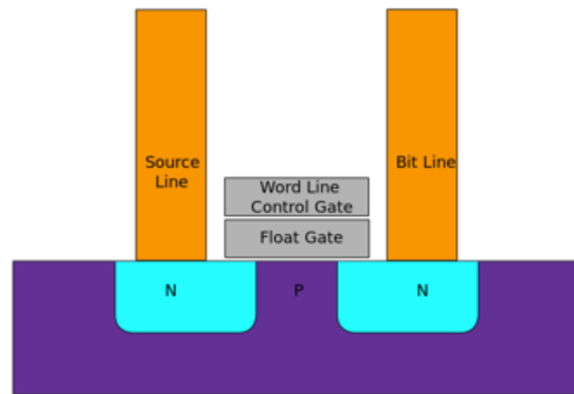

Figure 1.1. A flash memory cell

Resistive random access memory (ReRAM) is one of the promising candidates to replace the Flash memory in modern integrated circuits and computing [21-25]. Most resistive memories have a metal-insulator-metal structure and thus have a high resistance in their pristine states [26]. When a high forming voltage is applied on the device, conductive filaments that usually consists of metal ions or oxygen vacancies are formed between the two electrodes, reducing the resistance of the device by orders of magnitude, which is the logic “1”. An erasing voltage that either reverses the polarity or has a larger current compliance can break or dissolve the conductive filaments and switch the device back to high resistance state, achieving the logic “0”. Obviously in ReRAMs, the data is stored by the location of atoms in the device [27].

To achieve the formation of conductive filaments in ReRAM devices under a reasonable forming voltage, the insulator layer has to been very thin (usually only a few nanometers). However, other than forming conductive filaments bridging the two electrodes, resistance of the

MIM devices can also be changed by modifying the interface properties between metal and insulator. This type of resistive memories has not yet been extensively studied.

Vanadium pentoxide has been intensively studied in the past few decades due to its special electrical and chemical properties. Its orthorhombic layered structure (Figure 1.2) promises a large capacity of conducting and intercalating metal ions, especially lithium and sodium ions, for which it can be used as a cathode material in lithium-ion batteries [28, 29]. The dangling vanadium-oxygen bonds also suggest that the oxidation states could be easily reduced by electrochemical reactions that might enable the interfacial resistive switching.

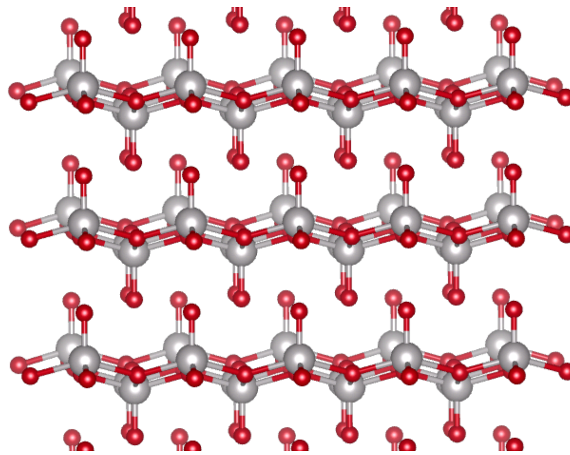

Figure 1.2. Atomic structure of orthorhombic V_2O_5 crystal

A persistent and reversible electrochromic effect is also observed in V_2O_5 structures, resulting from intercalation and extraction of ions [30]. In particular, Iwanaga performed nano-scale patterning of V_2O_5 thin film by conducting AFM in the air without depositing other ionic compounds as a charge source, suggesting that electrochemical reactions involving water molecules are possible to occur in a plain V_2O_5 film [31, 32].

Electron transport properties of crystalline V_2O_5 are commonly characterized by small polaron hopping (SPH) [33]. V^{4+} atoms (vanadium atom with a valence of four) created by thermal agitation and crystal defects induce extra electrons to the system, and electronic conduction occurs by means

of electron hopping accompanied by a travelling lattice distortion. Therefore, the conductivity of V_2O_5 can be enhanced by several orders of magnitude after ion intercalation, which significantly increases the concentration of V^{4+} states. Switching behavior has also been reported in V_2O_5 xerogel due to the creation of a conductive channel [34]. However, the application of V_2O_5 as a potential memory material employing its electrochemical properties has not yet been exploited so far.

V_2O_5 nanostructures, including nanowires, nanoribbons and nanofibers, have attracted increasing attention recently, and are used in multiple electrical devices such as field emitters [35] [36], field effect transistors [37], sensors [38-40] and photodetectors [41]. Nanoscale structures usually have higher surface to volume ratios, thus making it easier for electrochemical reactions to occur. One of the easiest ways to construct V_2O_5 nanostructures is through the sol-gel process. Nanoribbons are formed in DI water during a melt-quench process. After the gel is dispersed on the substrate and dried, most physically and chemically bonded water molecules evaporate, leaving a thin V_2O_5 xerogel film consisting of entangled nanoribbons [42]. Recent research has shown that such xerogel films with a nano-scale rough and porous surface could significantly enhance the electrochemical reaction capability compared to crystalline V_2O_5.

1.2 OUTLINE

In this thesis, we mainly explore the possible applications of nano-structured V_2O_5 thin film synthesized by sol-gel process for resistive switching based memory. Metal/V_2O_5/Metal structure is fabricated using microfabrication techniques; devices are characterized by various characterization methods such as scanning electron microscopy (SEM), atomic force microscopy (AFM) and X-ray Diffraction (XRD); electrical properties are measured by semiconductor parametric analyzers (Keithley 2600B and Keithley 4200SCS), oscilloscope (Keysight

DSO1022A) and function generator (Keisight 33621A); custom built vacuum chamber with the functionalities of controlling environments (pressure, moisture and gas compositions), temperature and laser coupling is employed to investigate the fundamental physics associated with the electrical properties.

In chapter 2, we investigate the electrical properties of a Cr/V_2O_5-xerogel/Cr device structure and observe abrupt switching in the current-voltage characteristics within a low bias amplitude of 1V. Interestingly, the switched electronic behavior of the device is controlled by the direction of the first applied bias: one is diode-like and the other is resistor-like. Such switching is irreversible and persistent, lasting for over 1 month. The switching mechanism is studied by performing environment dependent I-V measurements and attributed to electrochemical reactions at the metal/V_2O_5 interfaces involving water molecules. An interfacial layer with reduced oxidation states and thus lower electron affinity appears to be responsible for the diode-like and resistor-like behaviors of the device. Different electrode materials are used to replace one of the chromium electrodes but did not solve the issue of irreversibility.

Then we move to a ITO/V_2O_5/ITO structure in chapter 3, and apply a post annealing process to remove intercalated H_2O molecules which might be one reasons for the irreversibility. A novel bipolar forming free resistive switching behavior is discovered for the first time in this new structure. While the bottom ITO layer functions as a common ground electrode, the top ITO layer is an active element and used as an oxygen reservoir with an additional metal electrode patterned on its top for making contact. Our device exhibits a low resistance state (LRS) in its virgin state, and is switched to a high resistance state (HRS) when a forward bias of ~+2.5 V is applied. The device can be reset to its original state at a reverse bias of ~–1.5 V. Transient response of the device to applied voltage pulses with widths of 2 μs in a full programming and erasing cycle is also tested,

confirming that no forming process is required and the device has the potential to work in high speed circuit. By reducing the diameter of top metal contact, a significant decrease in switching voltage is observed, implying a strong electric field enhanced effect associated with the switching as the electric field beneath the top metal contact increases when decreasing the contact area, and the switching is likely to occur at the interface instead of bulk filaments. Although the ITO/V_2O_5/ITO structure seems to be symmetrical, asymmetry in electrical properties is observed when a reverse sweep is applied first. No resistive switching occurs up to -4 V and the I-V characteristics of the device remain resistor-like. Bipolar switching appears only when a forward bias is applied to the top electrode. This observation implies that oxygen ions do not migrate at the bottom V_2O_5/ITO interface and the two interfaces are asymmetric, which can be explained by the asymmetric fabrication processes.

In chapter 4, it is discovered that the post annealing temperature strongly affects the electrical properties of ITO/V_2O_5/ITO structure. For the bipolar reversible resistive switching, the switching voltages are optimized at post annealing temperature of 280°C; when the annealing temperature increases to 400°C, the resistive switching behavior disappears. X-ray Diffraction measurements suggest that the huge transition in electrical switching properties is related to the atomic lattice structure of V_2O_5. When the V_2O_5 film has large interlayer spacing supported by H_2O molecules, reversible switching occurs; when the annealing temperature increases and V_2O_5 becomes highly crystalline, reversible switching disappears. *Ab initio* calculations have been performed to evaluate the formation energies of oxygen vacancies in both V_2O_5 xerogel and crystalline bulk phases.

To overcome the drawbacks of V_2O_5 film synthesized by sol-gel process, thermal evaporation has been employed for V_2O_5 deposition and the resistive switching characteristics of fabricated devices are discussed in chapter 5. The thin film deposited by thermal evaporation has amorphous

nature and shows stable I-V characteristics over annealing temperature. Similar to the xerogel film, reversible switching behavior disappears when the annealing temperature reaches 400˚C and the film becomes fully crystalline. *Ab initio* molecular dynamics calculations are performed to simulate the amorphous V_2O_5 structure and evaluate the formation energies of oxygen vacancies, which also decreases due to the metastable nature of amorphous V_2O_5.

A unique coloration effect of ITO/V_2O_5/ITO structure is presented and discussed in chapter 6. The color of V_2O_5 xerogel film changes from orangish to greenish when it is exposed under blue laser with applied voltage bias. Both laser source with sufficient photon energy and adequate voltage bias are required for the coloration to occur. The coloration effect is a proof of reduction of oxidation states of vanadium atoms due to electrochemical reactions. The mechanism for coloration is discussed and the importance of controlling water content in V_2O_5 xerogel film is addressed again.

Chapter 2. IRREVERSIBLE RESISTIVE SWITCHING IN XEROGEL V_2O_5 THIN FILM

In this chapter, chromium was first employed as the electrode material for metal/V_2O_5/metal sandwich structure. Resistance change by Atomic Force Microscopy tip was discovered on V_2O_5/Cr structure previously [31] so we decided to use it as a starting point.

2.1 CHARACTERIZATION

2.1.1 *Film Synthesis*

The high aqueous solubility of hydrated V_2O_5 allows its use in solution-based microfabrication methods, which are fundamentally inexpensive, both in terms of materials and equipment, scalable to large areas, and do not involve any toxic or otherwise dangerous chemicals. Sol– gel techniques have proven to be the most versatile, and of these the melt-quench technique has yielded good and reproducible results on a variety of substrates.

The V_2O_5 thin film is synthesized by a sol-gel process. In this method, V_2O_5 powders were melted in a fused quartz crucible in an air atmosphere at a temperature of 800˚, and held for 15-20 minutes. The melting temperature of V_2O_5 is 670-685˚C. Then the melt was poured into DI water at room temperature and stirred for 1 hour. This process yielded a yellowish color gel, with V_2O_5 nanoribbons which have hydrated surfaces suspended almost homogeneously in water. This gel was applied to different substrates by a dip coating method. After application, the film was slowly dehydrated in open air on a hot plate with a fixed temperature of 40°C, which resulted in a xerogel film with a gentle overlapping of the ribbons and thus a good alignment of the c-axis normal to the

plane of the substrate. The film consists of entangled nanoribbons in the SEM images shown in Figure 2.1.

Surface roughness of the film is characterized by atomic force microscopy (shown in Figure 2.1 (a) inset). AFM measures the surface height distribution of the synthesized film. Based on the AFM data, the surface roughness is estimated to be 30 nm.

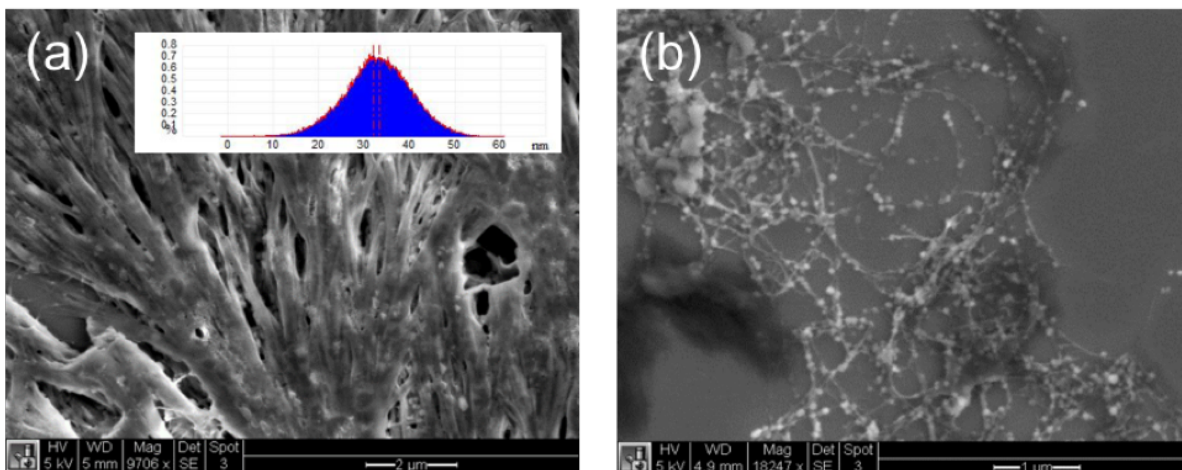

Figure 2.1. SEM image of V_2O_5 xerogel film synthesized by sol-gel process. (a) Bulk region of the film. Inset: Surface height profile extracted from AFM data. (b) Edge of the film. Single nanoribbon can be observed clearly.

2.1.2 *X-ray Diffraction Analysis*

The crystal structure of the V_2O_5 xerogel film was obtained by Bruker F8 Focus Powder X-ray diffractometer using an X-ray source of Cu K-α radiation with wavelength of 1.54 Å. Three samples were annealed for 30 minutes at different temperatures (150˚C, 300˚C and 400˚C). One control sample without annealing treatment was also tested for comparison (Figure 2.2).

One dominant peak which represents the (001) orientation can be identified in the results, showing a crystalline structure with random ab-planes but well-aligned c-axis. Note that even in the sample without any annealing, this peak is significant, indicating that the V_2O_5 nanoribbons

have a good alignment in c-axis. However, compared to bulk V_2O_5 with (001) peak at two theta equal to 20.8˚, our presented results, 6.9˚, 7.1˚, 7.9˚ and 12.3˚ respectively, all show smaller two theta values at the (001) peak, corresponding to larger interlayer spacing as a result of the water molecules intercalated between the V_2O_5 layers [42]. This is consistent with the fact that an increasing trend of two theta values is observed as the annealing temperature increases, which removes more intercalated water molecules. The full-width half-max (FWHM) of the (001) peak also shrinks and other small peaks appear while the annealing temperature increases. This means the nanoribbons exist at first, but slowly disappear when increasing the annealing strength, making the structure more like a uniform, crystalline thin film.

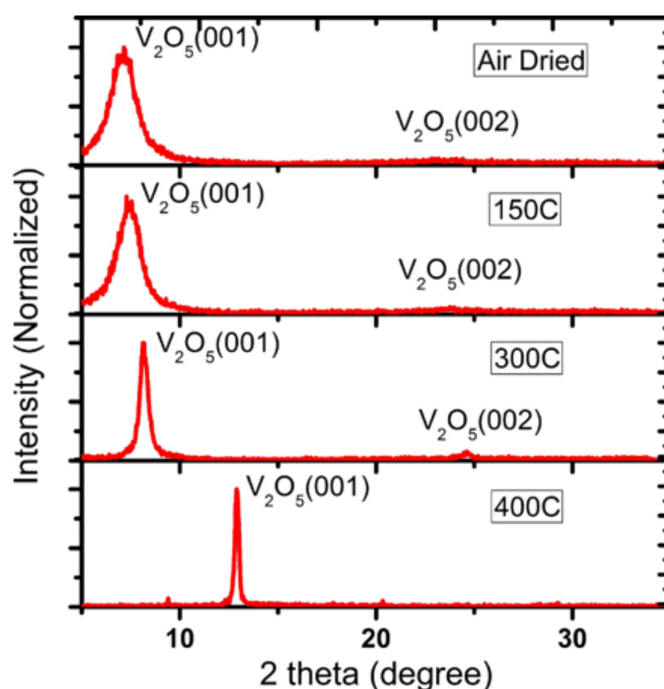

Figure 2.2. X-Ray diffraction analysis of V_2O_5 xerogel film annealed at different temperatures.

2.2 DEVICE STRUCTURE

A schematic of the tested device structure is shown in Figure 2.3. The device consists of a vanadium pentoxide xerogel thin film sandwiched by two metal electrodes. The bottom electrode is fabricated by e-beam metal evaporation. Aluminum with a thickness of 280nm is deposited on the silicon substrate, and then capped with a thin layer of 20 nm of chromium to prevent oxidation of the aluminum. The V_2O_5 xerogel thin film is then deposited by a dip coating process on top of the bottom electrode. The thickness of the film is uniform and around 900 nm. A top electrode dot with diameter ranging from 1mm to 10mm is patterned by a shadow mask during another e-beam metal evaporation. Note that chromium is also used as the interface metal in order to make the device symmetric. 260 nm of aluminum is then deposited to make the top electrode more robust for probe-station measurements as well as to avoid the internal stress of Cr which might crack the electrodes, and this is capped with another layer of Cr. After the device is fabricated, a clean room swab with DI water was used to remove the excess V_2O_5 layer around the top electrode, in order to eliminate the geometry effects and offer equivalent gas exposure to both top and bottom interfaces.

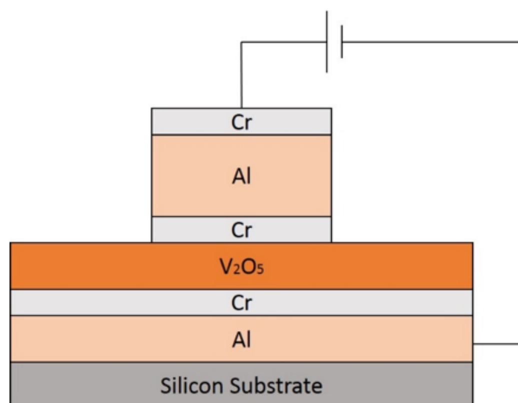

Figure 2.3. Schematic of the device structure. Bottom electrode is fabricated on silicon substrate. V_2O_5 xerogel film is then deposited by sol-gel process. Top electrode is then patterned by shadow mask evaporation.

2.3 CURRENT-VOLTAGE CHARACTERISTICS IN AIR

The current-voltage characteristics of the device are measured by a custom-built probe station and a Keithley 2612b source meter unit. In the measurements, the bottom electrode is grounded and a voltage bias is applied to the top electrode. Environmental tests are performed inside a custom designed high vacuum chamber that can as well be filled with mixtures of different gases.

Current-voltage measurements of the metal-V_2O_5-metal structure were first performed in air. The device exhibits a low-resistance state under low applied bias (200 mV), as shown in Figure 2.4 (a). This is characterized as the virgin-state of the device. Electrical switching occurs for the first time when a forward cyclic voltage sweep with magnitude of 1V is applied to the top electrode. A large hysteresis loop with two distinct peaks (at 0.3 V and 0.7 V respectively) exists in the I-V curve (Figure 2.4 (b)), indicating that the state of the device has been changed. The mechanism for switching is attributed to the change of oxidation states at the top electrode/V_2O_5 interface due to electrochemical reactions. In the subsequent voltage sweeps, the I-V curves behave like a diode with clear rectifying features as well as a few peaks (Figure 2.4 (c)). Note that the magnitude of the dominant peak keeps decreasing in the consecutive sweeps, indicating that the reactants, in this case mainly the V_2O_5 at the interface, is being consumed.

We have observed that the scan rates do not change the ability to obtain the transition in resistive to diode like behavior. The inset to Figure 2.4 (c) shows the I-V measurements with found different scan rates. With higher scan rates (400 mV/s and 800 mV/s), switching is suppressed in the first scan, implying that electrochemical reactions are limited by lack of time. However, repeated scans yield the same behavior as obtained with a single scan with a lower scan rate. That is, switching becomes more pronounced with increasing number of sweeps, further proving the

irreversibility of the devices. Further tests under low bias show that the current has been greatly suppressed (>1,000 times) with strong hysteresis after the switching (Figure 2.4 (d)).

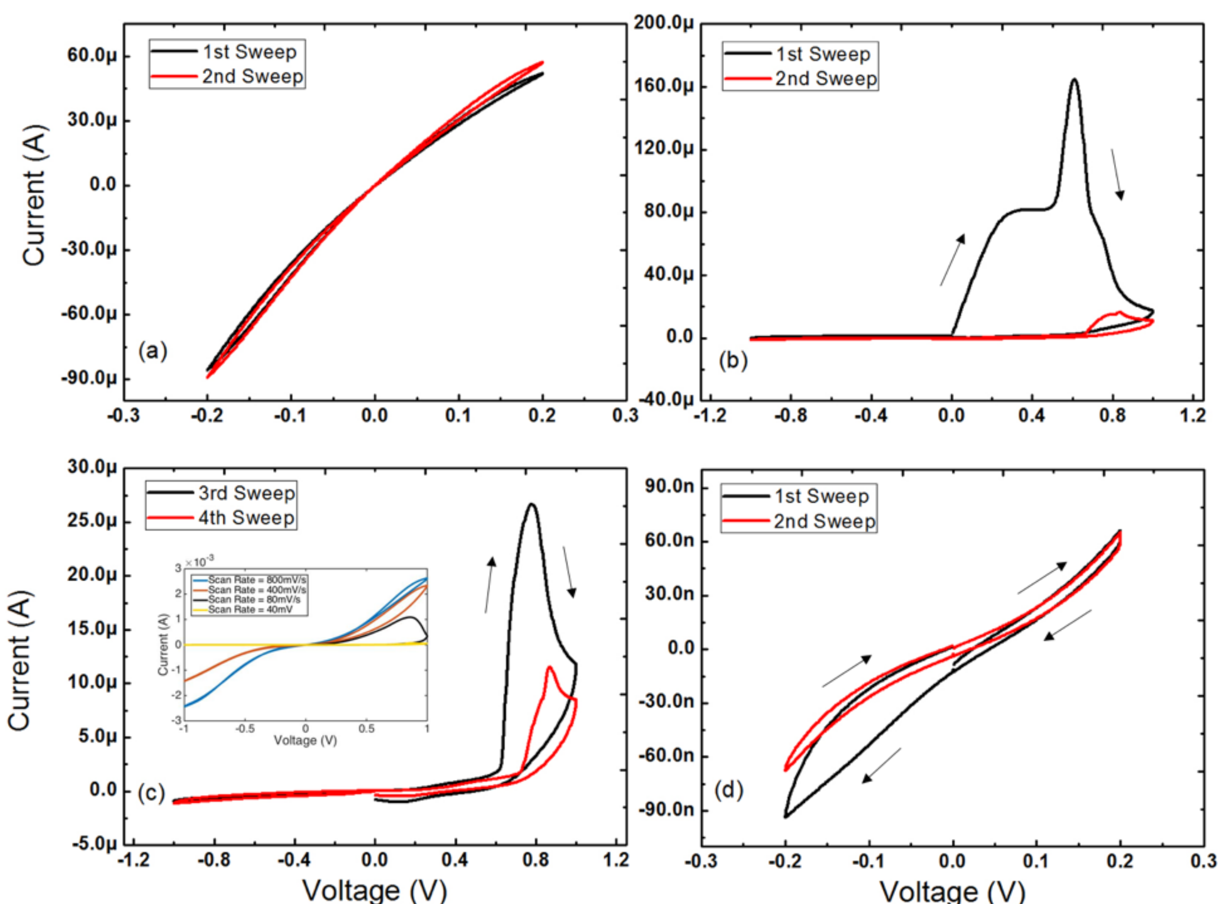

Figure 2.4. Current-Voltage characteristics of the device in air atmosphere. (a) Low-bias measurements of the virgin-state. The device is in a high conductance state and lasts for over one month if not applied higher bias. (b) Forward-first sweep. Switching of the device happens and shows two peaks. (c) Following reverse sweeps. The device remains in a diode-like state with peaks. Inset: Sweeps with different scan rates. (d) Low-bias measurements show that device has been switched to low conductance state.

Interestingly, the device exhibits an entirely different behavior when a reverse voltage sweep is applied first. Switching with similar hysteresis loop happens in the first reverse sweep and two peaks show up at -0.3 V and -0.7 V (Figure 2.5 (b)), implying that the same electrochemical reaction is happening at the bottom electrode/V_2O_5 interface. However, in the following sweeps,

the device shows highly linear I-V characteristics with little hysteresis, namely a resistor-like state (Figure 2.5 (b)). Further bias sweeps with a magnitude of 1 V have little influence on the I-V curves, indicating that further electrochemical reactions are prevented. The low bias current shows that the resistance of the device has been increased by 5~6 times (Figure 2.5 (a)). Both the diode-like and resistor-like states of the device last for over one month when the device was stored in a vacuum dessicator, suggesting that the switching is irreversible and persistent. No significant degradation of the device is detected within one-month time frame.

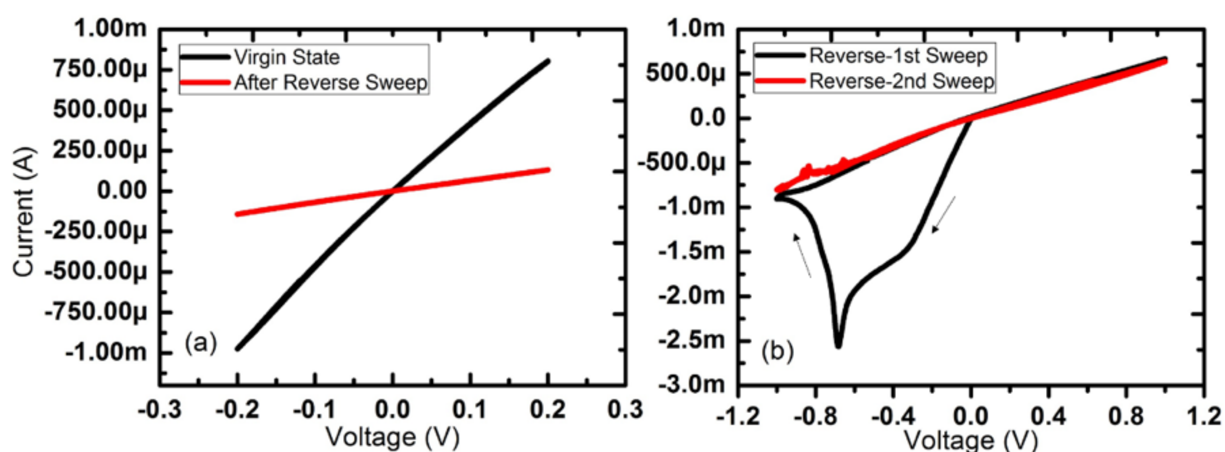

Figure 2.5. Reverse-first sweep I-V characteristics. (a) Low-bias measurements show that the resistor-like state has only 5~6 times higher resistance than the virgin-state. (b) Switching occurring at reverse bias shows similar peaks (-0.3 V, -0.7 V) as forward bias case, but turn the device into a resistor-like state.

2.4 Switching Mechanism

Vanadium has its highest oxidation state (V^{5+}) in V_2O_5 and has the capability of changing its oxidation state in the presence of reactants and an external electric field. Here, we attribute the reason for the abrupt switching of the device's electronic behavior to the reduced oxidation states formed at the Cr/V_2O_5 interfaces, due to electrochemical reactions involving water molecules. To

prove our hypothesis and further understand the switching mechanism, we performed I-V measurements in a controlled environment.

In Figure 2.6 (a), the device was measured in a vacuum environment (base pressure < 100 mTorr) for about 5 minutes. It is observed that the switching still occurs during the first forward sweep. In the following sweeps (Figure 2.6 (b)), the rectifying feature becomes less significant, the hysteresis is reduced and the peak is suppressed, implying that further electrochemical reactions are limited, due to the lack of reactants. As a comparison, we put another device in vacuum for over 2 hours, allowing any intercalated water molecules to fully evaporate. After evaporation, with applied bias, the device shows diminished switching behavior and remains in a high conductance state after multiple sweeps (Figure 2.6 (c)), indicating that the intercalated H_2O molecules are responsible for the switching observed in Figure 2.6 (a). Then, we pass air through a drying tube that helps remove moisture, and bring the pressure up to 600 Torr. I-V measurements in dry air also show that the switching does not occur (Figure 2.6 (c)), proving that H_2O in the environment is essential for switching to happen, and the switching of oxidation states is not due simply to the oxidation of chromium electrodes. Finally, a mixture of nitrogen and water vapor is passed into the chamber. In a few minutes, the device is able to be switched again (Figure 2.6 (d)), indicating that H_2O is sufficient for inducing switching. Small bubbles are observed in all the devices after switching, indicating that there are gases released in the reactions. Permanent loss of oxygen is likely to be the reason for the irreversibility of the switching.

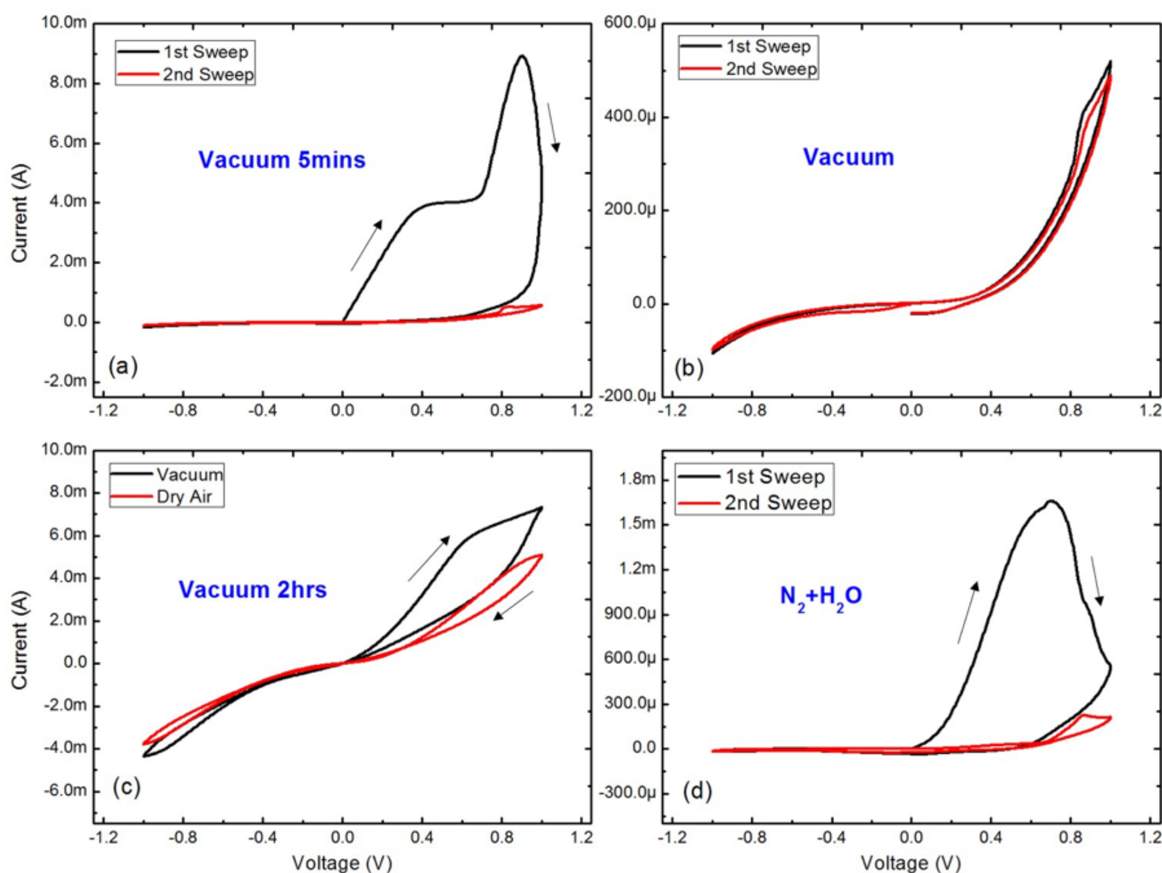

Figure 2.6. I-V measurements in different environments. (a) Sample is in vacuum for 5 minutes. Switching still occurs as it's in air. (b) Following sweeps show much less hysteresis and reduced peak. (c) Sample has been in vacuum for over 2 hours. Switching is highly suppressed due to water removal. (d) Chamber is vented and the same sample in (c) is tested in nitrogen and water vapor. Switching occurs once again.

So far, we have proved that the presence of H_2O molecules is essential for switching the device. With its layered atomic structure, V_2O_5 has the capability of intercalating cations such as lithium and protons. We provide a detailed hypothesis for the resistance change observed. When a voltage bias is applied to the device, the electric field at the Cr/V_2O_5 interface creates protons from the dissociation of H_2O molecules (2.1). Such reaction does not occur spontaneously as the dissociation of H_2O is endothermic and requires external energy [43]. The energy is provided by the current, which also explains the long stability of the virgin state. We note that in materials such

as TiO_2, the dissociative adsorption of H_2O on the TiO_2 surface is an exothermic process in the presence of oxygen vacancies [44]. The main hypothesis in our explanation is that the dissociation energy of H_2O is reduced when H_2O molecules are intercalated in V_2O_5 layers. The created protons are then driven into V_2O_5 nanoribbons, form bonds with oxygen (or create OH^- groups), reduce the oxidation states of V_2O_5 and form a colored $H_xV_2O_5$ (2.2). At room temperature, the presence of OH^- groups weakens the V-O bonds, making it much easier to remove H_2O molecules and leave oxygen vacancies in V_2O_5 lattice (2.4). In the chromium side, OH^- groups lose electrons and release oxygen gas, creating bubbles in the device (2.3). The complete electrochemical reactions at the Cr/V_2O_5 interface are shown below:

$$H_2O = H^+ + OH^- \tag{2.1}$$

$$V_2O_5 + xH^+ + xe^- = H_xV_2O_5 \tag{2.2}$$

$$4OH^- - 4e^- = 2H_2O + O_2 \uparrow \tag{2.3}$$

$$H_xV_2O_5 = \frac{x}{2}H_2O + V_2O_{5-\frac{x}{2}} \tag{2.4}$$

2.5 Asymmetry in Two Interfaces

The asymmetry in the current-voltage characteristics with two opposite bias polarities indicates that electrochemical reactions only involve interfacial V_2O_5 rather than the whole film, otherwise symmetric electrical characteristics would be observed regardless of the bias polarity. In our hypothesis, electrochemical reactions start from the Cr/V_2O_5 interface to form V_2O_{5-x} layer, and the thickness of interfacial layer with reduced oxidation states keeps growing with increasing number of bias sweeps until the applied bias cannot supply enough energy for electrochemical reactions to occur. The asymmetry we observed still stays pronounced after removal of excess V_2O_5 layer around the top electrodes, implying that the asymmetry does not simply arise from different

exposures to the humidity in the environment, but from the asymmetric synthesis process of the two Cr/V_2O_5 interfaces. Besides, under forward bias bubbles can be observed while there are none under reverse bias, indicating that electrochemical reactions are suppressed in the reverse bias case.

The bottom interface is formed during the sol-gel process of depositing V_2O_5 xerogel film, in which case the system is exposed to air on a slightly heated (40˚C) hot plate for about 5 hours. A very thin native oxide layer grows on top of the chromium layer during this process, which substantially reduces the reactivity with the subsequent grown V_2O_5 xerogel film. By contrast, top interface is formed in the e-beam evaporator chamber with high vacuum environment, where the fresh chromium atoms impact the V_2O_5 surface with a variety of incident angles without being terminated by oxygen. During subsequent bias sweeps, if a reverse bias is applied first, electrochemical reactions occurring at the bottom interface are restricted by the native oxide on the chromium as it takes more energy for the electrons bound by OH^- groups to overcome the oxide barrier and transfer to the chromium electrode, resulting in a relatively thin layer of vanadium oxide with reduced oxidation states. In the other case of a forward sweep first, the un-oxidized chromium allows the electrochemical reactions to fully take place until all the reactants have been exhausted, implying a much thicker interfacial layer with reduced vanadium oxidation states. The asymmetric thicknesses of these interfacial layers with reduced oxidation states are responsible for the asymmetric I-V characteristics in the resistor-like and diode-like states of the device.

2.6 Physical Explanation for Diode and Resistor-Like States

In this section, we describe one possible explanation for the underlying mechanism responsible for the different diode-like and resistor-like behaviors programmed by the polarity of the first applied

bias. Previously we found that during the voltage sweep, electrochemical reactions occurred at the Cr/V_2O_5 interfaces, introducing vanadium oxide layer with reduced oxidation states into the system. It has been reported that reduction of oxidation states in V_2O_5 will dramatically decrease the electron affinity of vanadium oxide [45], which helps provide insight in understanding the device's behavior.

The band structure of a virgin-state device is shown in Figure 7(a). The conduction band energy of V_2O_5 is close to the Fermi energy of chromium, forming a low Schottky barrier (Φ_b) for electrons. There is also a very thin layer of chromium oxide on top of the bottom electrode. Note that the electron affinity (E_A) of the chromium oxide is close to the work function of chromium. Thus, in the virgin-state of the device, the conductance is high and the contact resistance can be neglected in the low-bias range. When a forward sweep is applied, protons are driven into the V_2O_5 layered structure continuously and they create oxygen vacancies in the lattice, resulting in a thick interfacial layer with reduced oxidation states (Figure 7(b)). The electron affinity (E_A) of such interfacial layer is much lower than the V_2O_5 region, indicating that the conduction band energy rises and thus a Schottky contact with higher electron barrier (Φ_{b1}) is formed at the top interface. This Schottky barrier is responsible for the diode-like behaviors in the forward-first I-V measurements. Note that the increased Schottky barrier is consistent with the polarity of conduction we observed in the experiments. In the contrasting case of a reverse-first sweep, similar electrochemical reactions will first occur at the bottom interface. However, such reactions are highly limited by both the native oxide on chromium. Therefore, a much thinner interfacial layer is formed in the reverse-first sweep (Figure 7(c)), resulting a thinner Schottky barrier region through which electrons can easily tunnel. On the other hand, such a thin Schottky barrier region still increases the contact resistance at bottom interface to a few times larger than the bulk

resistance of V_2O_5 region. In the following sweeps, the increased contact resistance acts as a voltage divider that limits the voltage drop at both interfaces, thus preventing the occurrence of further electrochemical reactions. Therefore, the device remains in resistor-like state.

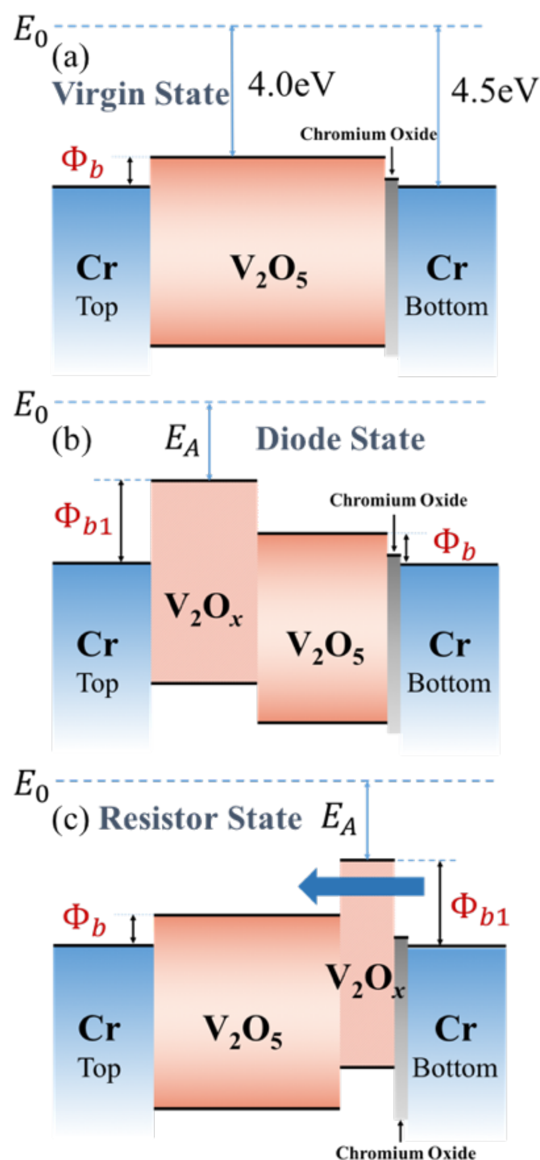

Figure 2.7. Band structure of the device. (a) Virgin-state. Chromium has low work function and thus forms a weak Schottky barrier at the interfaces. The device behaves like a resistor in low bias range. (b) Diode-like state. Interfacial layer with reduced oxidation states forms at top interface, creating a stronger Schottky contact. (c) Resistor-like state. Interfacial layer is formed at bottom interface, but with thinner width. Electrons can tunnel through easily.

2.7 OTHER STRUCTURES TESTED

Asymmetrical resistive switching has been discovered in the Cr/V_2O_5/Cr structure and the mechanism is explained by the reduction of oxidation states of vanadium atoms. So far, the switching is irreversible due to the release of oxygen gas, and for real application in circuits, it is important to make it reversible. To achieve this goal, we have also tested other device structures with different conductors that are available in Washington Nanofabrication Facility (WNF) as electrodes, such as ITO/V_2O_5/Cr, Cr/V_2O_5/ITO, Ti/V_2O_5/Cr. It turns out that asymmetrical switching only occurs in Cr/V_2O_5/Cr devices.

2.7.1 *ITO/V_2O_5/Cr Structures*

We first tried replacing one chromium electrode with the conductive transition oxide - indium tin oxide (ITO). ITO is one of the most widely used transparent conductive oxides and it has a wide bandgap of around 4 eV that allows visible lights to pass through. The purpose of this work is to investigate the light response of V_2O_5 devices as well as the effects of a different conductor as electrode. ITO is fabricated by magnetron sputtering, which typically gives a sheet resistance of 80Ω/sq with thickness of 160nm and work function of 4.1 eV. Compared to chromium, it is much less conductive but should form a low Schottky barrier with V_2O_5 that exhibits resistor-like behavior. Two types of devices are fabricated: devices with ITO as the top overlayer and devices with ITO as the bottom adlayer. The other electrode is kept as chromium. The asymmetric fabrication process that has been described in previous section still exists in chromium. ITO electrode itself is kept symmetric for both overlayer and adlayer as ITO does not get oxidized in

the air. Top electrode is patterned by shadow mask during fabrication process while bottom electrode covers a whole 4'' wafer so there is an intrinsic asymmetry between the two electrodes.

I-V characteristics of the two types of devices are measured using Keithley 2600B and a custom-built probe station. The I-V characteristics of the ITO overlayer devices are shown in Figure 2.8. Little switching can be observed under positive bias, while significant switching is featured under negative bias. The asymmetric diode-like and resistor-like behaviors disappeared. Regardless of the polarity of the first sweep, the devices only show one final state – resistor-like state.

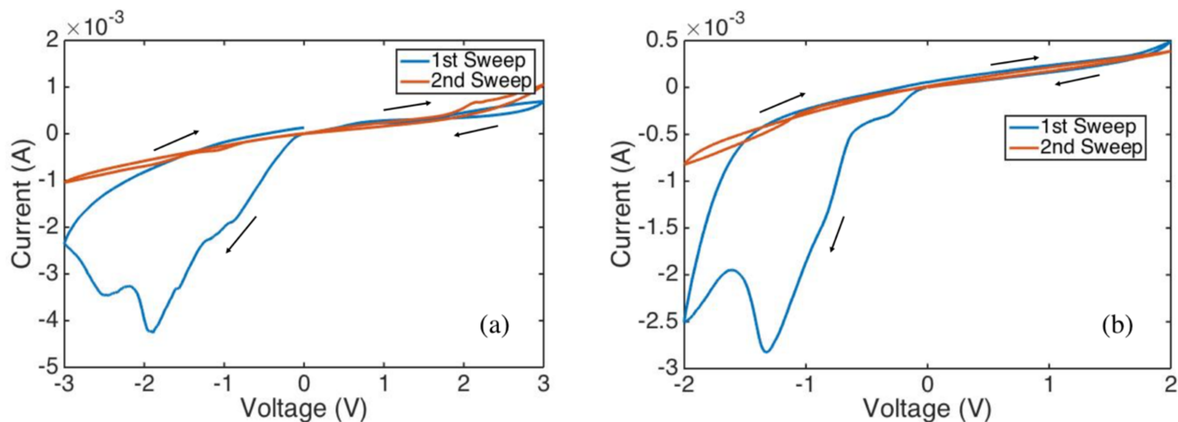

Figure 2.8. I-V characteristics of ITO (top)/V_2O_5/Cr (bottom) devices. (a) Forward-first sweeps. (b) reverse first sweeps.

As a comparison, the I-V characteristics of the ITO bottom adlayer devices are shown in Figure 2.9. Huge switching behaviors are observed under positive bias during both forward and reverse sweeps with amplitude of 1V. Small hysteresis loop is observed under negative bias during reverse first sweep, but it does not change the state of the device. It's clear that switching under positive bias is dominant in determining the status of the device. By contrast to the ITO overlayer devices, diode-like behavior is the only state after switching.

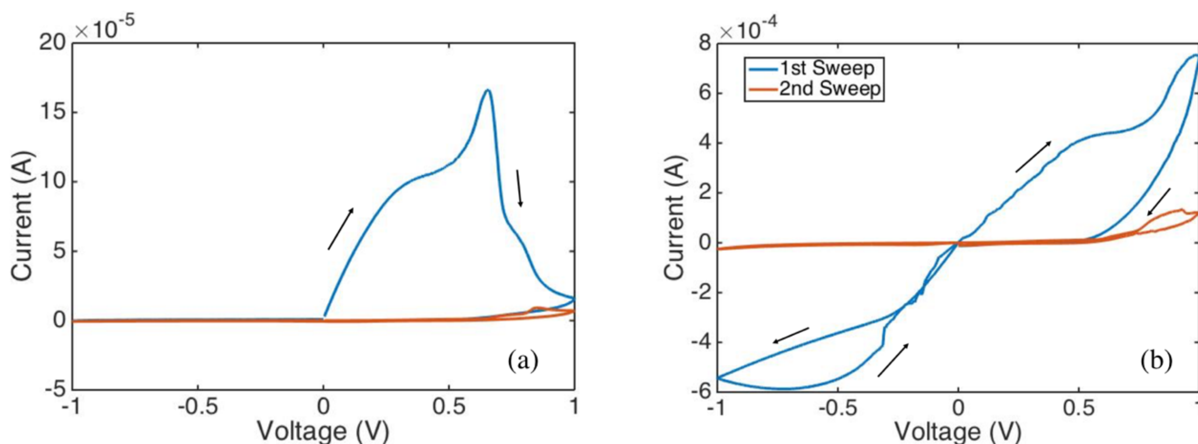

Figure 2.9. I-V characteristics of Cr (top)/V_2O_5/ITO (bottom) devices. (a) Forward-first sweeps. (b) reverse first sweeps.

Based on the previous I-V measurements, it can be concluded that asymmetry still exists by comparing ITO overlayer and adlayer devices. When ITO is the top overlayer, device exhibits resistor-like state after switching regardless of the polarity of the first sweep; in the other case when ITO is the bottom adlayer, device only shows diode-like state after switching. In other words, the final state of the device is determined by Cr/V_2O_5 interface instead of ITO/V_2O_5 interface. This is a further proof of our previous hypothesis, that is, asymmetric Cr/V_2O_5 interfaces result in different levels of electrochemical reactions, which substantially decide the device state.

Photoresponse of ITO (top)/V_2O_5/Cr (bottom) devices is also tested. The results are shown in Figure 2.10. Blue laser with wavelength of 405 nm (photon energy = 3.06 eV) is shined on the top electrode with applied voltage sweep by the probe tips and the same I-V measurements are also performed in dark environment as a comparison. Figure 10 shows that even though the photon energy of blue laser is larger than the bandgap of V_2O_5, there is very little photoresponse observed in the devices. A possible explanation is that when the device is in resistor-like state, its conductance is already high so that the photon generated current is very small compared to its intrinsic current. Another observation is that the color of the device changes when a large voltage

is applied. Bluish color change is observed under negative bias and reddish color change is observed under positive bias. Notice that this color change is not relevant to the blue laser as it is observed both with and without blue laser source. This color change is also not persistent and disappeared after a few minutes.

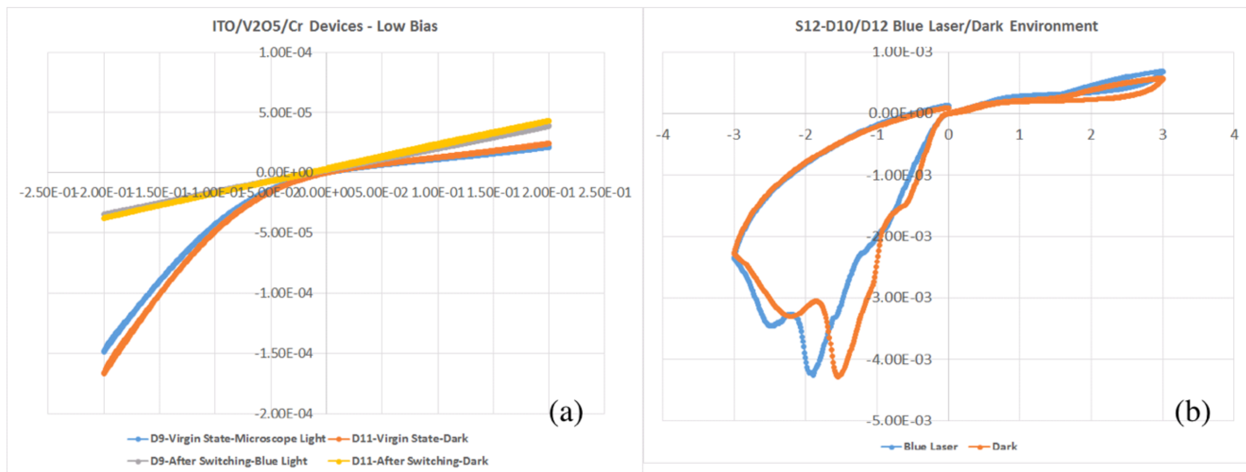

Figure 2.10. Blue laser response of ITO (top)/V_2O_5/Cr (bottom) devices. (a) Low bias response. (b) 3V forward bias response.

2.7.2 *Ti/V_2O_5/Cr and Ti/V_2O_5/ITO Devices*

To solve the problem of irreversibility, we also tried to employ titanium as one of the electrodes. Titanium has been used in various resistive memory devices as reactive electrode capping transition metal oxides such as HfO_2. The generally accepted mechanism for the reversible switching is that titanium acts as an oxygen reservoir that temporarily stores oxygen atoms which are driven by applied electric field, creating oxygen vacancies in the sandwiched oxide region that substantially changes the conductivity of the device. It would be interesting to introduce this material as one of the electrodes to see if it could help change the irreversibility.

We have tested two device structures: Ti/V_2O_5/Cr and Ti/V_2O_5/ITO. Titanium is fabricated by electron beam evaporation and always acting as the top electrode due to its high reactivity with oxygen in the air. The I-V characteristics of the devices are shown in Figure 2.11.

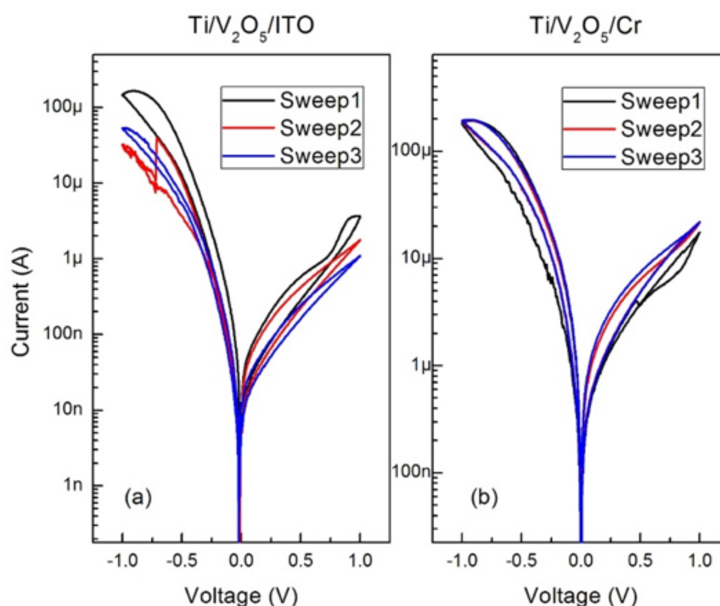

Figure 2.11. I-V characteristics of (a) Ti/V_2O_5/Cr device (b) Ti/V_2O_5/ITO.

The I-V characteristics of both device structures show strong rectifying feature, that is, the device is conducting under negative bias but relatively insulating under positive bias. Slight hysteresis behavior can be observed under negative bias, but there is hardly any under positive bias. This feature could be explained by the high reactivity of titanium itself. V_2O_5 is already fully oxidized and might react with titanium during deposition process, forming a built-in interfacial layer with reduced oxidation states that decreases the conductivity under forward bias.

2.8 SUMMARY OF CHROMIUM/V_2O_5 DEVICES

In this chapter, we mainly investigated the electrical switching properties of Cr/V_2O_5 xerogel devices. V_2O_5 xerogel film fabricated by sol-gel process has nano-structured surface consisting of bundled V_2O_5 nanoribbons. Without post annealing process, the film contains intercalated H_2O

molecules between atomic layers of V_2O_5. When the film is sandwiched by two chromium electrodes, significant change in the resistance of the film is discovered and the switching is asymmetrical and irreversible. Environmental tests have confirmed that the irreversible switching is catalyzed by the intercalated H_2O molecules. The significant increase in resistance is attributed to the reduction of oxidation states of vanadium at Cr/V_2O_5 interface. Different electrode materials such as ITO and Titanium have been tried to solve the problem of irreversibility. However, so far reversible electrical switching has not yet been achieved, which prohibits the application of V_2O_5 in real-world memory circuits.

Chapter 3. FORMING FREE BIPOLAR RESISTIVE SWTICHING IN ITO/V_2O_5/ITO STRUCTURE

In the previous chapter, we have discussed the asymmetrical irreversible resistive switching discovered in Cr/V_2O_5/Cr sandwich structure. Due to the existence of intercalated H_2O molecules, vanadium ions are easily reduced when a small voltage bias is applied and oxygen gas is created as there is no place for the oxygen ions to be temporarily stored. Testing on other devices with different electrode materials also indicates that the presence of Cr in the sandwich structure is always the dominant electrode that introduces irreversible switching. As it is important to have reversible operation between the two resistance (memory) states, we probed the ITO/V_2O_5/ITO structure with a post annealing process added to get rid of the intercalated H_2O molecules, which could also introduce irreversible switching. A novel interfacial forming-free bipolar switching is discovered that is very different from the conventional filamentary switching in resistive random access memory (RRAM).

3.1 MOTIVATION

Resistive random access memory (RRAM) is considered as one of most promising candidates for the next generation memory due to its high speed [46, 47], low power consumption [46] and superior scalability [47, 48]. Most RRAMs are based on Metal-Insulator-Metal (MIM) systems and can be divided into two categories: unipolar switching and bipolar switching [26]. The generally accepted physical mechanism responsible for bipolar switching is the formation and annihilation of conductive filaments due to migration of ions driven by electric field [21]. Prior to resistive switching behavior, a large forming voltage that is a few times higher than the switching voltage is usually required to form the conductive filaments in a pristine insulator layer. However,

high forming voltages result in very high electric fields, which cause severe electrical and mechanical stresses to the MIM memory element (the value of the voltage depends on the thickness of the insulating layer). Dramatic changes of the film morphology are observed after forming, including partial blowoff of electrode material [49]. The forming process may also result in unpredictable resistance states, which lowers the device yield [50, 51]. Obviously, reducing or even eliminating the forming step is valuable for practical applications.

So far, the so-called forming free resistive switching with two different characteristics has been realized. In the first case, the pristine state resistance is similar to the high resistance state (HRS) after reset, and the forming voltage is comparable to the subsequent set voltage [52]. In the second case, conductive filaments have already existed in the as-fabricated RRAM cells, resulting in an initial ON state [53-56]. However, both cases require elaborate control of the defect profiles of the device achieved by various approaches, including film thickness optimization [54], ion doping [52, 55], thermal treatment [53] and fabrication modulation [52, 56]. The drawback is that this increases the complexity of fabrication. In this work, we demonstrate a forming-free bipolar resistive switching in ITO/V_2O_5/ITO sandwich structure for the first time. Commercial ITO coated glass with a sheet resistance of 15 Ω/sq is used as substrate and bottom contact. The carrier concentration is estimated to be $9.66 \times 10^{20}\ cm^{-3}$, by using parameters from literature [57]. The Fermi level is thus calculated to be around 1.02 eV above the conduction band minimum [58] [59]. A thin film of V_2O_5 with a thickness of 300 nm is deposited using a sol-gel process. The top layer of ITO (160 nm) is deposited by magnetron sputtering and the corresponding sheet resistance is 50 Ω/sq. After the deposition of the top ITO, a post annealing step is applied at 300˚C for 20 minutes in ambient air to remove the intercalated water molecules in the V_2O_5 xerogel layer. An

additional top contact made from Cr (20 nm)/Al (260 nm)/Cr (20 nm) is then deposited and patterned by a shadow mask, with contact diameters ranging from 30 μm to 100 μm.

3.2 RESULTS

3.2.1 *Resistive Switching Characteristics*

The current-voltage (I-V) characteristics of the device were measured by a custom-built probe station and a Keithley 4200 source meter unit (SMU). The bias voltage is applied on the top metal electrode and the bottom ITO electrode is grounded. The measured characteristics are shown in Figure 3.1. An abrupt drop in current is observed at around +2.5V, indicating a static resistance that has increased by 5~8 times, varying with different devices. The current level is reset to its original state after a reverse bias of –1.5V is applied. Subsequent sweeps show consistent and reproducible resistive switching characteristics. Notice that no forming process is required prior to the bipolar switching behavior. During the DC voltage sweep no current compliance is applied either. The results not only suggest a reversible bipolar resistive memory behavior in the V_2O_5 device, but also imply a novel switching mechanism different from conventional resistive memories with metal-insulator-metal structures, in which case a large forming voltage is required to create conductive filaments in the pristine insulator layer. In addition, the large thickness of the V_2O_5 layer prevents the formation of any conductive filaments bridging two electrodes under such small biases.

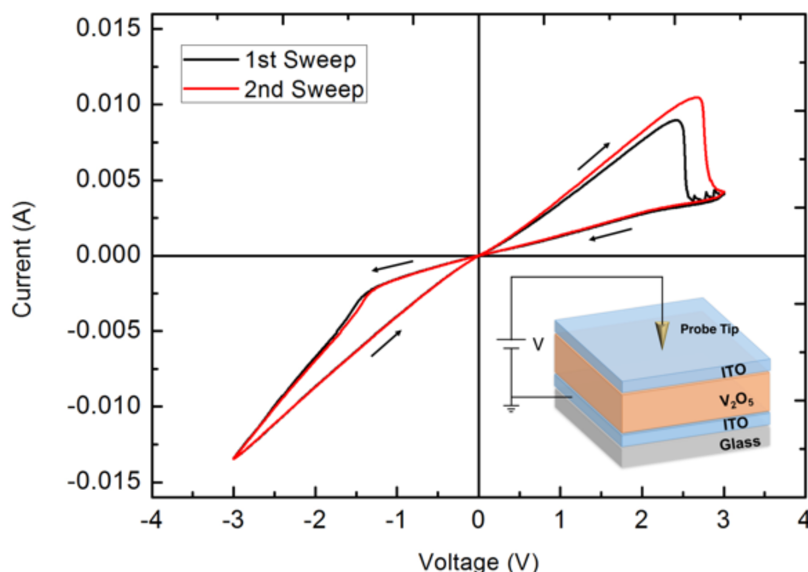

Figure 3.1. Resistive switching characteristics of ITO/V_2O_5/ITO structure, measured by using a probe tip (2 μm diameter) on the top ITO layer. The applied voltage varies from 0 V→3 V→0 V→–3 V→0 V. Abrupt resistive switching is observed at +2.5 V during the initial sweep. The resistance is reset to its initial state after a bias of –1.5 V is applied.

Figure 3.2 shows the transient response of the device to applied voltage pulses with widths of 2 μs in a full programming and erasing cycle. The initial status of the device is read by a +0.2 V voltage pulse (Figure 3.2 (a)) and shows a high current of 600 μA. Then a +4 V pulse is applied (Figure 3.2 (b)), followed by another "read" operation that shows a lowered current of 400 μA (Figure 3.2 (c)). A –4 V pulse is applied (Figure 3.2 (d)) to reset the current of the device to 580 μA (Figure 3.2 (e)). Note that the decreased ON/OFF ratio shown in the transient response is due to the degradation of the sample which has a ON/OFF ratio of 2:1 even during DC sweep. The transient response results show that the devices have the potential to operate in high speed circuit.

It is also worthy to point out that the switching speed of ITO/V_2O_5/ITO device is much higher compared to the Cr/V_2O_5/Cr devices. In the case of chromium devices when the scan rate is 0.8 V/s, there is very little switching observed in the I-V curves, indicating that the irreversible

switching is a relatively slow process. In the case of ITO devices, the switching speed is increased by orders of magnitude, suggesting a difference in fundamental switching mechanisms.

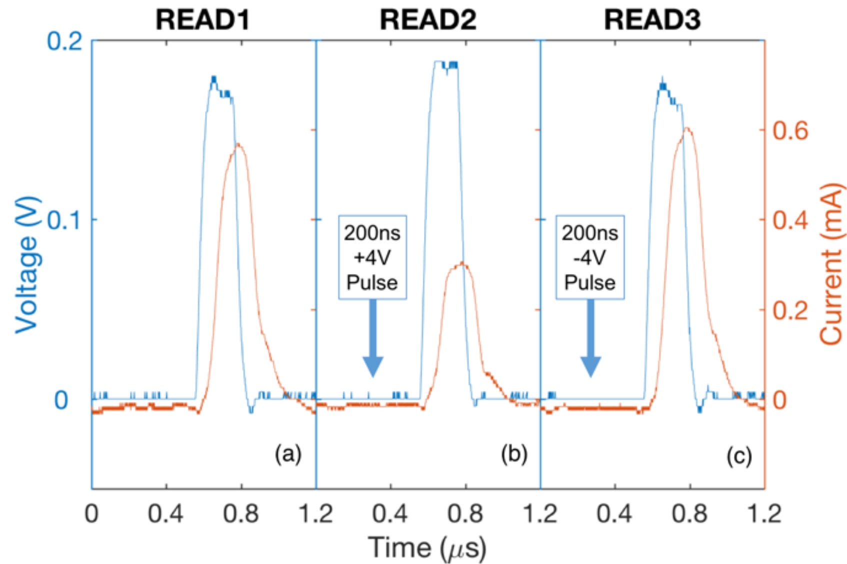

Figure 3.2. Transient response of the ITO/V_2O_5/ITO device. The applied voltage is shown in blue. The detected current is shown in green. (a) +0.2 V, 200 ns “READ” pulse in the low resistance state. (b) +0.2 V, 200 ns “READ” pulse in the high resistance state after applying a “SET” pulse of +4 V, 200 ns. (c) +0.2 V, 200 ns “READ” pulse returning to the low resistance state after applying a “RESET” pulse of −4 V, 200 ns.

Note that the transient response is measured by a custom-built circuit on a breadboard using a function generator (Keysight 33621A) and an oscilloscope (Keysight DSO1022A) controlled by a custom-built LabVIEW interface (Figure 3.3). A single voltage pulse is sent by the function generator; negative terminal of the high-speed op-amp LM318 is virtually grounded so the current flowing through DUT is approximately equal to V_{pulse}/R_{DUT}. As the op-amp has a high input impedance, all the current will enter the branch with feedback resistor R_f, resulting in a voltage signal that equals $-V_{pulse}/R_{DUT}*R_f$ at the output of the op-amp. This voltage pulse is then detected by the oscilloscope and the data is processed by LabVIEW interface.

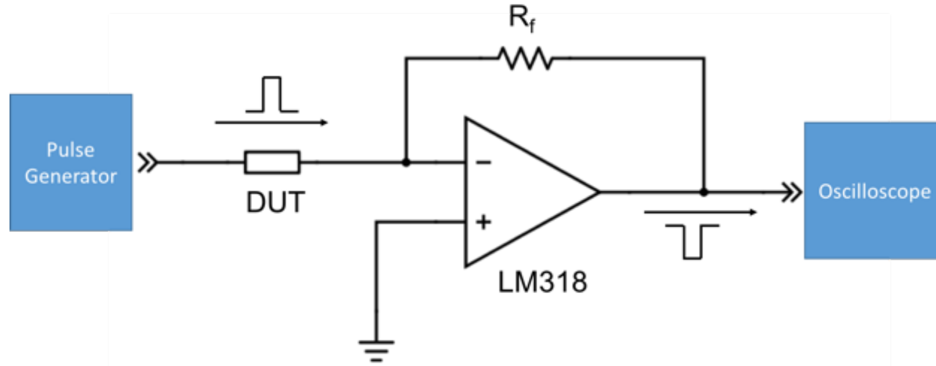

Figure 3.3. Custom-built circuit for measuring transient response of device under test (DUT).

3.2.2 *Contact Diameter Dependent Switching Voltages*

ITO/V_2O_5/ITO devices with different metal contact diameters varying from 30 μm to 100 μm were fabricated. Reversible switching characteristics are observed for all the devices, but at different voltage biases. A systematic linear drop in the positive switching voltage is found when the contact diameter decreases. The results are shown in Figure 3. The lowest switching voltage (+2.5 V) is observed when a probe tip with 2 μm diameter is directly in contact with the top ITO layer. A similar trend is also observed for the negative switching voltages.

The results indicate a significant fringe effect associated with the switching process. As the contact becomes smaller, the electric field beneath the electrode is increased by the larger edge to area ratio, thus enhancing the migration of mobile ions in the system, and reducing the required applied voltage for switching. The contact size dependent switching voltages of the tested devices also support the hypothesis that conductive filament mechanism, which generally does not depend on contact size, is unlikely to be the underlying physics of switching.

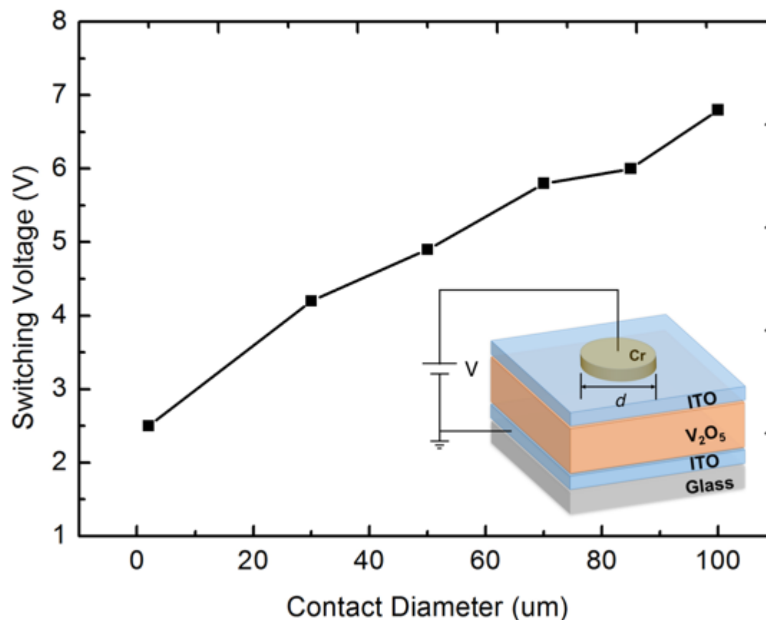

Figure 3.4. Positive switching voltage increases with the diameter of top metal contact. The smallest switching voltage (+2.5 V) is observed with a probe tip (~2 μm diameter). The highest switching voltage (+6.8 V) is observed when the contact diameter is 100 μm.

3.3 Switching Mechanism

Irreversible resistive switching characteristics were discovered in V_2O_5 xerogel films sandwiched by chromium electrodes in our previous work [60]. When a sufficient voltage bias is applied, oxygen vacancies formed at V_2O_5/Cr interfaces create an energy barrier for electrons to overcome, thus reducing the conductance of the device. Such a switching process is catalyzed by the intercalated water molecules in the V_2O_5 xerogel film. Oxygen gas is released after the switching and a permanent loss of oxygen ions is proposed to be the reason for the irreversibility.

When the electrodes are replaced by ITO and a post annealing step is added, the reduction in conductance of the devices becomes reversible. Indium tin oxide has a fluorite structure with 25% empty oxygen sites in an ordered array [61]. Unlike the dense chromium electrodes, a conductive ITO film deposited by RF sputtering has oxygen vacancies acting as both a source for free electrons

and a reservoir for oxygen ions. Yang et al. [62] reported a bipolar switching behavior in the ITO/HfO_2/ITO system which usually involves conductive filaments consisting of oxygen vacancies. This observation indicates that ITO can store oxygen ions in a reversible way. The post annealing step removes the intercalated water molecules in the V_2O_5 film, and thus prevents the formation of oxygen gas. In our experiments here, no bubbles were observed after the reversible switching.

It is proposed that the creation of oxygen vacancies in the V_2O_5 lattice at the V_2O_5/ITO interface is responsible for the resistive switching. When a positive voltage is applied on the top electrode, oxygen ions are extracted from the V_2O_5 lattice and driven to fill in the oxygen vacancies in the top ITO layer, leaving a thin vanadium oxide layer with reduced oxidation states behind. A reduction in electron affinity is expected due to the loss of oxygen [45], thus a thin Schottky barrier is formed between the vanadium oxide layer and ITO electrode (Figure 3.5). This is also consistent with the experimental observation that the conduction band minimum of V_2O_5 shifts to about 1 eV above the Fermi level when the oxidation state is reduced, while the position of valence band maximum barely changes [63]. Before the reduction, the conduction band was only 0.3 eV above the Fermi level. The band gap of ITO is 2.9 eV according to literature [64], and the position of Fermi level has been calculated previously. The filling of oxygen vacancies in the ITO layer also results in an increase in resistance. This corresponds to the abrupt decrease of current in I-V characteristics under forward bias. When a negative voltage is applied, oxygen ions are driven back to refill the vacancies in the interfacial layer, resulting in the conductance increasing back to its initial state.

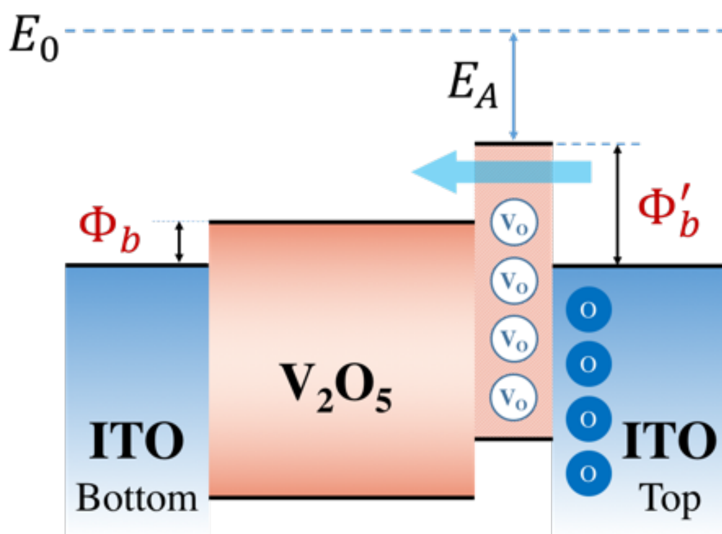

Figure 3.5. Proposed band diagram of the ITO/V_2O_5/ITO structure after a “SET” operation. At the top ITO/V_2O_5 interface, oxygen ions migrate from the V_2O_5 side to the ITO side, leaving an interfacial vanadium oxide layer with reduced oxidation states. A thin Schottky barrier is formed due to the reduced electron affinity of the interfacial layer, which is responsible for the increased resistance. Oxygen ions can be driven back into the V_2O_5 when a negative voltage is applied.

3.4 Discussion

Although the ITO/V_2O_5/ITO device structure seems to be symmetrical, asymmetry in electrical properties is observed when a reverse sweep is applied first. No resistive switching occurs up to −4 V and the I-V characteristics of the device remain resistor-like. The same switching appears only when a forward bias is applied to the top electrode. This observation implies that oxygen ions do not migrate at the bottom V_2O_5/ITO interface and the two interfaces are asymmetric. We believe the asymmetry originates from the different fabrication processes for the ITO layers. The bottom V_2O_5/ITO interface is formed in a sol-gel process that does not involve high-energy irradiation. Whereas when the top ITO is deposited on the V_2O_5 film, the whole substrate is immersed in an Argon plasma and it is possible that surface lattice structure of the V_2O_5 film has changed to a more reactive state after this exposure. Another possible explanation is the asymmetrical contact size.

The bottom ITO electrode covers the whole wafer and is much bigger than the top metal contact. When a reverse bias is applied, the electric field is less confined at the bottom V_2O_5/ITO interface, making ion migration more difficult to occur.

To investigate the robustness of the resistive switching behavior, we have measured current-voltage characteristics at temperatures varying from 4.0˚C to 62.3˚C (Figure 3.6). Distinct switching features can be observed at all the temperatures tested without degradation, showing that the device has potential to operate in a wider temperature range.

Preliminary endurance cycling tests of the device have also been performed in ambient air condition at room temperature (results not listed). After about 10 cycles, destructive changes of the surface topography are observed, resulting in degradation of the top contact. The LRS and HRS can then no longer be detected due to high contact resistance. The degradation of the device occurs after about one-month exposure in the air, accompanied by the color changing from orangish to greenish. Bipolar switching behavior disappears after the degradation and the device simply exhibits a resistor-like state. Future engineering of film quality and fabrication process will be needed to solve these issues.

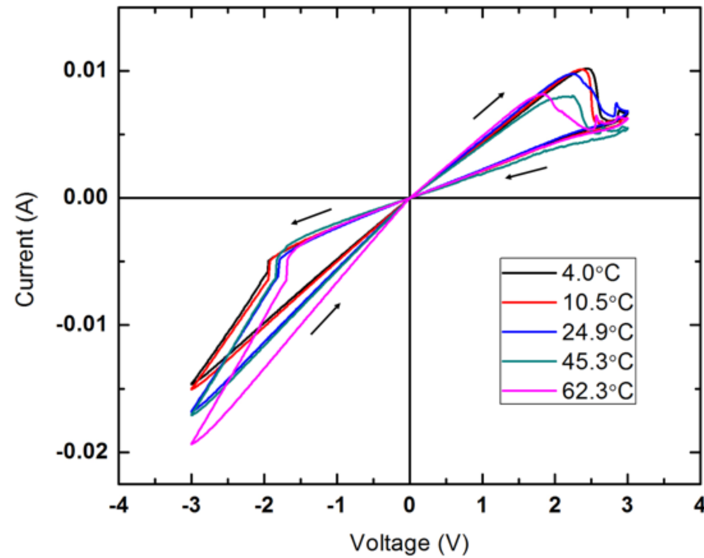

Figure 3.6. Current-voltage characteristics of ITO/V_2O_5/ITO structure at different temperatures varying from 4.0˚C to 62.3˚C. Resistive switching behavior persists in the tested temperature range.

3.5 Summary of ITO/V_2O_5/ITO Devices

In this chapter, reversible bipolar resistive switching is observed in a metal/ITO/V_2O_5/ITO structure. Opposite to the conventional bipolar switching observed in MIM structures, the device starts with a low resistance state (LHS) and is switched to high resistance state (HRS) without a prior forming process when a positive voltage is applied on top electrode. The switching voltage decreases when the size of top metal contact is reduced, indicating a significant fringe effect that enhances the electric field beneath the contact and thus accelerates the migration of oxygen ions at the top ITO/V_2O_5 interface. Creation of oxygen vacancies in the vanadium oxide layer and filling of oxygen vacancies in the ITO layer are responsible for the increased resistance after switching. The results suggest future applications of this V_2O_5 structure in low-power, high speed integrated non-volatile memories.

Chapter 4. ENGINEERING OF THE RESISTIVE SWITCHING PROPERTIES BY ATOMIC STRUCTURAL TRANSITION IN ITO/V_2O_5/ITO STRUCTURE

Bipolar resistive switching has been reported in ITO/V_2O_5/ITO structure. Synthesized from sol-gel process, the $V_2O_5 \cdot nH_2O$ xerogel film endures significant structural transition during the post annealing step. The impact of structural transition of V_2O_5 film on the resistive switching properties is studied in this work. The switching voltage decreases from 6.5 V to 3.0 V when the annealing temperature increases from 220˚C to 280˚C, and then increases up to 5.0 V at 350˚C. Above annealing temperature of 350˚C, the reversible switching characteristics disappears. Thermogravimetric measurement show that intercalated H_2O molecules fully evaporate above 350˚C. X-ray diffraction shows that the xerogel phase gradually vanishes as the annealing temperature increases, and only α-V_2O_5 and ß-V_2O_5 exist at high annealing temperatures. Ab initio simulations are performed to evaluate the formation energies of oxygen vacancy in xerogel, α-V_2O_5 and ß-V_2O_5 phases. The results are in good agreement with the experiments: the formation energy of oxygen vacancy is significantly lower in xerogel than in α-V_2O_5 and ß-V_2O_5, enabling the occurrence of reversible switching when xerogel phase exists in the sandwich structure.

4.1 MOTIVATION

Resistive random access memory (ReRAM) is considered to be one of the most promising candidates for the next generation memory due to its high speed [46, 47], low power consumption [46] and superior scalability [47, 48]. Most RRAMs are based on Metal-Insulator-Metal (MIM) systems and employ transition metal oxides such as HfO_2 [46], TiO_2 [47], ZnO [65] and ZrO_2 [66]

as the sandwiched insulator layer. A widely accepted mechanism for bipolar resistive switching, which means SET and RESET operations require opposite voltage polarities, is the formation of conductive filaments consisting of oxygen vacancies in the oxide layers due to the applied electric field [21]. Reports have indicated that the crystallinity of the insulator layer plays an important role in determining the resistive switching performance [67] as the oxygen vacancy formation energies differ for amorphous and crystalline oxides. This fact provides insights to engineer the electrical switching properties for other oxygen vacancy based RRAMs.

Vanadium pentoxide (V_2O_5) is widely used as cathode material for lithium batteries [68-70] due to its layered atomic structure [42, 71] and the capability of storing intercalated ions [29]. Previously, a novel forming-free bipolar resistive memory was discovered on ITO/V_2O_5/ITO structures [72]. ITO coated glass with a sheet resistance of 10 Ω/sq is used as substrate and bottom contact. A thin film of V_2O_5 with a thickness of 800 nm is deposited using a sol-gel process. A gentle pre-annealing at 220˚C is added for 1 hour to reduce the amount of intercalated water molecules and prevent bubbling during the post-annealing process. The top layer of ITO (160 nm) is deposited by magnetron sputtering and the measured sheet resistance is 50 Ω/sq. It was proposed that oxygen vacancies were formed in V_2O_5 at the top ITO/V_2O_5 interface due to the applied electric field and this creates a thin Schottky tunneling barrier which increases the overall resistance. The oxygen ions migrate into or out of the top ITO layer which consists of sufficient vacancies to achieve reversible switching. The formation of oxygen vacancies in the V_2O_5 layer is critical in the electrical switching process and can have a significant impact on the switching voltage, which is of great importance in terms of energy consumption and electrical stress to peripheral circuits elements. As the V_2O_5 film is synthesized from sol-gel process, it will endure a drastic structural transition under various temperatures. In this work, we investigate the impact of structural

transition of V_2O_5 thin film in the ITO/V_2O_5/ITO sandwich structure due to post-annealing process at various temperatures. Significant change in resistive switching properties is found and the underlying mechanism is attributed to the change in the oxygen vacancy formation energies resulting in phase transition from xerogel to α-/ß-V_2O_5 when annealing temperature increases.

4.2 RESULTS

4.2.1 *I-V Characteristics at Various Annealing Temperatures*

Current-voltage characteristics of ITO/V_2O_5/ITO devices are measured using Keithley 4200SCS parametric analyzer after applying post annealing at temperatures varying from 220˚C to 400˚C. The results are shown in Figure 4.1.

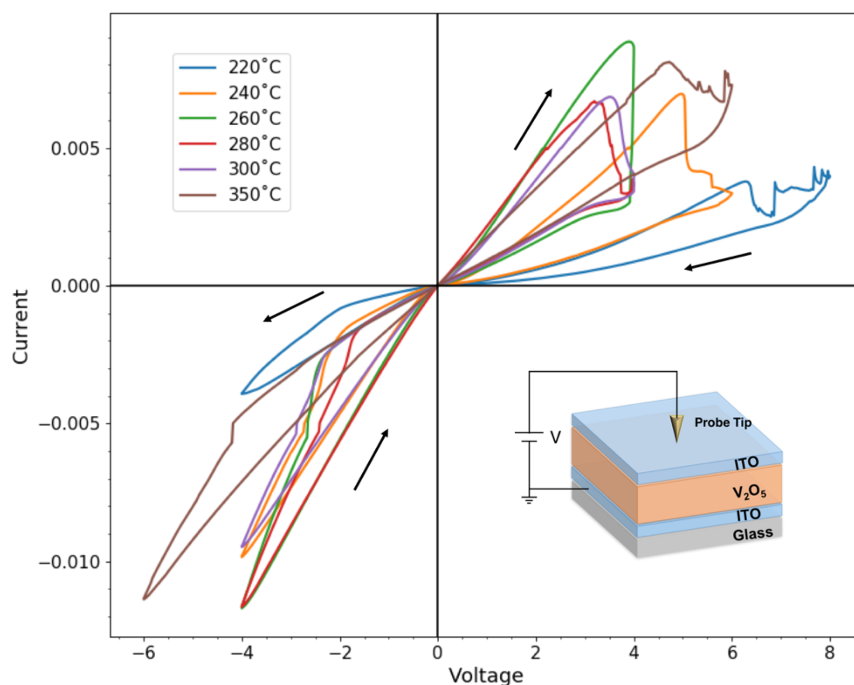

Figure 4.1. Switching voltages vs post annealing temperatures

Most of the devices show reversible bipolar switching behavior. Under high positive bias, the device can be switched from a low resistance state (LRS) to high resistance state (HRS) without the forming process. HRS can be reset to LRS with a sufficient negative bias. The switching voltages are shown to depend significantly on the annealing temperature. As the annealing temperature increases from 220˚C, the positive switching voltage (for HRS state) drops from 6.5 V and reaches its minimum value of 3 V at 280˚C. Negative switching voltage does not show a monotonic change and varies around -2.0 V. Making the annealing temperature larger than 280˚C results in an increase in the magnitude of both the positive and negative switching voltages. When annealing temperature is above 360˚C, the reversible resistive switching behavior disappears. Irreversible breakdown that causes the current to drop down to almost zero occurs when the positive or negative bias reaches about 4 V in magnitude. The results indicate that the switching behavior is optimized at an annealing temperature of 280˚C, and is very sensitive to annealing temperatures above 320˚C.

The shape of I-V curves also changes significantly. At low annealing temperatures, resistance of the device is high at low biases, and gradually decreases when the applied voltage increases, showing non-linear I-V characteristics. As the annealing temperature increases, this non-linear feature disappears, and the device exhibits Ohmic behavior for both LRS and HRS. The transition in low-bias I-V characteristics also indicates a change of band structure in the transport direction. The underlying mechanism for the change in electrical properties is attributed to the change in the chemical composition and atomic structure of $V_2O_5 \cdot nH_2O$ thin film during post-annealing process, which will be discussed in the following sections.

4.2.2 *TGA and X-Ray Diffraction Analysis*

$V_2O_5{\cdot}nH_2O$ xerogel thin film synthesized by the sol-gel process contains intercalated H_2O molecules [42] which can be gradually evaporated when annealed. First, we evaluate the water content in $V_2O_5{\cdot}nH_2O$ xerogel as a function of the annealing temperature. Thermogravimetric analysis (TGA) is performed on a thermal gravimetric analyzer in a N_2 atmosphere and the temperature is swept from room temperature to 500˚C with a heating rate of 5˚C/minute.

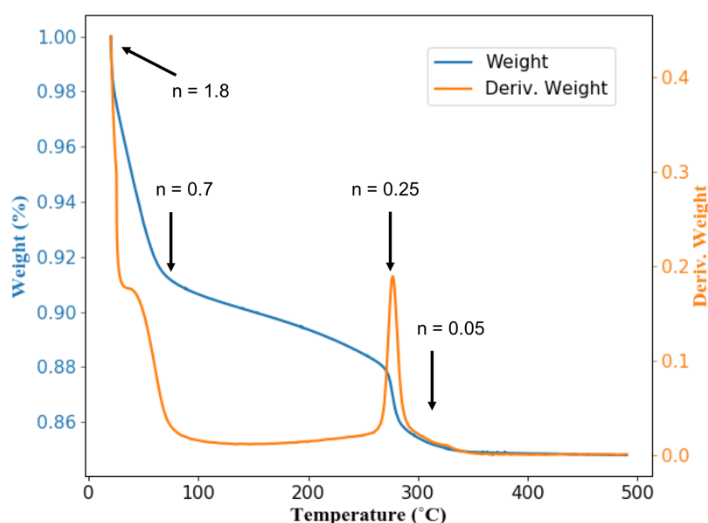

Figure 4.2. Thermogravimetric analysis (TGA) of V_2O_5 xerogel thin film

The obtained thermogravimetric trace is shown in Figure 4.2. It reveals the existence of 1.8 mole of water per mole of oxide at room temperature assuming H_2O is the only volatile phase in the xerogel film. The water content decreases rapidly and is characterized by the weight loss until the trace enters a gradually decreasing region above 70˚C. The value of n decreases to 0.25 at 270˚C. At this temperature, there is a sharp peak in derivative weight, indicating the loss of more tightly bounded water. At 300˚C, the n value decreases to 0.05 and beyond 350˚C the weight loss is no longer observed, suggesting that all the bounded water has been released. Comparing the TGA results with the I-V characteristics mentioned above, it is intuitive to relate the water content

with the change in switching properties. Below the optimized annealing temperature of 280˚C, the amount of H_2O molecules intercalated is relatively high, potentially creating a small barrier between V_2O_5 atomic layers that blocks the electron transport under low biases. As the annealing temperature rises beyond 360˚C, the bounded H_2O molecules fully evaporate, and this results in a more compact atomic structure solely consisting of crystalline V_2O_5. The barrier for the generation of mobile ions is increased, resulting in the disappearance of reversible switching.

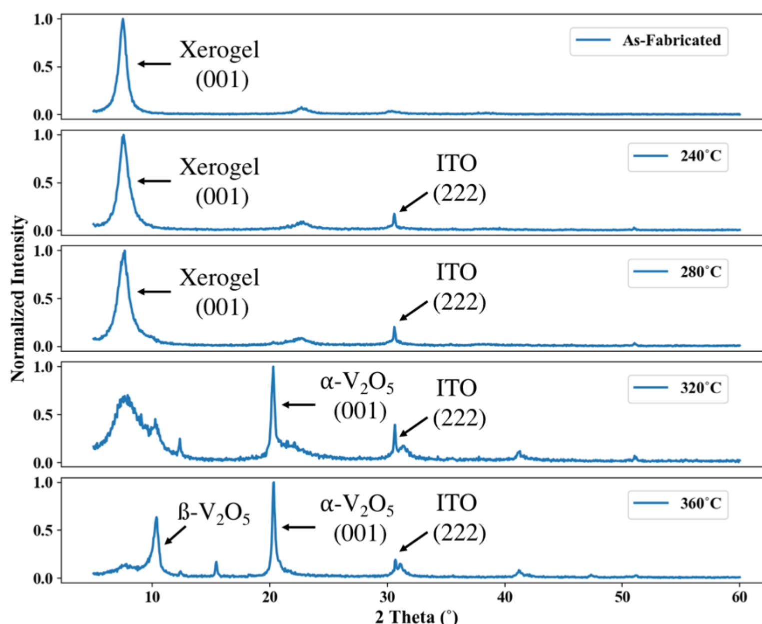

Figure 4.3. XRD results of ITO/V_2O_5/ITO structure

To further investigate the change in atomic structure of the device, X-Ray Diffraction (XRD) analysis is performed using a Bruker F8 Focus Powder X-ray diffractometer with an X-ray source of Cu K-α radiation with wavelength of 1.54 Å. The XRD patterns of ITO/V_2O_5/ITO structure at various annealing temperatures are shown in Figure 4.3. At low annealing temperatures below 280˚C, the dominant peak (001) is the one at 7.5˚, indicating a large interlayer spacing of 11.78 Å with the presence of intercalated water molecules. The broad full-width half-max (FWHM) of the dominant peak also indicates a large grain size, which originates from the randomized overlapping

of V_2O_5 nanoribbons during the sol-gel process. As the annealing temperature increases to 320˚C, the intensity of the low angle peak (7.5˚) drops significantly and other minor peaks at around 10˚ begins to emerge. The dominant peak at 20.6˚ corresponds to a crystalline orthorhombic α-phase V_2O_5 (001) peak. Interestingly, secondary peaks emerge at 11˚ and 12.5˚ as the annealing temperature becomes high, and they do not correspond to crystalline ITO or α-phase V_2O_5. These peaks belong to a different phase of V_2O_5, that is the ß-phase. The existence of ß-phase V_2O_5 in ITO/V_2O_5/ITO structure is surprising, as previous reports have suggested that ß-phase V_2O_5 is usually formed in rather extreme conditions: thermal heating of V_2O_5 powder at high temperature (T = 1073 K) and high pressure (P = 6.0 GPa) [73] or DC reactive magnetron sputtering at high substrate temperature (T = 550˚C) [74]. In the next section, it is discovered that the ultimate phase of V_2O_5 film grown by the sol-gel process after high temperature annealing depends significantly on the properties of substrate that the film is interfacing with.

4.3 DISCUSSIONS

4.3.1 *Asymmetrical Interfaces*

To investigate the structural transition of $V_2O_5 \cdot nH_2O$ xerogel film during annealing process and its dependence on the choice of substrate material, $V_2O_5 \cdot nH_2O$ thin film was coated on three different substrates first: soda-lime microscope glass slide, sapphire and ITO wafer. An ITO/V_2O_5/glass substrate structure was also fabricated to explore the effect of top ITO film which was deposited by RF magnetron sputtering using the same recipe. The XRD analysis results of the four structures are shown in Figure 4.4.

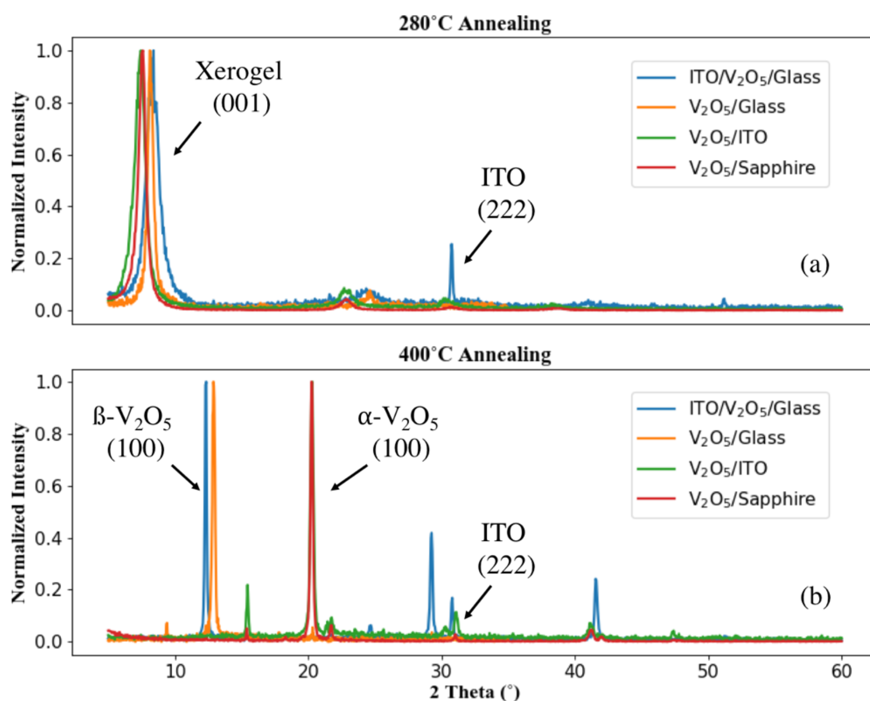

Figure 4.4. XRD results of ITO/V_2O_5/Glass, V_2O_5/Glass, V_2O_5/ITO and V_2O_5/Sapphire structures at annealing temperatures of (a) 280˚C (b) 400˚C

It is observed that at high annealing temperature (400˚C), the crystal structure of V_2O_5 film depends on the surface roughness of the substrate. When the substrate is crystalline and smooth (e.g. ITO or sapphire), the annealed V_2O_5 sol-gel film exhibits a regular α-phase with lattice constants of a = 11.512 Å, b = 5.364 Å, c = 4.368 Å [71]. However, when the substrate is amorphous and rough (e.g. soda-lime glass has a roughness of ~13 nm [75]), the crystal structure of V_2O_5 film is in ß-phase, and is identified by the dominant peak at 12.5° in the XRD analysis results.

The formation of ß-phase is explained by the different thermal expansion of substrate and V_2O_5 film at the V_2O_5/substrate interface. Figure 2.1 shows the scanning electron microscopy (SEM) images of V_2O_5 nanoribbons synthesized by sol-gel process from our previous work [60]. These nanoribbons are about 10 nm wide and 1 μm long and can easily fill into the valleys on a rough

substrate. At high annealing temperatures, the nanoribbons that directly come in contact with the substrate can experience high localized pressure due to different thermal expansion coefficients (eg. CTE is 9.5 ppm/K for soda-lime glass [76] and 51.6 ppm/K for V_2O_5 [77]). The local high pressure provides the environment for the formation of ß-phase V_2O_5 at the substrate/V_2O_5 interface, which acts as a seeding layer and eventually determines the crystal structure of V_2O_5 film on the top. Whereas when the substrate surface is smooth, the overlap between substrate and V_2O_5 nanoribbons is minimized and the local pressure does not reach the threshold for creating ß-phase V_2O_5. Therefore, the film exhibits a normal crystal structure of α-phase V_2O_5. Note that in ITO/V_2O_5/glass structure, the whole V_2O_5 film only exhibits ß-phase at 400°C, contrary to the α-V_2O_5 formed in V_2O_5/ITO substrate structure. In this case, the V_2O_5 xerogel film becomes the rough substrate (surface roughness is around 30 nm [60]). During the subsequent magnetron sputtering deposition of top ITO, a firm interface with large contact area is generated. ß-phase V_2O_5 is thus formed at high annealing temperature due to different thermal expansion of ITO and V_2O_5 (CTE is 7.2 ppm/K for ITO [78]).

From the above analysis, we conclude that the ITO/V_2O_5/ITO device has asymmetrical top and bottom interfaces. When the annealing temperature increases above 280°C, α-V_2O_5 starts to form at the bottom ITO/V_2O_5 interface while ß-V_2O_5 forms at top ITO/V_2O_5 interface. The active region of xerogel phase with large interlayer spacing is consumed and keeps shrinking. The phase distribution of the device is illustrated in Figure 4.5. The resistive switching from LRS to HRS only occurs at positive bias, implying that the oxygen ion migration only happens between top ITO and V_2O_5 layers. When ß-V_2O_5 is formed at the top interface, it acts as a thin barrier layer for oxygen ion migration, where the xerogel region remains the source for mobile oxygen ions. This is consistent with the reduced ON/OFF ratio and increased switching voltages at annealing

temperatures above 320˚C. At the same time, the α-V_2O_5 region at the bottom interface keeps growing and reduces the thickness of xerogel region. At a high annealing temperature of 400˚C, the xerogel phase is thoroughly exhausted, accompanied by the disappearance of reversible resistive switching. This confirms that neither α-V_2O_5 nor ß-V_2O_5 has the capability of generating oxygen ions and reacting with the ITO electrode to achieve reversible switching. To further investigate this claim, the results of first-principle calculations are presented in the following section.

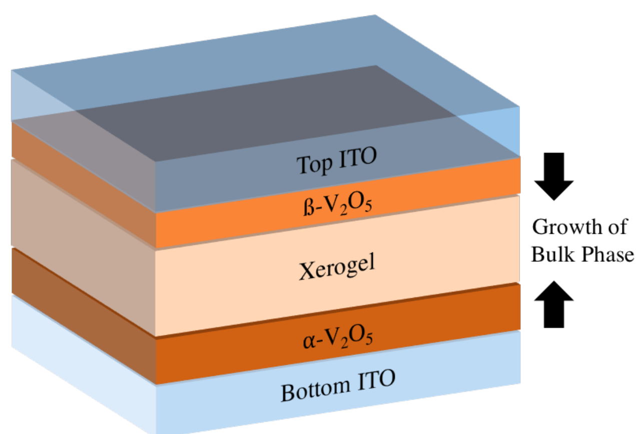

Figure 4.5. Phase distribution of ITO/V_2O_5/ITO device at annealing temperature above 280˚C and below 400˚C

4.3.2 *Microscopic Insights*

We have confirmed that the presence of xerogel phase is essential for creating oxygen vacancies in V_2O_5 layer which is responsible for the resistive switching from LRS to HRS. First-principle calculations of oxygen vacancy formation energies in three different phases of V_2O_5 have been performed to obtain microscopic insights into our results. For all calculations the spin polarized periodic DFT code Vienna Ab-initio Simulation Package [79, 80] was employed, in which valence electronic states are described within a plane wave basis set with a cutoff energy of 520 eV. The

core electrons were represented using projector augmented wave (PAW) pseudopotential [81] and explicitly treated eleven valence electrons for vanadium ($3p^6 3d^4 4s^1$), six for oxygen ($2s^2 2p^4$), and one for hydrogen. The Perdew-Burker-Ernzerhof [82] within the Generalized Gradient Approximation (GGA) functional [83] was used for the exchange-correlation energy, including rotationally invariant GGA+U [84] with a coulomb repulsion of U= 3.25 eV to account for the strongly correlated electrons in vanadium d-states [85]. Structural optimization was obtained by relaxing the atoms using conjugate-gradient method [86] with the use of a single (gamma) k-point.

Three different phases of V_2O_5 have been modeled to evaluate their oxygen vacancy formation energies, including α-phase, ß-phase, and xerogel phase $V_2O_5 \cdot 0.5\ H_2O$. The value of n = 0.5 was chosen according to the TGA measurements at the optimized annealing temperature of 280˚C. The atomic structures denoted by distinct oxygen positions are shown in Figure 4.6. Reduced V_2O_5 calculations were carried out on 1 × 4 × 2 supercell of $V_{32}O_{79}$ for α-V_2O_5 (Figure 4.6(a)) and 2 × 2 × 3 supercell of $V_{48}O_{119}$ for ß-V_2O_5 (Figure 4.6(b)). $V_2O_5 \cdot n\ H_2O$ xerogel consists of bilayer V_2O_5 layers intercalating H_2O molecules with an interlayer spacing of 10.49 Å. Structure of $V_2O_5 \cdot 0.5\ H_2O$ was obtained by first optimizing the $V_2O_5 \cdot\ H_2O$ structure (2 × 4 × 1 supercell) reported in [87], and removing half of H_2O molecules followed by relaxing the structure again. As the water molecules in [87] have two different orientations, we have examined the cases of removing either type of water molecule (Figure 4.6(c), (d)). An oxygen atom was then removed from the resulting structure for the oxygen vacancy formation energy calculations.

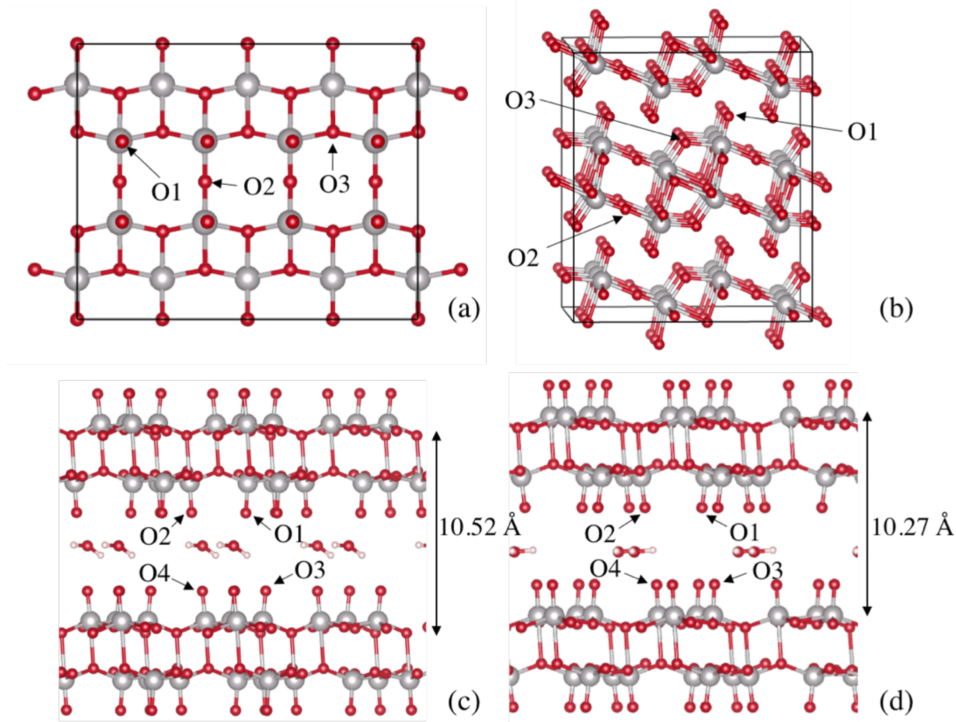

Figure 4.6. Atomic structures of (a) α-V_2O_5. (b) ß-V_2O_5. (c) V_2O_5·*0.5* H_2O, type I. (d) V_2O_5·*0.5* H_2O type II.

The vacancy formation energy was calculated according to the equation

$$\Delta E^{V}_{form} = E^{V} - E^{pristine} + \frac{1}{2}\mu_{O_2} \tag{4.1}$$

where E^V is the energy of the system with a vacancy, $E^{prisine}$ is the energy of the system without the vacancy, and μ_{O_2} is the energy of molecular oxygen. In α-V_2O_5, only O1 vacancy, where the removed oxygen atom is bonded with a single vanadium atom has been taken into consideration as it has been reported to have the lowest formation energy [88]. The computed formation energy is 1.65 eV and it is used as a reference to evaluate how easily the other structures could generate oxygen vacancies respectively.

Table 4.1. Energies of formation of oxygen vacancies in ß-V_2O_5 and V_2O_5·*0.5* H_2O.

Vacancy Site	Energy of Formation (eV)	Difference from α-V_2O_5 (eV)

β-V_2O_5, O1 vacancy	1.604	-0.046
β-V_2O_5, O2 vacancy	2.543	0.893
β-V_2O_5, O3 vacancy	2.034	0.384
$V_2O_5 \cdot 0.5$ H_2O type I, O1	2.230	0.580
$V_2O_5 \cdot 0.5$ H_2O type I, O2	1.367	-0.283
$V_2O_5 \cdot 0.5$ H_2O type I, O3	2.205	0.555
$V_2O_5 \cdot 0.5$ H_2O type I, O4	1.302	-0.348
$V_2O_5 \cdot 0.5$ H_2O type II, O1	1.186	-0.464
$V_2O_5 \cdot 0.5$ H_2O type II, O2	0.957	-0.693
$V_2O_5 \cdot 0.5$ H_2O type II, O3	1.819	0.169
$V_2O_5 \cdot 0.5$ H_2O type II, O4	-0.628	-1.022

The calculated oxygen vacancy formation energies in ß-V_2O_5 and two types of $V_2O_5 \cdot 0.5$ H_2O are listed in Table 4.1. Energies of formation of oxygen vacancies in ß-V_2O_5 and $V_2O_5 \cdot 0.5$ H_2O. Note that in the xerogel structures, bridging oxygen sites that are bonded to multiple vanadium atoms are not considered as they are less likely to be removed from the system. The lowest formation energy found in ß-V_2O_5 is 1.604 eV at O1 site where oxygen atom is bonded with a single vanadium atom. The difference of formation energy compared to α-V_2O_5 is only 46 meV, suggesting that both structures have similar capability of generating oxygen vacancies. In the first type of $V_2O_5 \cdot 0.5$ H_2O, both O2 and O4 vacancy sites have lower formation energies than α-V_2O_5 case. In the second type of $V_2O_5 \cdot 0.5$ H_2O, the formation energies are further reduced and even becomes negative in O4 vacancy site, implying that the release of oxygen atoms and generation of oxygen vacancies is a thermodynamically favored process. Taking a closer look at the resulting structure after removing the oxygen atom from O4 site, it is found that one intercalated H_2O molecule has been attracted to the V_2O_5 laminar and filled the vacancy site (Figure 4.7(b)). Due to

the heavy reconstruction occurring after the removal of oxygen atom, the energy of the system decreased dramatically.

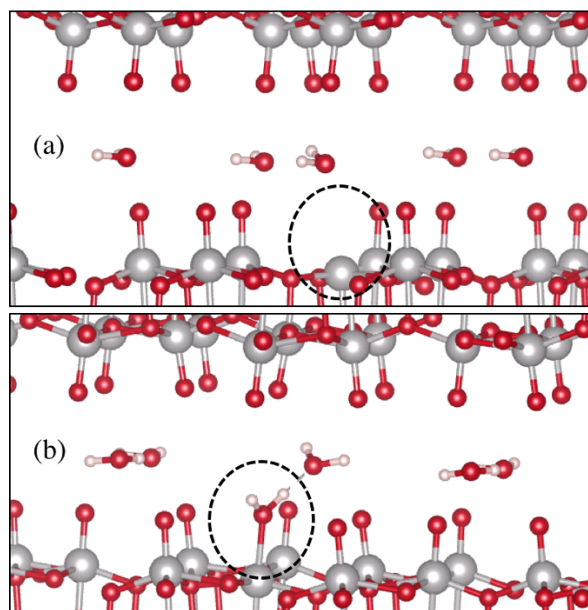

Figure 4.7. Atomic structure after removing oxygen atom and relaxation for (a) V_2O_5·*0.5* H_2O type II, O3 site. (b) V_2O_5·*0.5* H_2O type II, O4 site.

Our simulation results are in good agreement with the experiments and the physical models proposed for the switching mechanism. When intercalated H_2O molecules still exist in V_2O_5 film, the interlayer spacing is enlarged so that the removal of single-bonded oxygen atoms becomes easier, resulting in a significant decrease in formation energies of oxygen vacancy. The negative formation energy of oxygen vacancy site (O4) in type II xerogel structure also qualitatively agrees with the experimental observation that the color of fabricated device usually turned from orangish to greenish after a few weeks, indicating a spontaneous reduction of oxidation states. Above the annealing temperature of 360˚C, H_2O molecules have been fully removed from V_2O_5 film so that

only α-V_2O_5 and ß-V_2O_5 exist. Reversible switching does not occur due to the relatively high formation energies of oxygen vacancies in these two compact crystalline phases.

4.4 SUMMARY OF THE IMPACT OF PHASE TRANSITION

In this chapter, we investigate the effects of post annealing temperatures on the switching characteristics of ITO/V_2O_5/ITO device. At annealing temperatures below 280˚C, intercalated water molecules increase the barrier for electron transport in V_2O_5 xerogel film and thus results in a non-linear I-V characteristics and higher switching voltages. When annealing temperature is above 300˚C, a phase transition starts to occur at both ITO/V_2O_5 interfaces: α-V_2O_5 is formed at the bottom and ß-V_2O_5 is formed at the top, which gives decreased ON/OFF ratio and higher switching voltages. The reversible resistive switching requires the existence of xerogel phase in the system. The annealing temperature is optimized at 280-300˚C. Ab initio simulations confirm that the formation energies of V_2O_5 xerogel is lower than both α-V_2O_5 and ß-V_2O_5, in agreement with the experimental evidence that reversible resistive switching only occurs when xerogel phase still exists in the V_2O_5 thin film synthesized by sol-gel process.

Chapter 5. BIPOLAR RESISTIVE SWITCHING CHARACTERISTICS OF THERMALLY EVAPORATED V_2O_5 FILM

In previous chapters, a sol-gel process was employed to fabricate the V_2O_5 thin film due to the advantages of simplicity and low-cost feature. The synthesized film is in xerogel phase with intercalated H_2O molecules, described by a chemical formula of $V_2O_5 \cdot nH_2O$. The water content n decreases with increased annealing temperature, and intercalated water is fully evaporated from the film above 350˚C. Reversible resistive switching only occurs with the presence of intercalated H_2O molecules. *Ab initio* calculations reveal that with the enlarged interlayer spacing supported by H_2O molecules, the formation energy of oxygen vacancy is significantly reduced in V_2O_5 xerogel compared to other crystalline phases such as α-V_2O_5 and ß-V_2O_5, so that it is easier to create mobile oxygen ions that can migrate across the ITO/V_2O_5 interface reversibly. However, the film synthesized by sol-gel process has poor uniformity and its conductivity and switching voltages are sensitive to the annealing temperature due to variable water content in the film, making it incompatible with modern IC fabrication technology. Moreover, the device fabricated from sol-gel process suffers from the issue of short lifetime due to the degradation of V_2O_5 thin film. The color usually transforms from orangish to greenish within one month, indicating a reduction of valence states from V^{5+} to V^{3+}/V^{4+}. Ab initio simulation also shows that some oxygen vacancy sites may have negative formation energy of oxygen vacancy, suggesting that the creation of oxygen vacancies can be spontaneous in $V_2O_5 \cdot nH_2O$ film.

To overcome the downsides mentioned above for the sol-gel process, we have deposited V_2O_5 thin film by thermal evaporation and employed it in the ITO/V_2O_5/ITO structure in this work. Bipolar resistive switching characteristics is preserved and the dependence of I-V characteristics

on annealing temperature is investigated. *Ab initio* calculations are performed to examine the formation energies of amorphous V_2O_5 compared with its bulk crystalline phase.

5.1 METHODS

ITO coated glass wafer with a sheet resistance of 20 Ω/sq was used as substrate and common bottom contact. Thin film of V_2O_5 was then deposited by thermal evaporation in a vacuum deposition chamber. V_2O_5 powder was used as source material and evaporated from a tungsten boat. The deposition pressure in the chamber was between 5×10^{-6} Torr to 1×10^{-5} Torr. No internal substrate heater was used and the distance between source and substrate was approximately 50 cm. Thickness of the deposited V_2O_5 thin film was measured by the built-in crystal monitor and three different thickness was obtained: 11.4 nm, 23.5 nm and 53.0 nm. The as-fabricated V_2O_5 thin film is almost transparent with slight yellowish color. The top layer of ITO was deposited on top of the V_2O_5 thin film by magnetron sputtering and patterned to have circular shape with a diameter of 2 cm. Two different ITO thickness was chosen: 60 nm and 120 nm. The fabricated ITO/V_2O_5/ITO device was then annealed in a box furnace in ambient environment at temperatures ranging from 150˚C to 375˚C. Current-voltage characteristics of the device was measured by Keithley 4200 SCS parametric analyzer and a custom-built probe station.

First-principle calculations of oxygen vacancy formation energies of both crystalline and amorphous V_2O_5 have been performed to obtain microscopic insights into our results. For all calculations, the spin polarized periodic DFT code Vienna Ab-initio Simulation Package (VASP)[79, 80] was employed, in which valence electronic states were described within a plane wave basis set with a cutoff energy of 520 eV. The core electrons were represented using projector augmented wave (PAW) pseudopotential[81]. The calculations explicitly treated eleven valence electrons for vanadium ($3p^6 3d^4 4s^1$), six for oxygen ($2s^2 2p^4$), and one for hydrogen. Exchange

–correlation energy was treated by using the Perdew-Burker-Ernzerhof [82] within the Generalized Gradient Approximation (GGA) method [83]. To overcome the limitations of GGA with respect to the strongly correlated electrons in vanadium d-states, rotationally invariant GGA+U[84] with a coulomb repulsion of U = 3.25 eV was applied to the system [85]. Structural optimization was performed by relaxing the atoms using conjugate-gradient method [86] with the use of single gamma k-point.

Bulk α-V_2O_5 forms a layered orthorhombic structure with lattice constants a = 11.512 Å, b = 3.564 Å, and c = 4.368 Å[71], and the primitive cell contains two formula units (14 atoms). This cell consists of distorted corner-sharing and edge-sharing octahedral with each vanadium atom surrounded by six oxygen atoms. In order to compare the present experiments with computations, amorphous V_2O_5 was modeled by the melt-quench process. Our modeling of amorphous V_2O_5 started from the corresponding crystalline material and used ab initio molecular dynamics simulations included in the VASP code. An orthorhombic α-V_2O_5 system consists of 112 atoms (1 × 4 × 2 supercell) was first fully melted at 2000 K with 18-ps-long time steps. Then the system was quenched from 2000 K to 300 K in 4000 more MD runs with 12-ps-long steps. After another 3-ps-long MD run at 300 K to stabilize the system, the last snapshot of this simulation was optimized at zero Kelvin to obtained to fully quenched amorphous state. The obtained amorphous structure is shown in Figure 5.1. Formation energies of the oxygen vacancies were calculated by removing one oxygen atom from random sites in the amorphous V_2O_5.

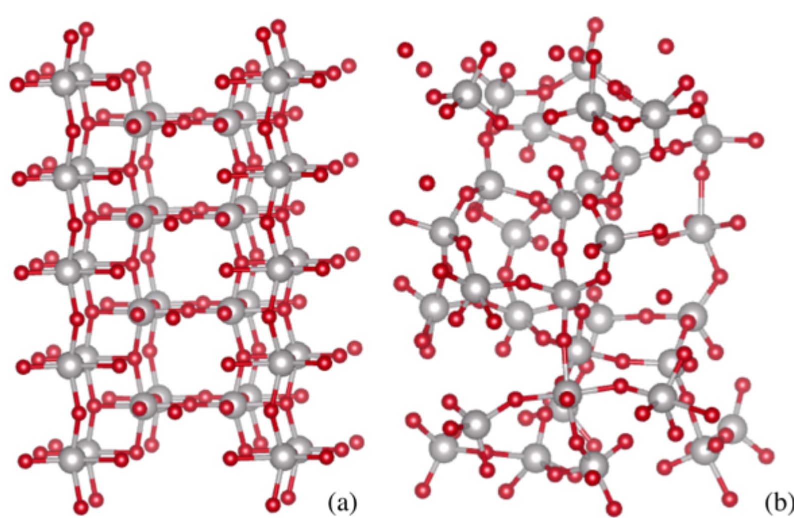

Figure 5.1. Bulk-and-stick plots of the simulated (a) orthorhombic α-V_2O_5 (b) amorphous V_2O_5

5.2 Experimental Results

The I-V characteristics of the as-fabricated devices are shown in Figure 5.2, and the bias setup is shown in the inset. All of the devices exhibited bipolar switching characteristics before any post annealing process, except for the devices with 11.4 nm V_2O_5 layer (results no shown in the plot). The devices show LRS in their pristine states, and can be programmed to HRS under a positive bias of +2.5 V. A negative bias of −2.5 V can erase the programmed state and change the resistance back to LRS. The switching occurs at similar voltage levels for the three tested devices with different thickness of V_2O_5 and/or ITO layers. However, it is counter-intuitive that the current level increases with thickness of V_2O_5 and ITO layer. This behavior can be explained by the fact that top electrode (essentially the probe tip) and bottom electrode are asymmetrical in geometry and ITO is not a perfect metallic conductor that allows current to fully spread across its covered area. Although an increase in thickness enlarges the distance of the current path in vertical direction, it

also supports more spreading of current in horizontal plane, giving rise to the overall increase in current.

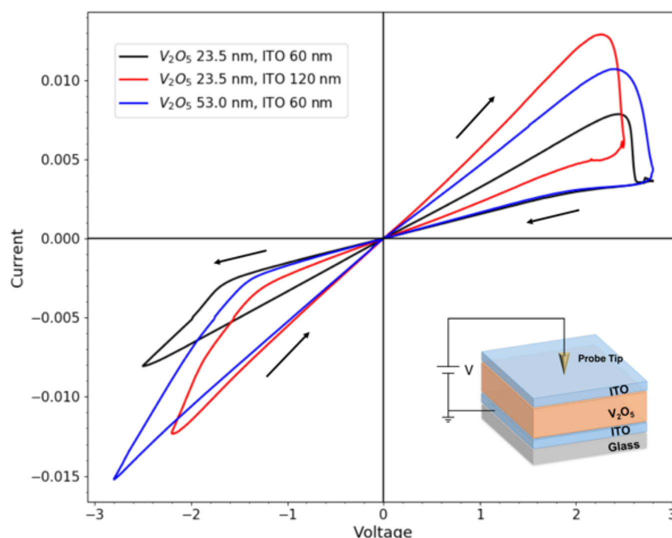

Figure 5.2. I-V characteristics of as-fabricated devices

It is observed that the device with 11.4 nm thick V_2O_5 layer does not show reversible switching behavior. Instead, an irreversible breakdown occurs at + 2.5 V bias, resulting in partial ablation of the ITO film underneath the probe tip. The high electric field and current density generated in V_2O_5 thin film are likely to be the cause of such breakdown. The result suggests a lower limit for the thickness of V_2O_5 layer.

In our previous study, V_2O_5 thin film synthesized by sol-gel process suffers from dramatic change in both atomic structure and electrical conductivity during the post annealing process at various temperatures due to the variable intercalated water content. To test the thermal stability of the ITO/V_2O_5/ITO structure fabricated from thermal evaporation, the same device (23.5 nm V_2O_5 and 60 nm ITO) has been annealed at temperatures increasing from 200˚C to 375˚C, followed by I-V measurements after each annealing step. The results are shown in Figure 5.3.

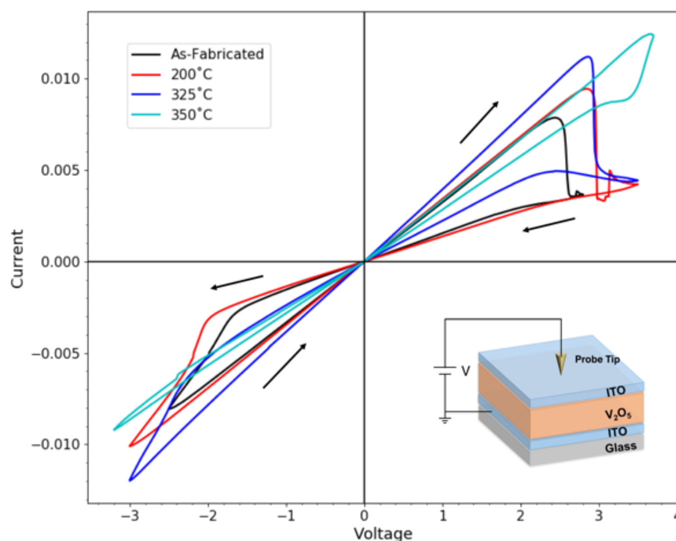

Figure 5.3. Dependence of I-V characteristics on annealing temperatures

Compared to the as-fabricated state, the positive switching voltage increases for about 500 mV after a soft baking at 200˚C, and less increase is observed for negative switching voltage. The device then shows stable I-V characteristics up to annealing temperatures of 300˚C. Further increase in annealing temperature to 325˚C raises the current in both LRS and HRS, resulting in a degradation in ON/OFF ratio. At 350˚C, the switching voltage increases up to +3.7 V and switching behavior is almost negligible. Bipolar switching fully disappears when the annealing temperature increases to 375˚C. Overall the device exhibits much improved thermal stability over the devices fabricated from the sol-gel process.

The disappearance of bipolar switching characteristics at high annealing temperatures can be explained by the re-crystallization of the amorphous V_2O_5 thin film. It has been reported[89] that amorphous V_2O_5 films deposited by thermal evaporation crystallize and transform to an orthorhombic phase when annealed in an oxygen rich environment at 400˚C. Note that indium tin oxide is a degenerate n-type semiconductor rich in oxygen vacancies, and its structure and electrical properties also changes dramatically with annealing temperature and environment[90].

The annealing of ITO films in air will lead to the filling of oxygen vacancies due to their reaction with free oxygen. According to our proposed switching mechanism, the loss of oxygen vacancies in the ITO electrode can also result in the disappearance of resistive switching behavior. To rule out this possibility, pre-annealing of amorphous V_2O_5 film at 400°C was performed in ambient air followed by deposition of the top ITO electrode by magnetron sputtering. No reversible switching was found in the as-fabricated devices, indicating that the transition of the amorphous V_2O_5 film into a crystalline phase is responsible for the resistive switching.

5.3 Simulation and Discussion

5.3.1 *Simulation of Oxygen Vacancy Formation Energy*

Formation of oxygen vacancies in V_2O_5 layer plays an important role in inducing the resistive switching behavior in ITO/V_2O_5/ITO structure. *Ab initio* calculations have been performed to investigate the formation energies of oxygen vacancies in amorphous V_2O_5 structure compared to crystalline orthorhombic α-V_2O_5 phase.

The energy of vacancy formation energy was calculated according to equation (4.1), where E^V is the energy of the system with a vacancy, $E^{pristine}$ is the energy of the system without the vacancy, and μ_{O_2} is the energy of molecular oxygen. In α-V_2O_5, only vacancy site where the removed oxygen atom is bonded with a single vanadium atom has been taken into consideration as it has been reported to have the lowest formation energy [88]. The computed formation energy is 1.65 eV and it is used as a reference to evaluate how easily the amorphous structure can generate oxygen vacancies. Among the 80 oxygen atoms in the amorphous structure, we randomly picked nine different oxygens and the calculated formation energies are listed in Table 5.2.

Table 5.2. Energies of formation of oxygen vacancies in amorphous V_2O_5.

Vacancy Site	Energy of Formation (eV)	Difference from α-V_2O_5 (eV)
O(1) a-V_2O_5	0.428	-1.222
O(2) a-V_2O_5	1.000	-0.650
O(3) a-V_2O_5	1.090	-0.560
O(4) a-V_2O_5	1.609	-0.041
O(5) a-V_2O_5	1.687	0.037
O(6) a-V_2O_5	1.892	0.242
O(7) a-V_2O_5	1.976	0.326
O(8) a-V_2O_5	2.090	0.440
O(9) a-V_2O_5	2.148	0.498

We observe that, among the nine oxygen vacancy sites, three have significantly lower formation energies than the bulk case, which is to be expected given the metastability of the amorphous structure. Compared to the bulk form where all atoms tend to remain fixed in their original positions in the lattice after removing one oxygen, the atoms in the amorphous structure could experience more significant movements and thus result in a lower energy states. Two oxygen vacancy sites have similar formation energies and the remaining four sites have significantly higher formation energies. Therefore, these simulations show that it is easier to create oxygen vacancies in amorphous V_2O_5 than the orthorhombic bulk phase, which is consistent with our previous experimental observations.

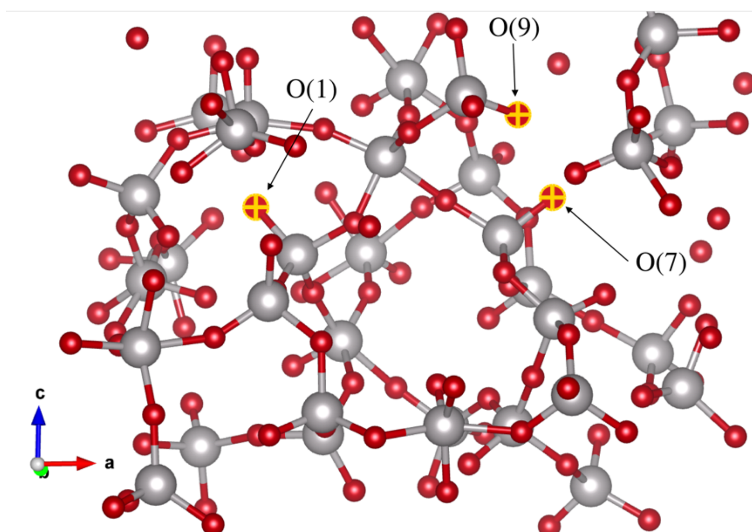

Figure 5.4. Illustration of oxygen vacancy sites O(1), O(7) and O(9).

It is normally difficult to qualitatively predict the formation energy of a specific oxygen site in an amorphous structure compared to its crystalline counterpart, as the ionic environment that the oxygen atom resides is always irregular and complicated. However, by taking a closer look at the sampled oxygen vacancy sites, some correlation can be found between the V-O bond lengths and the corresponding formation energies of oxygen vacancies, which we report here. Figure 5.4 illustrates the positions of three calculated oxygen sites: O(1), O(7) and O(9), which are all single-bonded to a neighboring vanadium ion. The V-O bond length of the oxygen site that has the lowest formation energy in crystalline V_2O_5 is 1.608 Å. The V-O bond lengths of O(1), O(7) and O(9) sites are 1.649 Å, 1.606 Å and 1.605 Å, respectively. Generally speaking, the larger the bond length, the smaller the bond energy. For the O(1) site, the V-O bond length is much larger than in the crystalline phase, which is consistent with its significantly lower formation energy. For O(7) and O(9), the bond length is slightly smaller than in the crystalline phase, corresponding to a higher formation energy. Overall, by transforming V_2O_5 from the crystalline to the amorphous phase, a

wider distribution of bond lengths is achieved, resulting in the formation energy deviating from that in crystalline phase in both directions.

Our calculations have confirmed that the formation energies of oxygen vacancies can be lowered in the amorphous structure without the presence of intercalated H_2O molecules, which enables the reversible resistive switching in the ITO/V_2O_5/ITO devices. The removal of intercalated water also improves the lifetime of the device. Excellent reversible switching characteristics are still preserved after seven months of exposure in the air, compared to the one-month lifetime for the device fabricated from the sol-gel process.

5.3.2 *Localized Bipolar Resistive Switching Induced by Joule Heating*

The bipolar resistive switching characteristics discussed in Chapter 3, 4 & 5 originate from mechanism similar to that illustrated in Figure 3.5. When an external electric field is applied, oxygen vacancies are generated in V_2O_5 layer and mobile oxygen ions migrate into ITO electrode. The filling of oxygen vacancies in ITO layer is partially responsible for the increase in resistance observed after resistive switching. The high resistance state (HRS) is found to be highly localized, that is, if the probe tip is moved to another nearby spot, the HRS can no longer be detected.

The resistive switching itself is also highly localized. A test scheme has been set up to confirm this hypothesis shown in Figure 5.5. The tested sample is a ITO/amorphous V_2O_5/ITO device fabricated using the recipes described in previous sections. The thickness of amorphous V_2O_5 is 55 nm, and the thickness of top ITO electrode is 120 nm. The test is performed in the following steps. The probe tip (2 μm diameter) is placed on the center point at the beginning, and a forward bias is applied to introduce the resistive switching. Then the probe tip is moved from P1 to P8 successively, followed by the same forward bias to test the resistive switching characteristics of

each individual point. Low-bias measurements are also performed to record the LRS and HRS at each point. The spacing of two neighboring points is set to be 10 μm.

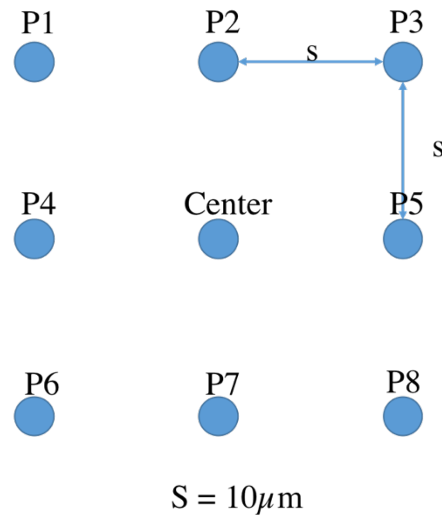

Figure 5.5. Test scheme setup for distribution of switching characteristics

The measured distribution of switching characteristics is shown in Figure 5.6. Resistive switching from LRS to HRS is found in all the points P1 – P8, although P2, P5 and P8 shows reduced switching behavior, likely due to contact problem and measurement errors. The switching voltages are also similar to the center point. This observation confirms that initial switching occurring at the center point has little impact on the initial resistance and switching characteristics of its neighboring points outside of 10 μm range.

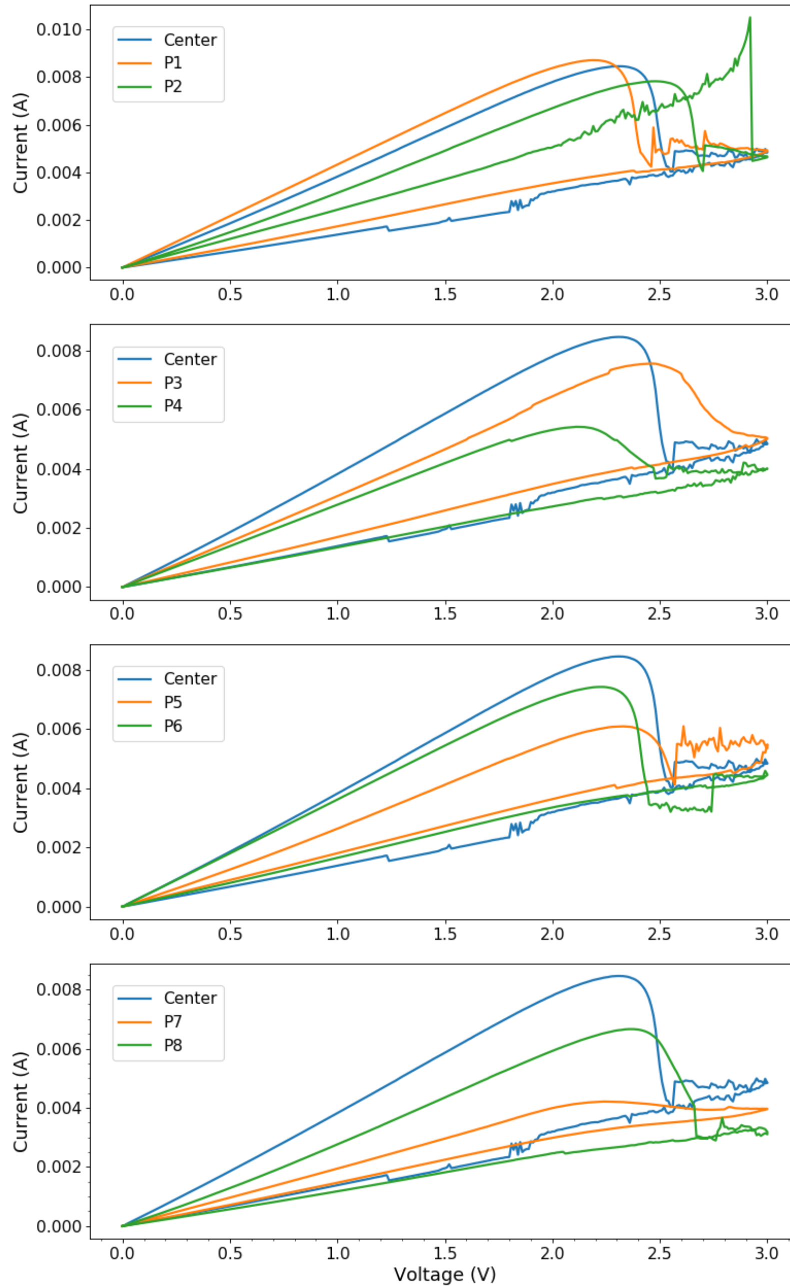

Figure 5.6. Switching distribution showing the localized switching characteristics

The low bias resistance of the nine points before and after switching is also measured. The results are shown in Figure 5.7. It is observed that the switching occurring at the center point has slight impact on the LRS of its neighbors and overall a decrease in initial current is detected. The

ON/OFF ratio is being affected as well, although it is hard to conclude that the degradation is thoroughly due to the center point rather than measurement error or non-uniformity of the film.

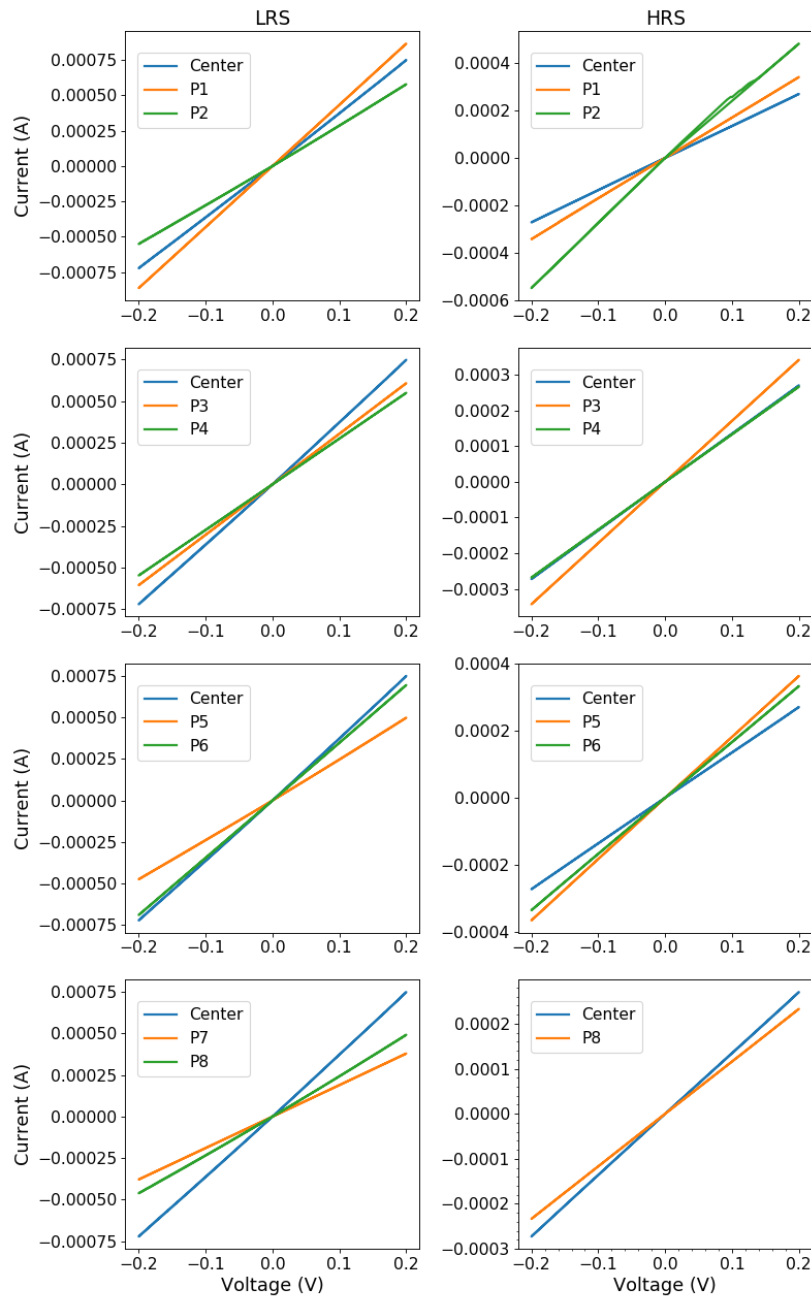

Figure 5.7. Distribution of LRS and HRS of all the nine points tested

The measurements presented above confirm that both the switching and HRS are highly localized. Initially we thought that this was due to the localized distribution of electric field in the

direction of current flow. Preliminary 3D TCAD simulation has been performed to investigate the distribution of electric field in ITO/V_2O_5/ITO device and the results are shown in Figure 5.8. Note that this simulation is designed for xerogel V_2O_5 film, so the thickness of V_2O_5 is chosen to be 0.8 μm.

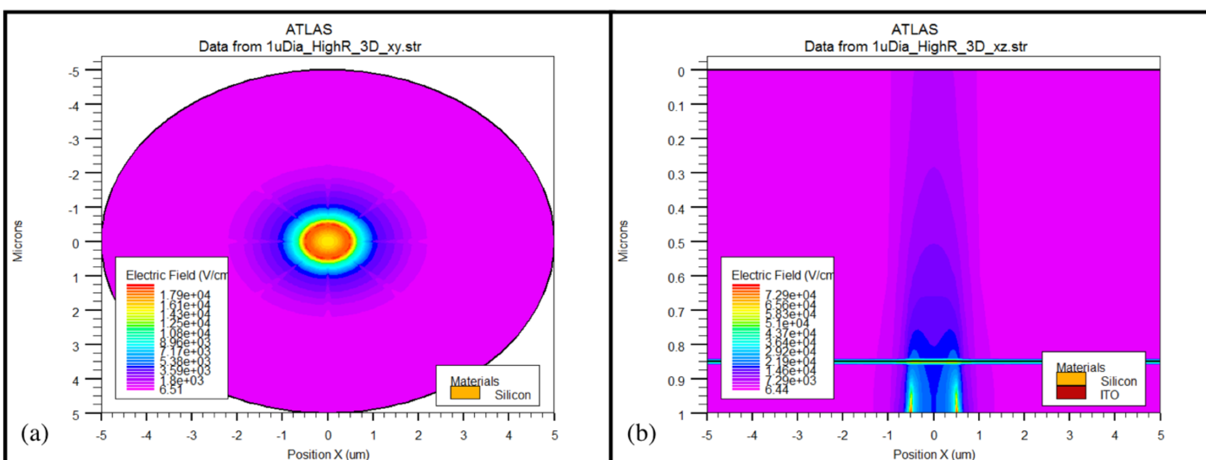

Figure 5.8. 3D TCAD simulation results of electric field distribution in ITO/V_2O_5/ITO structure. (a) top view. (b) cross section view.

The simulation suggests that when the contact diameter is small (1 μm), the electric field in V_2O_5 layer is clustered underneath the metal contact (essentially the probe tip) and does not spread widely across the V_2O_5 layer. Based on the simulation, the current in vertical direction should also be confined by the size of metal contact. It should have little dependence on the area of V_2O_5 or top ITO layer. However, the conclusion derived from the simulation is in contrary to the experiments. The area of top ITO layer is demonstrated to have significant impact on the I-V and resistive switching characteristics of the ITO/V_2O_5/ITO device.

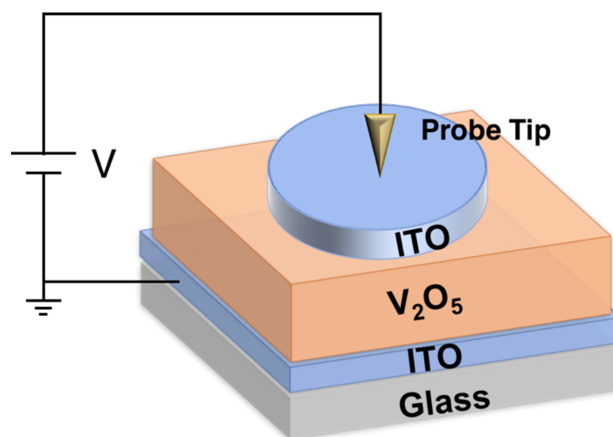

Figure 5.9. Structure of patterned top ITO devices.

To investigate the influence of top ITO size, the top ITO layer is patterned by a shadow mask during the magnetron sputtering process. The diameter of top ITO electrode ranges from 1 mm to 4 mm, and the device structure is shown in Figure 5.9. Note that the V_2O_5 is synthesized by the sol-gel process followed by 280˚C post annealing. Similar behavior can be found in thermally evaporated V_2O_5 devices as well.

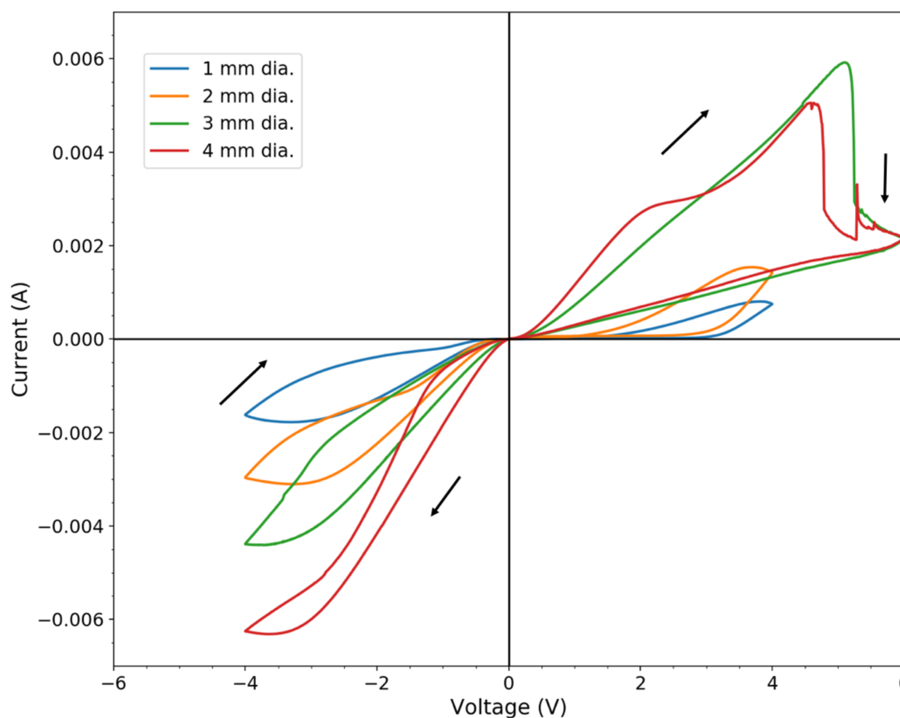

Figure 5.10. I-V characteristics of devices with patterned top ITO layer

The measured I-V characteristics of the ITO/V_2O_5/ITO devices with patterned top ITO layer are shown in Figure 5.10. It is obvious that both the current level and the curvature of the traces have changed significantly with various top ITO area. The low-bias current increases and is found to be proportional to the top ITO area, indicating that the current spreads over the top ITO layer at least within 4 mm diameter range. All the curves show non-Ohmic behavior, contrary to the linear I-V characteristics reported in previous chapters. The linearity seems to increase with increasing the area of top ITO layer. Reversible resistive switching is not detected in the tested voltage range in devices with 1 mm and 2 mm diameters, but it can occur when the voltage is further increased (results not shown). Switching is found in the other two devices, but with significantly higher switching voltages (+5.5 V compared to +2.5 V reported before).

The results suggest an apparently different distribution of current in ITO/V_2O_5/ITO devices from what is shown in the simulation presented previously. The current is not confined underneath

the small probe tip; it is actually spreading all over the top ITO layer. This observation seems to be in contrary to the localized switching characteristics mentioned above: if the current spreads across the whole ITO layer, then the interfacial switching could occur at any place in the current path, and thus HRS can be detected in other neighboring spots as well. Another interesting observation is that the switching voltage decreases with increasing area of ITO layer, opposite to the observation described in Chapter 3 that it decreases with decreasing area of top metal contact. It is again contrary to the model that current is confined underneath the probe tip.

A preliminary physical model is proposed here to explain the contradictory observations discussed above and it is illustrated in Figure 5.11. It is proposed that although the current eventually spreads over the ITO layer, it is still well confined and has high density when it first comes out of the top probe tip. Such high current density introduces Joule heating beneath the probe tip, creating a localized temperature increase at the top ITO/V_2O_5 interface in the region under the probe tip. The increase in temperature accelerates the generation of oxygen vacancies, and introduces the occurrence of oxygen ion migration discussed previously. Whereas for the rest of the interfacial region, the reaction is limited due to lower temperature, which explains the localized switching characteristics. This model can also explain the fact that the switching voltage increases with reduced top ITO area: when the top ITO area is small, the current density at probe tip/top ITO interface is also reduced. In order to create the sufficient high temperature to introduce the reaction, voltage has to be increased to provide more current.

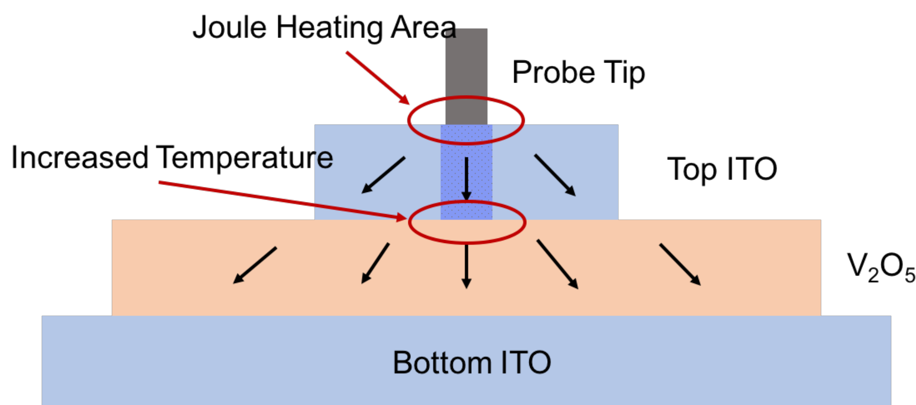

Figure 5.11. Illustration of the Joule heating model

It is worthy to point out that the model described above is in its very early stage and will need further proof from either experiments or modeling in the future.

5.4 Summary of Thermally Evaporated V_2O_5 Thin Film Devices

In this chapter, an ITO/V_2O_5/ITO structure has been fabricated using thermal evaporation of V_2O_5 to replace the sol-gel process employed in our previous study. Resistive switching characteristics are observed for the as-fabricated devices before any post-annealing process. The device exhibits good thermal stability up to post annealing temperatures of 300˚C, and the reversible switching disappears when annealing temperature exceeds 350˚C. This is attributed to the re-crystallization of the amorphous V_2O_5 structure into its bulk orthorhombic structure. Ab initio calculations have been performed to evaluate the formation energies of bulk and amorphous V_2O_5, and it has been confirmed that it is easier to create oxygen vacancies in amorphous V_2O_5 than in the crystalline structure. The lifetime of the device has been greatly improved by the removal of the intercalated H_2O molecules. The results offer a promising IC compatible fabrication process for ITO/V_2O_5/ITO structures for memory applications.

Localized switching characteristics are found and discussed in ITO/V_2O_5/ITO structures, regardless of the synthesis process of V_2O_5 film. This is somewhat opposite to the observation that the current spreads across the top ITO layer. A preliminary physical model is briefly discussed to explain the contradiction and hopefully can provide more insights to the researchers who are interested in the underlying device physics.

Chapter 6. PHOTON-INDUCED COLORATION OF V_2O_5 THIN FILM IN ITO/V_2O_5/ITO STRUCTURE

Electrochromic materials have many applications in display and photonics area, including smart windows [91-93], modulators [94] and optical memories [95, 96]. Reversible color change has been discovered in materials such as GST [95, 97], due to phase change from amorphous to crystalline, whose optical properties can be transformed as desired. Electrochromics has also been discovered in Vanadium Pentoxide (V_2O_5) and has been applied to smart window applications. However, the electrochromic effect discovered in V_2O_5 is often accompanied by the introduction of Li ions [98-101]. As discussed in previous chapters, we have attribute the resistance change measured in experiments to the hypothesis that the oxidation states of V_2O_5 can be modified by applying voltage bias to a conductor/V_2O_5/conductor sandwich structure. It is well known that reduction of oxidation states of V_2O_5 often lead to a change in its color [31]. In this chapter, a distinct photon-induced coloration effect of V_2O_5 xerogel thin film is discussed and analyzed. This phenomenon is considered as an experimental proof of the switching mechanism, i.e. change in valence states of vanadium, proposed in previous chapters.

6.1 EXPERIMENTAL METHOD AND RESULTS

6.1.1 *Device Structure and Fabrication Process*

In order to observe the coloration of V_2O_5 underneath the electrode, ITO/V_2O_5 xerogel/ITO structure is fabricated and characterized. V_2O_5 thin film is synthesized by sol-gel process and no post annealing process is applied, implying that the water content is high in the film. Commercial ITO wafer with a sheet resistance of 15 Ω/sq is used as substrate and bottom electrode. Top ITO is deposited by magnetron sputtering and patterned by shadow masks with electrode diameter

ranging from 1 mm to 10 mm. Laser with different wavelengths is shone on the top electrode. The device structure is shown in Figure 6.1.

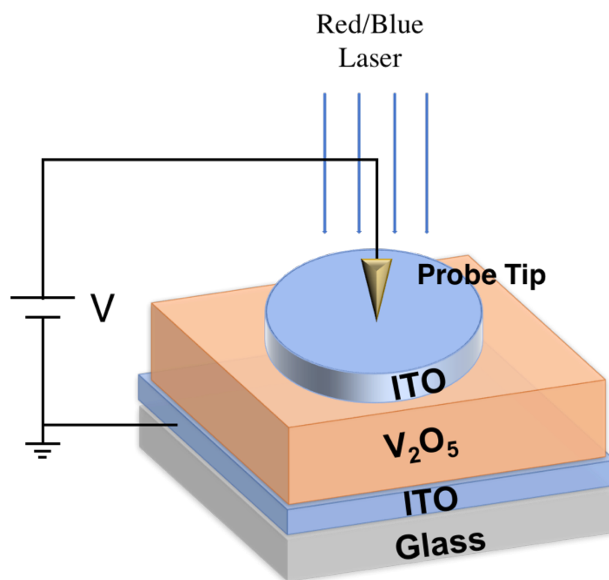

Figure 6.1. Structure of ITO/V_2O_5/ITO device and I-V measurement setup.

6.1.2 *I-V Characteristics in Dark and Illuminated Environment*

I-V characteristics of the devices are investigated first under microscope light and the results are shown in Figure 6.2. Unlike the devices with chromium electrodes, these devices show much less hysteresis loop in the 1st sweep. The resistance change is irreversible, similar to the Cr/V_2O_5/Cr devices. Under forward bias, the current reduces after switching. But under reverse bias, the current increases with increase in the reverse voltage. The asymmetric I-V characteristics could be explained also by the asymmetric fabrication process. The top V_2O_5 is exposed to ITO plasma and as a result can be substantially damaged, and a thin interfacial layer with a reduced oxidation state of V_2O_5 might be formed.

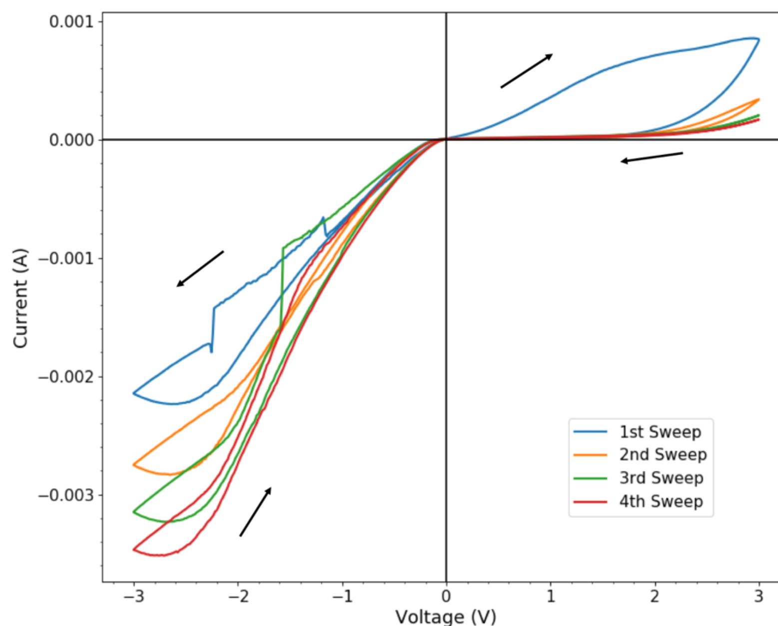

Figure 6.2. I-V characteristics of ITO/V_2O_5 xerogel/ITO device under microscope light.

Photoresponse of the devices is measured by applying a voltage and an external laser source simultaneously. The results are shown in Figure 6.3. Band gap of the V_2O_5 is reported to be 2.1 eV-2.3 eV, so blue laser with wavelength equal to 405 nm is shined on top of the device to allow absorption of photons by V_2O_5 film. A constant voltage bias is also applied to the top electrode while the bottom electrode is grounded. A large amount of photocurrent can be clearly observed, indicating that photon induced excitons are generated and separated. It has been confirmed that photons with larger wavelength (green laser, 520 nm; red laser 635 nm) cannot introduce photocurrent. We also observe that the magnitude of photocurrent is decreases with time and cannot be reversed.

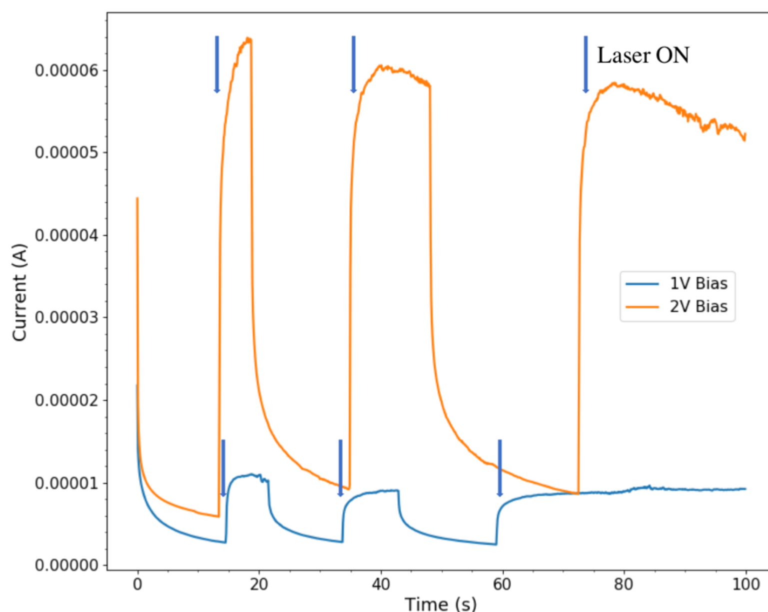

Figure 6.3. Transient photoresponse measurements under blue laser (wavelength = 405 nm)

6.1.3 *Coloration of V_2O_5 Film*

Coloration of the V_2O_5 film can be clearly observed after simultaneously shining blue laser and applying a voltage (or sufficient amount of current). Shadow of the probe tip can be clearly observed after switching OFF the laser source and retracting the probe tip (shown in Figure 6.4). The color of the V_2O_5 film changes from orangish to greenish after laser exposure with sufficient applied bias. We find that exposure of the V_2O_5 film to blue laser alone cannot introduce the color change. We also find that a color change is not observed when the voltage bias is less than +1.5 V, irrespective of if the blue laser is ON or OFF. However, a large voltage bias (typically > 5.0 V) can induce a similar color change to the V_2O_5 film without the laser source.

The coloration is somewhat reversible. The device will recover back to a yellowish color after being exposed in air for a few hours. Although the coloration only occurs under positive voltage bias, it cannot be erased with a negative bias.

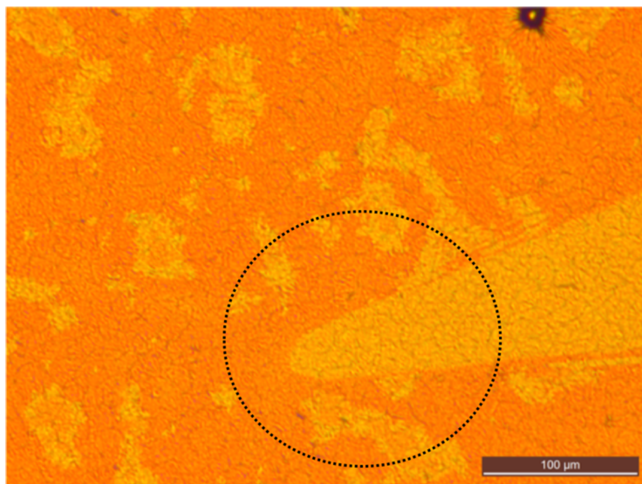

Figure 6.4. Optical microscope image of color change region. The shape of a probe tip can be clearly observed.

In order to characterize the coloration of the device, transmittance spectra are measured before and after coloration by using Varian Cary 5000 spectrophotometer. The result is shown in Figure 6.5. The absorption edge is located at wavelength of ~520 nm in the virgin devices. After the color change (induced by blue laser and voltage bias), the absorption edge shifts a bit to the blue color region (~490 nm). Another noticeable difference is the transmittance in the high wavelength region. Interestingly, the transmittance decreases by about 50% in the wavelength region of 600 nm – 800 nm, probably as a result of additional energy levels in the band structure induced by the electrochemical reactions.

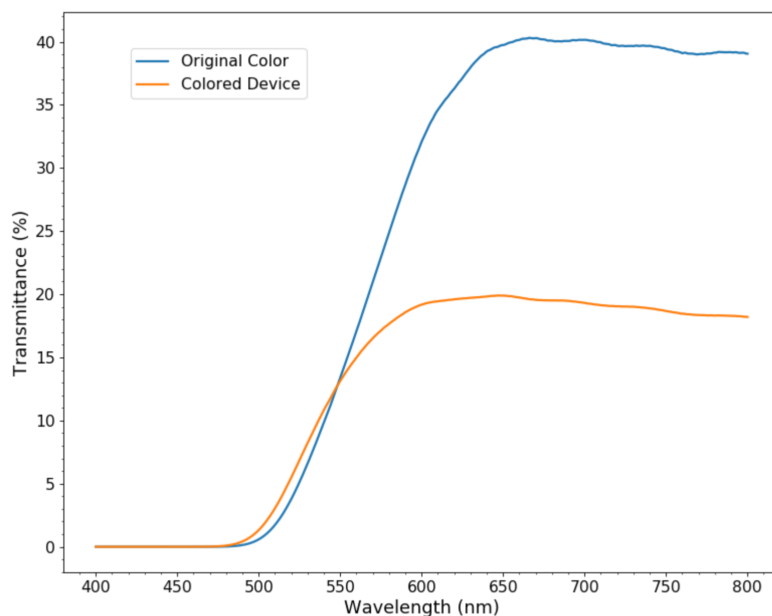

Figure 6.5. Transmittance spectrum of ITO/V_2O_5/ITO device before and after coloration.

6.2 PHYSICAL EXPLANATIONS

Besides the blue laser, we also tested laser sources with different wavelengths. Green (520nm) and red (635 nm) lasers did not introduce any color change on the device. This observation implies that the energy of photons has to be high enough to induce the color change. We have also tried increasing the applied voltage in a dark environment. Interestingly, without the presence of external photons, when the applied voltage is increased to 4~5 V, a similar color change from orangish to greenish can be observed in the same ITO/V_2O_5/ITO devices.

Based on the previous effects we have observed on Cr/V_2O_5 and ITO/V_2O_5 devices, it is intuitive to believe that the color change of V_2O_5 devices is mainly due to the change in oxidation states of vanadium ions. The applied voltage introduces electrochemical reactions at ITO/V_2O_5 interfaces and results in the reduction of oxidation states. The suggested process of electrochemical reactions is illustrated in Figure 6.6. Another proof is that the color of vanadium oxide in its

solution form changes from yellowish to bluish when the oxidation state is reduced. The most interesting aspect of our experiment is that the introduction of blue photons decreases the amount of applied voltage required to induce the color change effect.

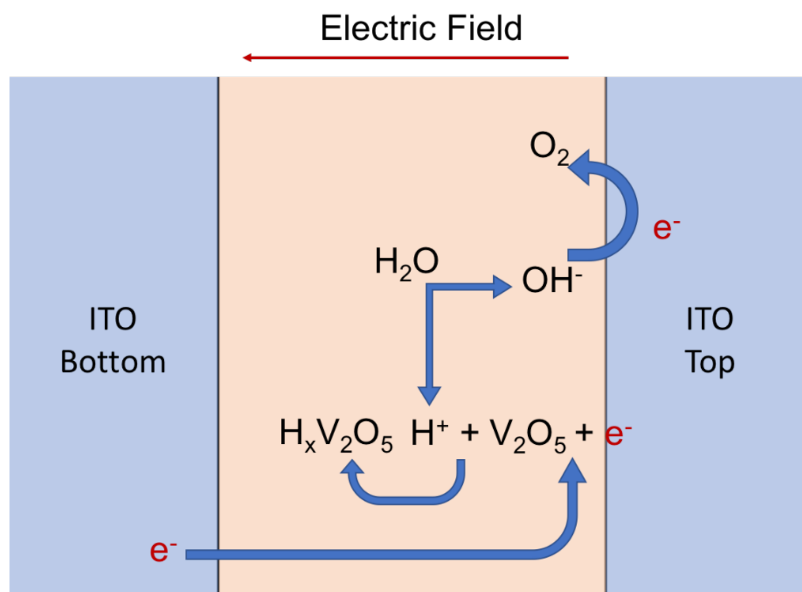

Figure 6.6. Illustration of electrochemical reactions occurring in ITO/V_2O_5/ITO structure

It is possible that the laser shined on the device heats it up, thus generating more current to accelerate the electrochemical reactions. We have placed the device on a hot plate and heated the device up to 300˚C. We shine blue light as the device is maintained at 300˚C. No coloration can be observed. It is worthy to try heating up the device and measuring I-V simultaneously to completely rule out the heating effect.

As the coloration only occurs when a laser with short wavelength is shined, it is straightforward to relate the energy of photons to the bandgap of V_2O_5. Our hypothesis is that the applied photons create extra electron-hole pairs at ITO/V_2O_5 interface; in the presence of an electric field, the electrons and holes are separated so that the local electron and hole densities are increased. We suggest that an increase in electron and hole concentrations at ITO/V_2O_5 interface introduced

by photons might accelerate equations (2.2) and (2.3), resulting in a stronger reaction under a smaller bias.

6.3 DISCUSSION AND RELATION TO PREVIOUS CHAPTERS

Compared with the forming-free resistive switching behavior discussed in Chapter 3, the device structure and fabrication process discussed in this chapter are the same except for removing the post-annealing step. The current level decreases by 5-8 times and reversible switching no longer exists. It has been discussed in Chapter 4 that the switching voltage increases with more intercalated H_2O molecules. In the device without post-annealing step, however, the coloration accompanied by the irreversible increase of resistance occurs before the reversible switching.

The significant difference in terms of device behavior suggests the importance of controlling the amount of intercalated H_2O molecules in V_2O_5 xerogel film. The reversible switching behavior and coloration effects arises from two different mechanisms. Reversible resistive switching is a localized effect: the resistance change only occurs underneath the probe tip; if the tip is moved to a different location, the detected resistance is still the same as the pristine resistance. The coloration effect occurs more globally. Figure 6.4 is the most straightforward proof: the whole region around the probe tip is colored by laser exposure and voltage bias. In fact, the colored region is determined by the size of laser spot coming out of the optical fiber. Moreover, the reason for the irreversibility of coloration is also likely due to permanent loss of oxygen atoms, similar to the mechanism discussed in Chapter 1. The key to switch between the two mechanisms is water content.

Large amount of intercalated water molecules affects the behavior of the device in two ways. It increases the overall resistance of the film, and thus increases the required voltage for reversible switching. It is also acting like a catalyst by participating in the electrochemical reactions at electrode/V_2O_5 interfaces, and introduces permanent loss of oxygen (in the form of oxygen gas).

The presence of intercalated water is also necessary as it decreases the formation energies of oxygen vacancies, which is also required in the reversible switching behavior.

Chapter 7. CONCLUSION

In this Ph.D. work, vanadium pentoxide (V_2O_5) thin film has been employed as an insulator/semiconductor material in metal-insulator-metal (MIM) structure for resistive memory applications. Sol-gel process was used first to synthesize V_2O_5 thin film and different conductors have been selected as electrode materials in order to obtain reversible resistive switching characteristics.

Irreversible resistive switching was discovered in Cr/V_2O_5/Cr structure and the switching mechanism is attributed to electrochemical reactions at both top and bottom Cr/V_2O_5 interfaces. Intercalated H_2O molecules are proved to be essential for the irreversible switching to occur. Resistance change is irreversible due to permanent loss of oxygen gas from V_2O_5. Efforts have been made to pursue a proper electrode material that can store oxygen ions reversibly and act as an oxygen reservoir.

Bipolar switching characteristics was first discovered in ITO/V_2O_5/ITO structure with a post annealing process applied to remove some of the intercalated H_2O molecules. It is proposed that when electric field is applied, oxygen ions from V_2O_5 layer can migrate through ITO/V_2O_5 interfaces, leaving a thin Schottky barrier at the interface as well as filling oxygen vacancies in ITO that contribute to its conductivity, thus resulting in the overall change in resistance.

Due to its layered structure and intercalated H_2O molecules, V_2O_5 xerogel thin film can experience huge transition during post annealing process. Atomic structure of V_2O_5 xerogel thin film was demonstrated to have significant impact on its resistive switching properties and an optimized annealing temperature is presented. Three different phases of V_2O_5 exist simultaneously in ITO/V_2O_5/ITO structure and the distribution is investigated and rationalized. First-principles simulation was then performed to provide more microscopic insights into the experimental results.

It is shown that the presence of intercalated H_2O molecules significantly reduce the formation energies of oxygen vacancies in V_2O_5 xerogel, compared to its bulk phases. Interestingly, negative formation energies were found for some of oxygen sites, indicating that reduction of valence states can occur spontaneously in V_2O_5 xerogel, which agrees with the degradation we found in our devices.

In order to overcome the drawbacks of V_2O_5 film synthesized by sol-gel process, thermal evaporation was employed for V_2O_5 thin film deposition. Better stability of I-V characteristics over annealing temperature was obtained due to the removal of water molecules from the system. DFT calculations of amorphous V_2O_5 structure generated by the melt-quench simulation process show that formation energies of oxygen vacancies is lower in the amorphous state.

The bipolar switching characteristics found in ITO/V_2O_5/ITO structures are demonstrated to be highly localized, whereas the current actually spreads over the whole top ITO layer. A preliminary physical model taking the Joule heating into account is proposed to explain the contradiction.

Finally, a unique photon-induced coloration is found in ITO/V_2O_5/ITO structures without the post annealing process. A color change from orangish to greenish when a voltage bias and laser exposure are applied simultaneously is observed. This observation is consistent with the hypothesis that reduction in oxidations states of V_2O_5 occurs during the electrochemical reactions. It also suggests that controlling the water content in V_2O_5 xerogel is critical in tuning the I-V characteristics of the device.

BIBLIOGRAPHY

[1] P. Pavan, R. Bez, P. Olivo, and E. Zanoni, "Flash memory cells-an overview," *Proceedings of the IEEE,* vol. 85, no. 8, pp. 1248-1271, 1997.

[2] R. Bez, E. Camerlenghi, A. Modelli, and A. Visconti, "Introduction to flash memory," *Proceedings of the IEEE,* vol. 91, no. 4, pp. 489-502, 2003.

[3] P. Cappelletti and A. Modelli, "Flash Memory Reliability," in *Flash Memories*, P. Cappelletti, C. Golla, P. Olivo, and E. Zanoni, Eds. Boston, MA: Springer US, 1999, pp. 399-441.

[4] C. Trinh *et al.*, "A 5.6MB/s 64Gb 4b/Cell NAND Flash memory in 43nm CMOS," in *2009 IEEE International Solid-State Circuits Conference - Digest of Technical Papers*, 2009, pp. 246-247,247a.

[5] S. Kang-Deog *et al.*, "A 3.3 V 32 Mb NAND flash memory with incremental step pulse programming scheme," *IEEE Journal of Solid-State Circuits,* vol. 30, no. 11, pp. 1149-1156, 1995.

[6] T. Tanaka *et al.*, "A quick intelligent page-programming architecture and a shielded bitline sensing method for 3 V-only NAND flash memory," *IEEE Journal of Solid-State Circuits,* vol. 29, no. 11, pp. 1366-1373, 1994.

[7] H. S. P. Wong *et al.*, "Phase Change Memory," *Proceedings of the IEEE,* vol. 98, no. 12, pp. 2201-2227, 2010.

[8] S. Lai, "Current status of the phase change memory and its future," in *IEEE International Electron Devices Meeting 2003*, 2003, pp. 10.1.1-10.1.4.

[9] M. K. Qureshi, V. Srinivasan, and J. A. Rivers, "Scalable high performance main memory system using phase-change memory technology," *SIGARCH Comput. Archit. News,* vol. 37, no. 3, pp. 24-33, 2009.

[10] B. C. Lee, E. Ipek, O. Mutlu, and D. Burger, "Architecting phase change memory as a scalable dram alternative," presented at the Proceedings of the 36th annual international symposium on Computer architecture, Austin, TX, USA, 2009.

[11] P. Zhou, B. Zhao, J. Yang, and Y. Zhang, "A durable and energy efficient main memory using phase change memory technology," *SIGARCH Comput. Archit. News,* vol. 37, no. 3, pp. 14-23, 2009.

[12] J. F. Scott and C. A. Paz de Araujo, "Ferroelectric Memories," *Science,* vol. 246, no. 4936, pp. 1400-1405, 1989.

[13] B. H. Park, B. S. Kang, S. D. Bu, T. W. Noh, J. Lee, and W. Jo, "Lanthanum-substituted bismuth titanate for use in non-volatile memories," *Nature,* vol. 401, p. 682, 10/14/online 1999.

[14] J. F. Scott, "Multiferroic memories," *Nature Materials,* vol. 6, p. 256, 03/11/online 2007.

[15] M. Bibes and A. Barthélémy, "Towards a magnetoelectric memory," *Nature Materials,* vol. 7, p. 425, 06/01/online 2008.

[16] S. Tehrani, J. M. Slaughter, E. Chen, M. Durlam, J. Shi, and M. DeHerren, "Progress and outlook for MRAM technology," *IEEE Transactions on Magnetics,* vol. 35, no. 5, pp. 2814-2819, 1999.

[17] B. N. Engel *et al.*, "A 4-Mb toggle MRAM based on a novel bit and switching method," *IEEE Transactions on Magnetics,* vol. 41, no. 1, pp. 132-136, 2005.

[18] T. Kishi *et al.*, "Lower-current and fast switching of a perpendicular TMR for high speed and high density spin-transfer-torque MRAM," in *2008 IEEE International Electron Devices Meeting*, 2008, pp. 1-4.

[19] D. Xiangyu, W. Xiaoxia, S. Guangyu, X. Yuan, H. Li, and C. Yiran, "Circuit and microarchitecture evaluation of 3D stacking magnetic RAM (MRAM) as a universal memory replacement," in *2008 45th ACM/IEEE Design Automation Conference*, 2008, pp. 554-559.

[20] N. Locatelli, V. Cros, and J. Grollier, "Spin-torque building blocks," *Nature Materials,* vol. 13, p. 11, 12/17/online 2013.

[21] J. J. Yang, M. D. Pickett, X. Li, D. A. Ohlberg, D. R. Stewart, and R. S. Williams, "Memristive switching mechanism for metal/oxide/metal nanodevices," *Nature nanotechnology,* vol. 3, no. 7, pp. 429-433, 2008.

[22] J. J. Yang, D. B. Strukov, and D. R. Stewart, "Memristive devices for computing," *Nature Nanotechnology,* Review Article vol. 8, p. 13, 12/27/online 2012.

[23] M. Prezioso, F. Merrikh-Bayat, B. D. Hoskins, G. C. Adam, K. K. Likharev, and D. B. Strukov, "Training and operation of an integrated neuromorphic network based on metal-oxide memristors," *Nature,* vol. 521, p. 61, 05/07/online 2015.

[24] S. Yu, B. Gao, Z. Fang, H. Yu, J. Kang, and H. S. P. Wong, "A Low Energy Oxide-Based Electronic Synaptic Device for Neuromorphic Visual Systems with Tolerance to Device Variation," *Advanced Materials,* vol. 25, no. 12, pp. 1774-1779, 2013.

[25] F. Pan, S. Gao, C. Chen, C. Song, and F. Zeng, "Recent progress in resistive random access memories: Materials, switching mechanisms, and performance," *Materials Science and Engineering: R: Reports,* vol. 83, pp. 1-59, 2014/09/01/ 2014.

[26] H.-S. P. Wong *et al.*, "Metal–oxide RRAM," *Proceedings of the IEEE,* vol. 100, no. 6, pp. 1951-1970, 2012.

[27] R. Waser, R. Dittmann, G. Staikov, and K. Szot, "Redox - based resistive switching memories - nanoionic mechanisms, prospects, and challenges," *Advanced materials,* vol. 21, no. 25 - 26, pp. 2632-2663, 2009.

[28] A. E. Semenov, I. N. Borodina, and S. H. Garofalini "In Situ Deposition and Ultrahigh Vacuum STM/AFM Study of V_2O_5/Li_3PO_4 Interface in a Rechargeable Lithium-Ion Battery," *Journal of The Electrochemical Society,* vol. 148, no. 11, pp. A1239-A1246, November 1, 2001 2001.

[29] Y. L. Cheah, V. Aravindan, and S. Madhavi, "Electrochemical Lithium Insertion Behavior of Combustion Synthesized V2O5 Cathodes for Lithium-Ion Batteries," *Journal of The Electrochemical Society,* vol. 159, no. 3, pp. A273-A280, January 1, 2012 2012.

[30] M. R. J. Scherer, L. Li, P. M. S. Cunha, O. A. Scherman, and U. Steiner, "Enhanced Electrochromism in Gyroid-Structured Vanadium Pentoxide," *Advanced Materials,* vol. 24, no. 9, pp. 1217-1221, 2012.

[31] S. Iwanaga, R. B. Darling, and D. H. Cobden, "Stable and erasable patterning of vanadium pentoxide thin films by atomic force microscope nanolithography," *Applied Physics Letters,* vol. 86, no. 13, 2005.

[32] R. Darling and S. Iwanaga, "Structure, properties, and MEMS and microelectronic applications of vanadium oxides," (in English), *Sadhana,* vol. 34, no. 4, pp. 531-542, 2009/08/01 2009.

[33] G. N. Greaves, "Small polaron conduction in V2O5 P2O5 glasses," *Journal of Non-Crystalline Solids,* vol. 11, no. 5, pp. 427-446, 1973/03/01/ 1973.

[34] J. G. Zhang and P. C. Eklund, "The switching mechanism in V2O5 gel films," *Journal of Applied Physics,* vol. 64, no. 2, pp. 729-733, 1988.

[35] M.-C. Wu and C.-S. Lee, "Field emission of vertically aligned V2O5 nanowires on an ITO surface prepared with gaseous transport," *Journal of Solid State Chemistry,* vol. 182, no. 8, pp. 2285-2289, 8// 2009.

[36] T. Zhai *et al.*, "Centimeter‐Long V2O5 Nanowires: From Synthesis to Field‐Emission, Electrochemical, Electrical Transport, and Photoconductive Properties," *Advanced Materials,* vol. 22, no. 23, pp. 2547-2552, 2010.

[37] G. T. Kim *et al.*, "Field-effect transistor made of individual V2O5 nanofibers," *Applied Physics Letters,* vol. 76, no. 14, pp. 1875-1877, 2000.

[38] N. Vieira, W. Avansi, A. Figueiredo, C. Ribeiro, V. Mastelaro, and F. Guimaraes, "Ion-sensing properties of 1D vanadium pentoxide nanostructures," *Nanoscale Research Letters,* vol. 7, no. 1, p. 310, 2012.

[39] I. Raible, M. Burghard, U. Schlecht, A. Yasuda, and T. Vossmeyer, "V2O5 nanofibres: novel gas sensors with extremely high sensitivity and selectivity to amines," *Sensors and Actuators B: Chemical,* vol. 106, no. 2, pp. 730-735, 2005.

[40] H. Y. Yu, B. H. Kang, U. H. Pi, C. W. Park, S.-Y. Choi, and G. T. Kim, "V2O5 nanowire-based nanoelectronic devices for helium detection," *Applied Physics Letters,* vol. 86, no. 25, pp. -, 2005.

[41] R.-S. Chen, W.-C. Wang, C.-H. Chan, H.-P. Hsu, L.-C. Tien, and Y.-J. Chen, "Photoconductivities in monocrystalline layered V2O5 nanowires grown by physical vapor deposition," *Nanoscale Research Letters,* vol. 8, no. 1, p. 443, 2013.

[42] V. Petkov, P. N. Trikalitis, E. S. Bozin, S. J. L. Billinge, T. Vogt, and M. G. Kanatzidis, "Structure of V2O5·nH2O Xerogel Solved by the Atomic Pair Distribution Function

Technique," *Journal of the American Chemical Society,* vol. 124, no. 34, pp. 10157-10162, 2002/08/01 2002.

[43] X. Yin *et al.*, "Adsorption of H2O on the V2O5 (010) surface studied by periodic density functional calculations," *The Journal of Physical Chemistry B,* vol. 103, no. 16, pp. 3218-3224, 1999.

[44] R. Schaub *et al.*, "Oxygen vacancies as active sites for water dissociation on rutile TiO2 (110)," *Physical Review Letters,* vol. 87, no. 26, p. 266104, 2001.

[45] H.-J. Zhai and L.-S. Wang, "Electronic structure and chemical bonding of divanadium-oxide clusters (V2Ox, x= 3-7) from anion photoelectron spectroscopy," *Journal of Chemical Physics,* vol. 117, no. 17, pp. 7882-7888, 2002.

[46] H. Lee *et al.*, "Low power and high speed bipolar switching with a thin reactive Ti buffer layer in robust HfO2 based RRAM," in *Electron Devices Meeting, 2008. IEDM 2008. IEEE International*, 2008, pp. 1-4: IEEE.

[47] Y. C. Yang, F. Pan, Q. Liu, M. Liu, and F. Zeng, "Fully room-temperature-fabricated nonvolatile resistive memory for ultrafast and high-density memory application," *Nano letters,* vol. 9, no. 4, pp. 1636-1643, 2009.

[48] B. Govoreanu *et al.*, "10× 10nm 2 Hf/HfO x crossbar resistive RAM with excellent performance, reliability and low-energy operation," in *Electron Devices Meeting (IEDM), 2011 IEEE International*, 2011, pp. 31.6. 1-31.6. 4: IEEE.

[49] R. Münstermann, J. J. Yang, J. P. Strachan, G. Medeiros ‐ Ribeiro, R. Dittmann, and R. Waser, "Morphological and electrical changes in TiO2 memristive devices induced by electroforming and switching," *physica status solidi (RRL)-Rapid Research Letters,* vol. 4, no. 1 ‐ 2, pp. 16-18, 2010.

[50] D. Lee *et al.*, "Excellent uniformity and reproducible resistance switching characteristics of doped binary metal oxides for non-volatile resistance memory applications," in *2006 International Electron Devices Meeting*, 2006, pp. 1-4: IEEE.

[51] D.-H. Kwon *et al.*, "Atomic structure of conducting nanofilaments in TiO2 resistive switching memory," *Nature nanotechnology,* vol. 5, no. 2, pp. 148-153, 2010.

[52] Z. Fang, H. Yu, X. Li, N. Singh, G. Lo, and D. Kwong, "Multilayer-based forming-free RRAM devices with excellent uniformity," *IEEE Electron Device Letters,* vol. 32, no. 4, pp. 566-568, 2011.

[53] M. Kawai, K. Ito, N. Ichikawa, and Y. Shimakawa, "Thermally formed conducting filaments in a single-crystalline NiO thin film," *Applied Physics Letters,* vol. 96, no. 7, p. 072106, 2010.

[54] Y.-S. Chen *et al.*, "An ultrathin forming-free resistance memory with excellent electrical performance," *IEEE electron device letters,* vol. 31, no. 12, pp. 1473-1475, 2010.

[55] B. Tulu, W. Chang, J. P. Chu, and S. Wang, "Forming-free resistive switching characteristics of 15 nm-thick multicomponent oxide," *Applied Physics Letters,* vol. 103, no. 25, p. 252904, 2013.

[56] X. Cao *et al.*, "Forming-free colossal resistive switching effect in rare-earth-oxide Gd2O3 films for memristor applications," *Journal of Applied Physics,* vol. 106, no. 7, p. 073723, 2009.

[57] O. Tuna, Y. Selamet, G. Aygun, and L. Ozyuzer, "High quality ITO thin films grown by dc and RF sputtering without oxygen," *Journal of Physics D: Applied Physics,* vol. 43, no. 5, p. 055402, 2010.

[58] I. Hamberg and C. G. Granqvist, "Evaporated Sn‐doped In2O3 films: Basic optical properties and applications to energy‐efficient windows," *Journal of Applied Physics,* vol. 60, no. 11, pp. R123-R160, 1986.

[59] Y. Gassenbauer *et al.*, "Surface states, surface potentials, and segregation at surfaces of tin-doped In 2 O 3," *Physical Review B,* vol. 73, no. 24, p. 245312, 2006.

[60] Z. Wan, R. B. Darling, and M. Anantram, "Programmable diode/resistor-like behavior of nanostructured vanadium pentoxide xerogel thin film," *Physical Chemistry Chemical Physics,* vol. 17, no. 45, pp. 30248-30254, 2015.

[61] O. Mryasov and A. Freeman, "Electronic band structure of indium tin oxide and criteria for transparent conducting behavior," *Physical Review B,* vol. 64, no. 23, p. 233111, 2001.

[62] P.-K. Yang *et al.*, "A Fully Transparent Resistive Memory for Harsh Environments," *Scientific reports,* vol. 5, 2015.

[63] J. Meyer, K. Zilberberg, T. Riedl, and A. Kahn, "Electronic structure of Vanadium pentoxide: An efficient hole injector for organic electronic materials," *Journal of Applied Physics,* vol. 110, no. 3, p. 033710, 2011.

[64] A. Walsh *et al.*, "Nature of the band gap of In 2 O 3 revealed by first-principles calculations and x-ray spectroscopy," *Physical review letters,* vol. 100, no. 16, p. 167402, 2008.

[65] W.-Y. Chang, Y.-C. Lai, T.-B. Wu, S.-F. Wang, F. Chen, and M.-J. Tsai, "Unipolar resistive switching characteristics of ZnO thin films for nonvolatile memory applications," *Applied Physics Letters,* vol. 92, no. 2, p. 2110, 2008.

[66] C. Y. Lin *et al.*, "Effect of Top Electrode Material on Resistive Switching Properties of <formula formulatype="inline"><tex>$hbox{ZrO}_{2}$</tex></formula> Film Memory Devices," *IEEE Electron Device Letters,* vol. 28, no. 5, pp. 366-368, 2007.

[67] P. Calka *et al.*, "Engineering of the Chemical Reactivity of the Ti/HfO2 Interface for RRAM: Experiment and Theory," *ACS applied materials & interfaces,* vol. 6, no. 7, pp. 5056-5060, 2014.

[68] S. H. Ng *et al.*, "Synthesis and electrochemical properties of V2O5 nanostructures prepared via a precipitation process for lithium-ion battery cathodes," *Journal of Power Sources,* vol. 174, no. 2, pp. 1032-1035, 12/6/ 2007.

[69] A. M. Cao, J. S. Hu, H. P. Liang, and L. J. Wan, "Self‐assembled vanadium pentoxide (V2O5) hollow microspheres from nanorods and their application in lithium‐Ion batteries," *Angewandte Chemie International Edition,* vol. 44, no. 28, pp. 4391-4395, 2005.

[70] J. Liu, H. Xia, D. Xue, and L. Lu, "Double-shelled nanocapsules of V2O5-based composites as high-performance anode and cathode materials for Li ion batteries," *Journal of the American Chemical Society,* vol. 131, no. 34, pp. 12086-12087, 2009.

[71] R. Enjalbert and J. Galy, "A refinement of the structure of V2O5," *Acta Crystallographica Section C: Crystal Structure Communications,* vol. 42, no. 11, pp. 1467-1469, 1986.

[72] Z. Wan, R. B. Darling, A. Majumdar, and M. P. Anantram, "A forming-free bipolar resistive switching behavior based on ITO/V2O5/ITO structure," *Applied Physics Letters,* vol. 111, no. 4, p. 041601, 2017.

[73] V. Filonenko, M. Sundberg, P.-E. Werner, and I. Zibrov, "Structure of a high-pressure phase of vanadium pentoxide, β-V2O5," *Acta Crystallographica Section B: Structural Science,* vol. 60, no. 4, pp. 375-381, 2004.

[74] Q. Su, W. Lan, Y. Wang, and X. Liu, "Structural characterization of β-V 2 O 5 films prepared by DC reactive magnetron sputtering," *Applied Surface Science,* vol. 255, no. 7, pp. 4177-4179, 2009.

[75] F. Roumili, S. Benbahouche, and J.-C. Sangleboeuf, "Mechanical strength of soda-lime glass sandblasted by gravitation," *Friction,* vol. 3, no. 1, pp. 65-71, 2015.

[76] T. P. Seward and T. Vascott, "High temperature glass melt property database for process modeling," (in English), 2005.

[77] B. Singh *et al.*, "Anomalous lattice behavior of vanadium pentaoxide (V2O5): X-ray diffraction, inelastic neutron scattering and ab initio lattice dynamics," *Physical Chemistry Chemical Physics,* 10.1039/C7CP01904A vol. 19, no. 27, pp. 17967-17984, 2017.

[78] W.-F. Wu and B.-S. Chiou, "Mechanical properties of r.f. magnetron sputtered indium tin oxide films," *Thin Solid Films,* vol. 293, no. 1, pp. 244-250, 1997/01/30/ 1997.

[79] G. Kresse and J. Hafner, "Ab initio molecular-dynamics simulation of the liquid-metal–amorphous-semiconductor transition in germanium," *Physical Review B,* vol. 49, no. 20, pp. 14251-14269, 05/15/ 1994.

[80] G. Kresse and J. Furthmüller, "Efficient iterative schemes for ab initio total-energy calculations using a plane-wave basis set," *Physical Review B,* vol. 54, no. 16, pp. 11169-11186, 10/15/ 1996.

[81] P. E. Blöchl, "Projector augmented-wave method," *Physical Review B,* vol. 50, no. 24, pp. 17953-17979, 12/15/ 1994.

[82] J. P. Perdew, K. Burke, and M. Ernzerhof, "Generalized Gradient Approximation Made Simple," *Physical Review Letters,* vol. 77, no. 18, pp. 3865-3868, 10/28/ 1996.

[83] J. P. Perdew *et al.*, "Atoms, molecules, solids, and surfaces: Applications of the generalized gradient approximation for exchange and correlation," *Physical Review B,* vol. 46, no. 11, pp. 6671-6687, 09/15/ 1992.

[84] A. I. Liechtenstein, V. I. Anisimov, and J. Zaanen, "Density-functional theory and strong interactions: Orbital ordering in Mott-Hubbard insulators," *Physical Review B,* vol. 52, no. 8, pp. R5467-R5470, 08/15/ 1995.

[85] L. Wang, T. Maxisch, and G. Ceder, "Oxidation energies of transition metal oxides within the GGA+U framework," *Physical Review B,* vol. 73, no. 19, p. 195107, 05/04/ 2006.

[86] W. H. Press, *Numerical recipes : the art of scientific computing*. New York: Cambridge University Press, 1986.

[87] V. V. Porsev, A. V. Bandura, and R. A. Evarestov, "Water adsorption on α-V2O5 surface and absorption in V2O5·nH2O xerogel: DFT study of electronic structure," *Surface Science,* vol. 666, no. Supplement C, pp. 76-83, 2017/12/01/ 2017.

[88] D. O. Scanlon, A. Walsh, B. J. Morgan, and G. W. Watson, "An ab initio Study of Reduction of V2O5 through the Formation of Oxygen Vacancies and Li Intercalation," *The Journal of Physical Chemistry C,* vol. 112, no. 26, pp. 9903-9911, 2008/07/01 2008.

[89] R. Santos *et al.*, "Thermoelectric properties of V2O5 thin films deposited by thermal evaporation," *Applied Surface Science,* vol. 282, pp. 590-594, 2013/10/01/ 2013.

[90] Y. Hu, X. Diao, C. Wang, W. Hao, and T. Wang, "Effects of heat treatment on properties of ITO films prepared by rf magnetron sputtering," *Vacuum,* vol. 75, no. 2, pp. 183-188, 2004/07/12/ 2004.

[91] D. R. Rosseinsky and R. J. Mortimer, "Electrochromic Systems and the Prospects for Devices," *Advanced Materials,* vol. 13, no. 11, pp. 783-793, 2001.

[92] N. M. Rowley and R. J. Mortimer, "New electrochromic materials," *Science Progress,* vol. 85, no. 3, pp. 243-262, // 2002.

[93] G. A. Niklasson and C. G. Granqvist, "Electrochromics for smart windows: thin films of tungsten oxide and nickel oxide, and devices based on these," *Journal of Materials Chemistry,* 10.1039/B612174H vol. 17, no. 2, pp. 127-156, 2007.

[94] P. Hosseini, C. D. Wright, and H. Bhaskaran, "An optoelectronic framework enabled by low-dimensional phase-change films," *Nature,* vol. 511, p. 206, 07/09/online 2014.

[95] C. Ríos *et al.*, "Integrated all-photonic non-volatile multi-level memory," *Nature Photonics,* vol. 9, p. 725, 09/21/online 2015.

[96] M. Wuttig, H. Bhaskaran, and T. Taubner, "Phase-change materials for non-volatile photonic applications," *Nature Photonics,* Review Article vol. 11, p. 465, 08/01/online 2017.

[97] T. Tuma, A. Pantazi, M. Le Gallo, A. Sebastian, and E. Eleftheriou, "Stochastic phase-change neurons," *Nature Nanotechnology,* Article vol. 11, p. 693, 05/16/online 2016.

[98] K. Takahashi, Y. Wang, and G. Cao, "Growth and electrochromic properties of single-crystal V2O5 nanorod arrays," *Applied Physics Letters,* vol. 86, no. 5, p. 053102, 2005.

[99] H. K. Koduru, H. M. Obili, and G. Cecilia, "Spectroscopic and electrochromic properties of activated reactive evaporated nano-crystalline V2O5 thin films grown on flexible substrates," *International Nano Letters,* journal article vol. 3, no. 1, p. 24, April 17 2013.

[100] L. Ottaviano, A. Pennisi, F. Simone, and A. M. Salvi, "RF sputtered electrochromic V2O5 films," *Optical Materials,* vol. 27, no. 2, pp. 307-313, 2004/11/01/ 2004.

[101] Y. Takako, B. Nobuyoshi, and K. Yasuo, "Electrochromic Properties of V 2 O 5 Thin Films Colloid-Chemically Deposited onto ITO Glasses," *Japanese Journal of Applied Physics,* vol. 26, no. 5R, p. 782, 1987.

APPENDIX A

INSTRUMENTATION: TEST CHAMBER

An environmental test chamber was built to measure the dependence of I-V characteristics of $Cr/V_2O_5/Cr$ devices on the testing environment described in Chapter 2.4. The test chamber was designed to have the following functionalities: (1) environment control (vacuum, O_2, N_2, N_2/H_2, H_2O, Dry Air etc.). (2) electrical feedthrough (used coaxial cable for better noise shielding). (3) temperature control. The chamber design is performed by Prof. R. Bruce Darling. The chamber assembling is completed by Prof. R. Bruce Darling and Zhenni Wan.

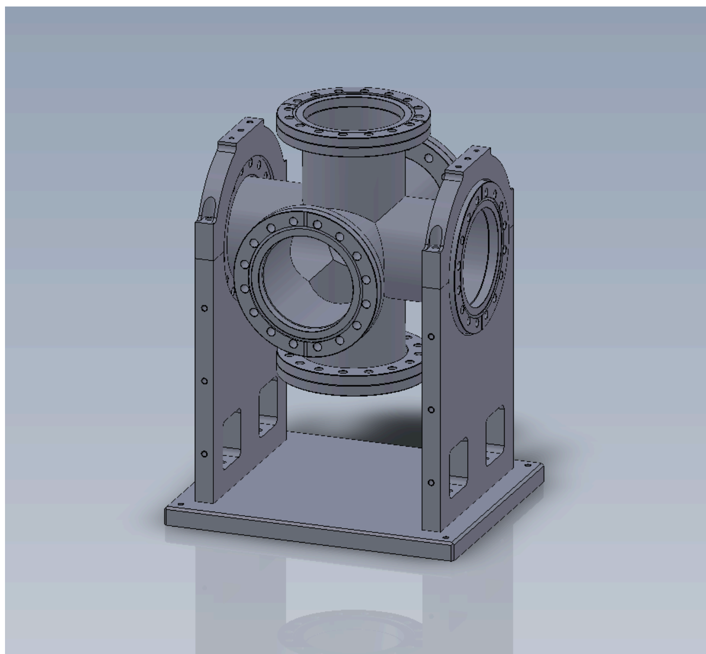

Figure A.1. Design of test chamber and base

Figure A.1 shows the design of test chamber and base. The test chamber itself is a six-way cross with six ports for assembling feedthroughs. Left port is reserved for gas and cooling water feedthroughs and the corresponding design is shown in Figure A.2. The two cooling lines in the center of the flange are LN2 feedthroughs that can be used to pass either liquid nitrogen or cooling water. The rest four feedthroughs are for other gases and air vent. Right port is used for electrical feedthrough. An adapter flange with four BNC feedthroughs is assembled for performing electrical measurements at low current level. Front port is reserved for a transparent view port in order to visualize the sample inside the chamber. Back port is connected with a mechanical pump to provide vacuum to the chamber. Since the overall chamber volume is low, it is easier to obtain a reasonable

low vacuum (10 mTorr) with a mechanical pump within one hour of pumping. The chamber itself is designed to hold much higher vacuum level. However, due to the leakage introduced during manual assembling, the vacuum level can only be in 10 mTorr range. Future engineering will be required to fully utilize its vacuum capability by digging out the source of leakage.

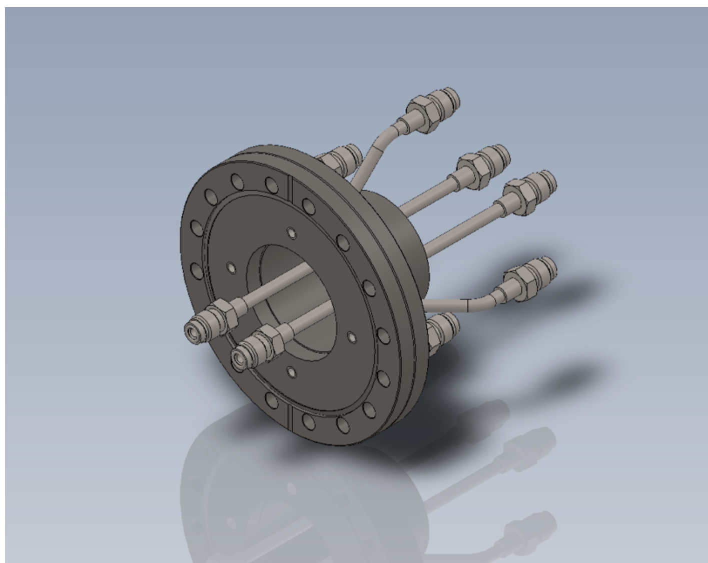

Figure A.2. Design of gas feedthrough port

Top port of the six-way cross chamber is used as a loading door for the sample holder. Since no micromanipulators are assembled in the chamber, one needs to make contact to the sample using pogo pins outside of chamber and then load the sample holder into the chamber manually. Bottom port is used for the sample stage shown in Figure A.3. The top red copper block is used for cooling/heating the sample. The bottom red copper has two channels for passing through the cooling lines to maintain its temperature. Between the top and bottom copper block, there is a sandwiched thermoelectric cooler (TEC) element that provides a temperature difference up to ± 60˚C. The TEC is powered via a DB25 feedthrough on the bottom flange.

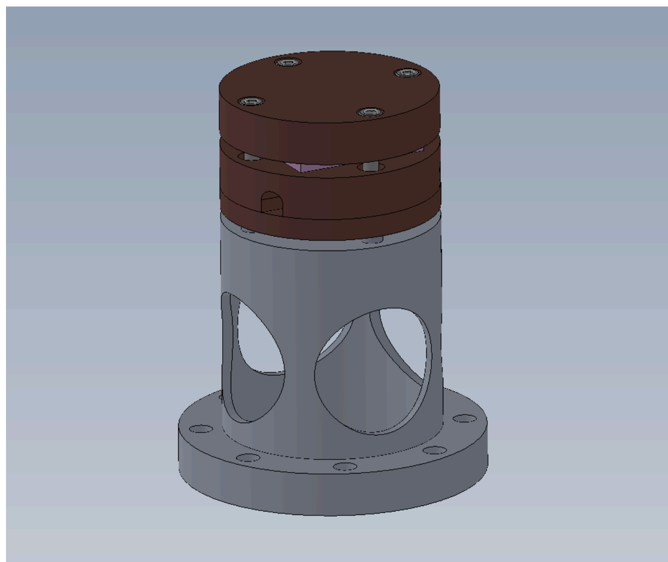

Figure A.3. Design of sample stage

The whole environmental test system contains the test chamber, a gas panel which mixes different gases with controlled ratios, gas cylinders, a mechanical pump, a thermometer that measures the temperature of sample stage via the thermocouple through the bottom flange, a source meter unit (SMU) for the current-voltage measurements using co-axial cables to minimize the electromagnetic noises.

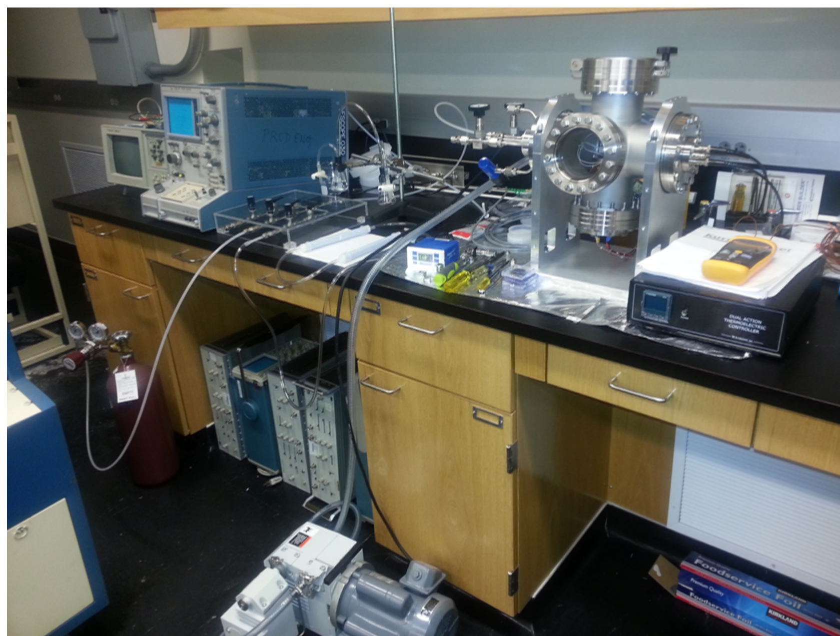

Figure A.4. Picture of test chamber, gas panel, pump and gas cylinders

The environmental test chamber described above uses pogo pins as probers to contact with the sample. In order to measure the I-V characteristics at low current level at various temperatures as well as maintain a delicate control of the tip position, a temperature-controlled probe station is built in ambient environment.

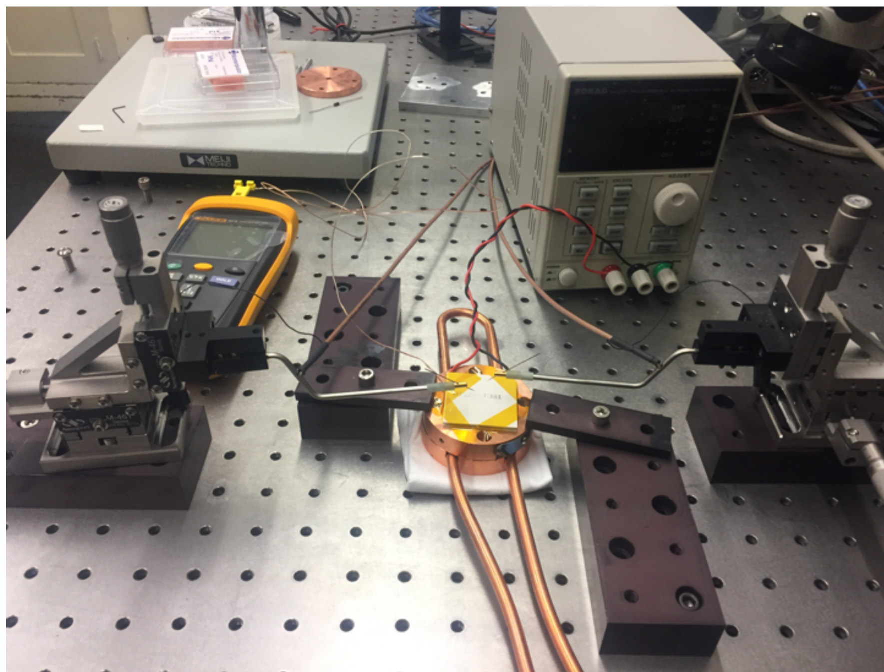

Figure A.5. Picture of temperature-controlled probe station

Figure A.5 shows the picture of the custom-built temperature-controlled probe station. Two probes are set up for two-wire measurements, but the system can be extended to four-wire measurements by adding two additional probes. Triaxial probe holders are used for the best noise shielding and ultra-low current measurements. A TEC element is used to control the temperature of the DUT and it is powered by a DC power source. The copper block with two cooling lines passing through is installed for heat dissipation.

The cooling water is set to have a fixed temperature of 20˚C. The TEC element has the capability of raising/decreasing the temperature for a maxim range of 60˚C. However, since the system is ensemble in ambient environment, water can condense on the surface of TEC element when temperature drops close to 0˚C, preventing further decrease of the temperature as well as interrupting the measurements by creating moisture on probe tips and samples. Therefore, the operation temperature of the probe station is 3˚C – 85˚C.

It is also worthy to point out that as the TEC element is powered by a DC voltage source instead of a PWM temperature controller, the resulted temperature is fully determined by the direction and amplitude of the supplied current. There is no function to create a set point and use the feedback loop to stabilize the temperature. The reason behind it is that due to the high AC current level running through the TEC element (10 A range) when a PWM temperature controller is being used, huge electromagnetic noises are emitted from the power lines and create significant distortion to the measurements. This problem can be eliminated by using a DC source instead.

VITA

Zhenni Wan received his B.Sc degree from Institute of Microelectronics at Peking University, Bejing, China, in June 2012. She is currently a Ph.D. candidate in Department of Electrical Engineering at University of Washington, Seattle.

Her research interests include experiments and modeling of semiconductor devices in nanoscale, application of novel materials on memory devices and sensors, and exploring the underlying device physics.